Mikada, H., Becker, K., Moore, J.C., Klaus, A., et al., 2002
Proceedings of the Ocean Drilling Program, Initial Reports Volume 196

4. Site 808[1]

Shipboard Scientific Party[2]

SITE SUMMARY

We drilled Hole 808I to obtain logging-while-drilling (LWD) data through the frontal thrust and décollement zones at the deformation front of the Nankai Trough and to install an Advanced CORK (ACORK) long-term subseafloor hydrogeologic monitoring experiment (Fig. **F1**). This hole complements Site 808 cores, which were recovered during Ocean Drilling Program (ODP) Leg 131. Coring, logging, and monitoring here are intended to document the physical and chemical state of the Nankai accretionary prism and underthrust sediments through the frontal thrust zone, the décollement zone, and into oceanic basement.

Log Quality

The overall quality of the LWD logs recorded in Hole 808I is variable. We recorded at least one sample per 15 cm over 99% of the total section. Sections of enlarged borehole indicated by differential caliper measurements yield unreliable density and associated porosity data, which is confirmed by a comparison to core data. Unreliable data are primarily associated with the depth intervals at 725–776 and 967–1057 meters below seafloor (mbsf), where there was a long gap between drilling and recording of the logs due to wiper trips or poor hole conditions (see **"Operations,"** p. 5). Density and density-derived porosity should be used cautiously until more complete corrections and editing is completed postcruise. Although the Anadrill Integrated Drilling Evaluation and Logging (IDEAL) sonic-while-drilling (ISONIC) velocity tool worked well, the processing of the waveforms was not straightforward and postcruise processing is required to yield reliable sonic data.

F1. Site 808 summary diagram, p. 32.

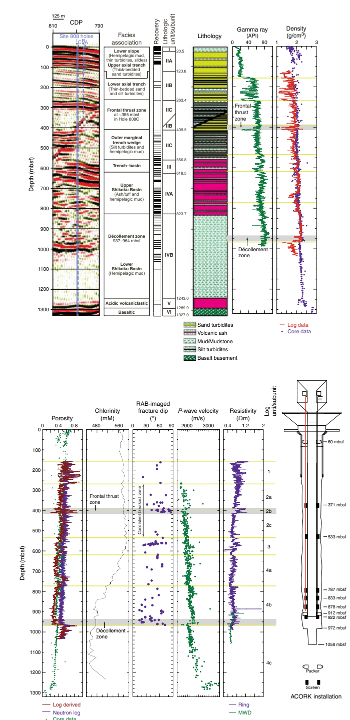

[1]**Examples of how to reference the whole or part of this volume.**
[2]**Shipboard Scientific Party addresses.**

Ms 196IR-104

Log Units and Lithology

Four log units and six log subunits were defined through a combination of visual interpretation and multivariate statistical analysis. Log Unit 1 (156–268 mbsf) is characterized by the overall lowest mean values of gamma ray, density, and photoelectric effect and overall highest mean values of resistivity and neutron porosity. These values coincide with very fine grained sandstones, siltstones, and clayey siltstone/silty claystones observed in the cores. Log Unit 2 (268–530 mbsf) has constant values of gamma ray and neutron porosity and a decreasing resistivity log. A high variability in the differential caliper log and a large number of values >1 in reflect bad borehole conditions. Log Unit 3 (530–620 mbsf) is marked by a significant increase in mean values of gamma ray, density, and photoelectric effect. Log Unit 4 (620–1035 mbsf) is characterized by the overall highest mean values of gamma ray, photoelectric effect, and density and the lowest mean values of resistivity and neutron porosity. Generally, a positive correlation between gamma ray and photoelectric effect is observed. A continuous increase in gamma ray and photoelectric effect is observed from log Unit 1 to Unit 4, which reflects an increase of clay and carbonate content. Log Units 3 and 4 are characterized by a positive correlation between resistivity and density.

Structural Geology

Resistivity-at-the-bit (RAB) tools imaged fracture populations and borehole breakouts throughout much of the borehole. We identified both resistive and conductive fractures, respectively interpreted as compactively deformed fractures (leading to porosity collapse) and open fractures. Fractures are concentrated in discrete deformation zones that correlate with those seen in Site 808 cores during Leg 131: the frontal thrust zone (389–414 mbsf), a fractured interval (559–574 mbsf), and the décollement zone (~940–960 mbsf). Only relatively sparse deformation occurs between these zones. The major deformation zones are dominated by conductive fractures and overall high resistivity with resistive fractures between the zones. Fractures are steeply dipping (majority >30°) and strike predominantly east-northeast–west-southwest, close to perpendicular to the convergence vector (~310°–315°; Seno et al., 1993). Bedding dips are predominantly low angle (<50°) but are difficult to identify in the highly deformed zones, biasing this result. Bedding strike is more random than fracture orientation, but where a preferred orientation is recorded, beds strike subparallel to fractures and approximately perpendicular to the convergence vector.

The frontal thrust zone (389–414 mbsf) represents the most highly deformed zone at Hole 808I and contains predominantly south-dipping (antithetic to the seismically imaged main thrust fault) and a few north-dipping east-northeast–west-southwest striking fractures. The highly fractured interval at 559–574 mbsf contains similar fracture patterns to the frontal thrust zone. Both deformation zones are characterized by high-conductivity (open?) fractures within a zone of overall high resistivity.

Deformation at the décollement zone is more subdued and is represented by a series of discrete fracture zones. The décollement zone imaged in the RAB images (937–965 mbsf) is defined by a general increase in fracture density and a marked variability in physical properties.

Borehole breakouts are recorded throughout Hole 808I. They are particularly strongly developed within log Unit 2 (270–530 mbsf), suggesting lithologic control on sediment strength and breakout formation. Breakouts indicate a northeast-southwest orientation for the minimum horizontal compressive stress (σ_2), consistent with a northwest-southeast convergence vector (310°–315°, parallel to σ_1; Seno et al., 1993), Breakout orientation deviates slightly from the dominant strike of fractures (east-northeast–west-southwest), but this deviation may be within the measurement error.

Physical Properties

The Hole 808I LWD density log shows a good fit to the core bulk density, slightly underestimating core values in the upper 550 m and slightly overestimating core values between 550 and 970 mbsf. Below 156 mbsf the LWD density log shows a steady increase from ~1.7 to ~1.95 g/cm^3 at 389 mbsf. Between 389 and 415 mbsf density shows large variations corresponding to the frontal thrust zone. The low density values here are probably spurious, produced by washout of the borehole. Below the frontal thrust zone density decreases sharply to ~1.85 g/cm^3, and below 530 mbsf it increases to ~2.1 g/cm^3. Between 725 and 776 mbsf density drops sharply to ~1.75 g/cm^3, corresponding to a period of borehole wiper trips. Density increases more rapidly from ~1.95 g/cm^3 at 776 mbsf to 2.25 g/cm^3 at 930 mbsf, decreasing steadily to ~2.15 g/cm^3 before stepping down to 1.4 g/cm^3 at 965 mbsf. This corresponds to the base of the décollement zone; below, density increases steadily from ~1.7 g/cm^3 at 975 mbsf to ~2.0 g/cm^3 at 1034.79 mbsf.

The downhole variations of LWD resistivity measurements show identical trends in all five resistivity logs of Hole 808I. All log unit boundaries are clearly identified. Log Unit 1 has an average resistivity of ~0.8–0.9 Ωm. After a sharp decrease in resistivity from 1.3 to 0.5 Ωm between 156 and 168 mbsf, the signal shows an increasing trend downward to the Unit 1/2 boundary. Unit 2 is characterized by an overall decreasing trend in resistivity from ~0.9 to ~0.6 Ωm. However, this trend is sharply offset at 389–415 mbsf (log Subunit 2b), where resistivity values are ~0.3 Ωm higher. This zone seems to correspond to the frontal thrust; the higher resistivity here may reflect compactive deformation in the frontal thrust zone. Unit 3 is characterized by a higher degree of variability in the resistivity signal. Resistivity again exhibits less variation in Unit 4 where it averages ~0.6 Ωm. At ~925 mbsf resistivity values change from gradually increasing to gradually decreasing. This change in trend occurs near the top of the décollement zone and may represent a tendency toward increasing porosity downward within the décollement zone. As was observed in Hole 1173B, shallow-focused resistivity values are systematically higher than both medium- and deep-focused resistivity values.

Logs and Seismic Reflection Data

Correlations between the synthetic seismogram and seismic reflection data are only broadly consistent beneath the cased section (~150 mbsf). The defined lithologic boundaries or units correlate only at a few depth intervals. The details of amplitude and waveform throughout most of the section do not match the seismic data. Amplitudes of the intervals between ~200 and ~400 mbsf, between ~750 and ~850 mbsf, and below ~925 mbsf are significantly higher in the synthetic seismogram than in the seismic data. The velocity and density logs infer reflections that are not observed in the seismic data, so many of the velocity and density values may not reflect true in situ properties and may be a product of poor hole conditions.

ACORK Installation

At Hole 808I we assembled a 964-m-long ACORK casing string, incorporating two packers and six screens, for long-term observations of pressures in three principal zones, as follows:

1. The décollement zone and overlying section of the lower Shikoku Basin deposits (lithologic Unit IV). A screen was placed immediately above the casing shoe, with a packer immediately above the screen. The hole was opened with the intent of emplacing the screen just into the décollement zone, with the packer positioned in a competent section immediately above the décollement zone. Three other screens were configured above the packer, to span the upper section of the lower Shikoku Basin deposits to study the variation of physical properties and propagation of any pressure signals away from the décollement zone.
2. A fractured interval at 560–574 mbsf in the upper Shikoku Basin deposits, as identified in RAB logs (see **"560-mbsf Fractured Interval,"** p. 21, in "Logs and Structural Geology"). A single screen was intended to be deployed in this zone.
3. The frontal thrust zone, centered at ~400 mbsf. A single screen was intended to be deployed in this zone.

Drilling conditions during installation of the ACORK steadily worsened starting ~200 m above the intended total depth. Despite all efforts, progress stopped 37 m short of the intended installation depth. This left the screen sections offset above the intended zones (Fig. **F1**), not an ideal installation but still viable in terms of scientific objectives. In addition, this left the ACORK head 42 m above seafloor, unable to support its own weight once we pulled the drilling pipe out. Fortunately, when the ACORK head fell over it landed on the seafloor such that all critical components remained in good condition. This includes the critical hydraulic umbilical, data logger, and the underwater-mateable connector, which remains easily accessible by a remotely operated vehicle (ROV) or by submersible for data download.

BACKGROUND AND OBJECTIVES

Site 808 penetrates the seaward edge of the imbricate thrust zone of the Nankai accretionary prism (Figs. **F2, F3, F4**). Previous drilling here during Leg 131 cored through the frontal thrust zone, the décollement zone, and ended in the top of the oceanic crust at a total depth (TD) of 1327 m (Shipboard Scientific Party, 1991). This site is the most complete documentation of the initial thrusting of a terrigenous clastic section in a subduction zone (Hill, Taira, Firth, et al., 1993). The décollement zone here is marked by a well-defined negative-polarity seismic reflection (Moore et al., 2001). The deeper part of the hole shows a large negative anomaly in pore water chloride content, spanning several hundred meters of formation surrounding the décollement zone. Ran-

F2. Locations of Leg 196 drill sites, p. 34.

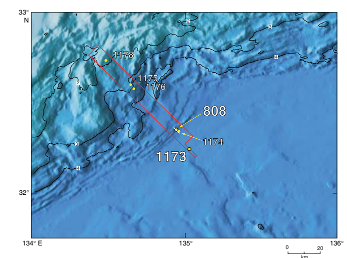

F3. Seismic profile crossing Site 808, p. 35.

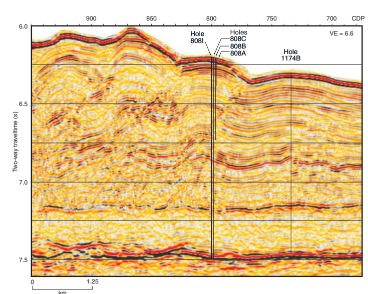

F4. Locations of Leg 196 and 131 drill holes at Site 808, p. 36.

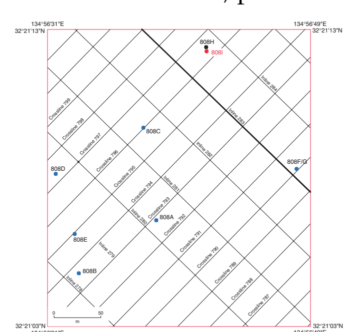

som et al. (1995) interpreted this anomaly as a response to fluid flow from seismogenic depths, but in fact it may represent a combination of deeply sourced fluids and those derived from local diagenetic alteration (Moore et al., 2001). The "Leg 196 Summary" chapter and Moore et al. (2001) provide additional topical and regional background on this site.

Overall, the goal of Leg 196 at Site 808 was to determine the initial state of deformation and fluid flow in a subduction zone dominated by terrigenous sediment. Given that the site crosses both the frontal thrust and décollement zones and also penetrates into basement, it provides a near-ideal location for the combination of techniques used during Leg 196: (1) LWD to document variations of physical properties across structural features and within the sections away from such features, and (2) long-term monitoring of the hydrogeologic state and processes in these zones with an ACORK, extending the understanding derived from similar experiments at other convergent margins (e.g., Becker et al., 1997). We intend to combine the LWD results and results from long-term subseafloor monitoring with existing core data to determine the spatial distribution and temporal progression in deformation, and the hydrologic evolution of the frontal thrust and décollement zones.

Because no significant wireline log data were collected at Site 808 during Leg 131, penetration data acquisition by LWD was a prime Leg 196 objective to provide continuous profiles of in situ physical properties. The ACORK at Site 808 was originally planned with a screen and packer at top of basement and an array of packers and screens spanning the décollement zone, to emphasize long-term monitoring of the hydrogeologic environment in the basement and across the décollement zone. Ultimately, the combination of ACORK measurements and the information from the LWD data should allow estimation of pore pressures and permeabilities as well as direct sampling of fluid from the décollement zone.

OPERATIONS

An operations summary of Leg 196 Site 808 is presented in Table T1. Previous coring operations at Site 808 conducted during Leg 131 are reported in Taira, Hill, Firth, et al. (1991).

T1. Site 808 operations, p. 66.

Site 808

Hole 808H

After the 1-hr, 8-nmi transit from Site 1173, we arrived at Site 808 at 1800 hr on 18 May. During the transit the drill crew slipped and cut the drill line. The seafloor positioning beacon was deployed at 1937 hr. The precision depth recorder indicated a water depth of 4674.5 meters below sea level (mbsl), or 4685.4 meters below rig floor (mbrf). The vessel was offset 1 km west (upcurrent) to allow assembly of the casing while the ship drifted with the current. The reentry cone was positioned on the moonpool door. The drill floor was rigged up to run 20-in casing, and the drill crew started running the 20-in casing at 2215 hr on 18 May. The casing string included a shoe joint (10.63 m), 12 joints of casing, and a short (pup) joint of casing attached to the casing hanger. The casing running tool was attached to the casing hanger. A compound (Baker-Loc) was applied to each threaded connection to ensure that it did not come apart, and all casing connections were tack-welded. The casing was lowered and latched into the reentry cone by 0515 hr on 19 May. We then assembled the drilling bottom-hole assembly (BHA) that included an 18½-in drill bit, a 22-in underreamer (Smith Service 15000 DTU), a positive-displacement mud motor (Drilex Model D825MSHF), 16 drill collars, and the casing running tool. The drilling BHA was lowered into the reentry cone and casing and was latched into the casing hanger. The casing, reentry cone, and drilling BHA were deployed through the moonpool at 0900 hr on 19 May. The drilling BHA (160.14 m) extended 3.54 m beyond the casing assembly (156.60 m).

The casing, reentry cone, and drilling BHA had been lowered to 3606.9 mbrf by 1500 hr on 18 May. The vibration-isolated television frame (VIT) camera was deployed, and we continued lowering the pipe to 4646.1 mbrf, where we spaced out the drill pipe in preparation to spud. Hole 808H was spudded at 1805 hr on 18 May. The casing was drilled into the seafloor from 0 to 126.7 mbsf (4685.0–4811.7 mbrf). While drilling ahead, we circulated sepiolite mud sweeps at 4710, 4735, 4780, 4792, 4802, and 4811 mbrf.

At 0230 hr on 20 May the downhole positive-displacement motor (mud motor) that provides rotational torque to the underreamer and drill bit appeared to stop working. At 0430 hr, we decided to pull the casing and reentry cone back up to the ship and replace the mud motor. The bit cleared the seafloor at 0615 hr on 20 May. The pipe trip continued until 0645 hr, when we began to recover the VIT camera; the pipe trip resumed at 0815 hr. The casing and reentry cone were set on the moonpool doors at 1625 hr. After unlatching the running tool from the casing, the BHA was taken apart until the mud motor was reached.

The mud motor was tested from 1800 to 1830 hr. The mud motor would not rotate when we pumped seawater through it at 165 gallons per minute (gpm) at 1025 psi. Testing prior to drilling operations showed that it freely rotated at 275 gpm with 125 psi. The mud motor was laid down, and the drill bit cleared the rig floor at 1910 hr on 20 May, ending Hole 808H.

Hole 808I

After its installation at 1915 hr on 20 May, the backup mud motor was successfully tested with circulation rates of 25 strokes per minute (spm) at 50 psi, 50 spm at 225 psi, and 70 spm at 450 psi. The BHA and casing running tool were attached to it, and the entire assembly was lowered and latched into the casing and reentry cone; it was deployed through the moonpool at 2205 hr.

When the bit was at 3809.2 mbrf, the VIT camera was deployed. We continued tripping down to 4646.1 mbrf, where we spaced out the drill string in preparation to spud. Hole 808I was spudded at 0720 hr; the seafloor depth was 4686 mbrf. We successfully drilled the casing down to 160.1 mbsf (4845.1 mbrf). The average drilling parameters were a weight on bit (WOB) of 5–15 klb and a flow rate of 400–550 gpm (80–110 spm) with 900–1150 psi.

The casing running tool was released at 2110 hr on 21 May, and the bit cleared the seafloor at 2245 hr on 21 May. When the drill string had reached 4588.6 mbrf, the VIT camera was retrieved. With the bit at 124.1 mbrf, the casing running tool was removed, the BHA was disassembled, and the mud motor and underreamer were flushed with freshwater.

On 22 May at 1245 hr, the LWD/MWD (measurement while drilling) BHA was made up with a new 9⅞-in bit. The MWD mud pulse communications were tested with a flow rate of 305 gpm (61 spm). The trip down to the seafloor started at 1630 hr; the VIT camera was launched at 0030 hr when the bit had reached 4309.0 mbrf. While the VIT camera was being lowered, the drill crew slipped and cut the drill line. The drill string was tripped to 4654.1 mbrf, and we started searching for the reentry cone at 0315 hr on 23 May. The cone was successfully reentered at 0345 hr. The LWD/MWD tools were lowered from mudline (4686 mbrf) to 141.4 mbsf (4827.4 mbrf). After the VIT camera was retrieved at 0630 hr, the drill string was lowered to 160.1 mbsf (4846.1 mbrf). We began LWD/MWD logging/drilling at 0745 hr on 23 May.

The goal was to log/drill at a controlled rate of 50 m/hr. With connection times, the average rate of penetration (ROP) from 4846.1 mbrf (160.1 mbsf) to 5214.5 mbrf (528.5 mbsf) was 22.9 m/hr. Sepiolite mud sweeps (15 bbl) were pumped at 329, 413, and 471 mbsf to help remove cuttings and improve hole conditions. The drilling parameters used were a WOB of 5–20 klb, torque of 175–225 A, and a flow rate of 67 spm (327 gpm) with 1250–1350 psi standpipe pressure.

On 24 May, the logging/drilling continued from 5214.5 mbrf (528.5 mbsf) to 5435.7 mbrf (749.7 mbsf), and the average ROP dropped to 21.0 m/hr. Twenty-barrel sepiolite mud sweeps were circulated at 557 and 634 mbsf, with a 30-bbl sweep at 749 mbsf.

Before continuing deeper into the hole, a wiper trip was made to determine hole conditions from 5435.7 mbrf (749.7 mbsf) to the casing shoe at 4846.1 mbrf (160.1 mbsf). The drill string was pulled with the top drive to 5230.7 mbrf (544.7 mbsf) with a maximum overpull of 20 klb and torque of 400 A. The top drive was then removed and the string was pulled to 4827.4 mbrf (141.4 mbsf). The drill string was tripped back to 5256.5 mbrf (570.5 mbsf), where we picked up the top drive and reamed down to 5435.7 mbrf (749.7 mbsf). One tight spot was encountered at 5413 mbrf (727 mbsf).

Logging/drilling then continued from 5435.7 mbrf (749.7 mbsf) to 5474.3 mbrf (788.3 mbsf). The average ROP dropped to 15.7 m/hr as a result of the wiper trip and the time needed to make pipe connections. One 30-bbl sepiolite mud sweep was circulated at 759 mbsf. The drilling parameters were a WOB of 15–20 klb at 60 revolutions per minute (rpm), torque of 200–300 A, and a flow rate of 67 spm (327 gpm) with 1500 psi standpipe pressure.

On 25 May, LWD/MWD logging/drilling continued from 5474.3 mbrf (788.3 mbsf) to 5676.3 mbrf (990.3 mbsf). Sepiolite mud sweeps (20 bbl) were circulated at 846, 923, and 968 mbsf.

The décollement zone was encountered at 5654 mbrf (968 mbsf). We experienced drilling problems (high torque and high pump pressures) from 1115 to 2245 hr. Efforts to improve hole conditions included circulation, mud sweeps, and reaming up and down with the drill string. A short wiper trip was made from 5676.3 mbrf (990.3 mbsf) to 5615.4 mbrf (929.4 mbsf). During the wiper trip, the maximum overpull was 25 klb, maximum torque was 550 A, and the maximum pump pressure was 2200 psi.

Logging/drilling operations continued from 5676.3 mbrf (990.3 mbsf) to 5695.5 mbrf (1009.5 mbsf). The average ROP dropped to 13.3 m/hr as a result of connection times, hole conditioning, and the wiper trip. The LWD/MWD logging/drilling parameters were a WOB of 15–20 klb at 60 rpm, torque of 275–350 A, and a flow rate of 67 spm (327 gpm) with 1550 psi standpipe pressure. Sepiolite mud sweeps (20 bbl) were pumped at 958, 961, and 990 mbsf. Another wiper trip was made from 5695.5 mbrf (1009.5 mbsf) to 5615.4 mbrf (929.4 mbsf).

Most of 26 May was spent fighting the poor hole conditions, making wiper trips, and troubleshooting an overheating top drive. LWD/MWD logging/drilling extended from 5695.5 mbrf (1009.5 mbsf) to 5743.6 mbrf (1057.6 mbsf). The LWD/MWD logging/drilling parameters were a WOB of 15–20 klb at 60 rpm and torque of 275–350 A with a maximum of 600 A. The pump pressure was 60 spm (300 gpm) with 1550 psi standpipe pressure. At 2330 hr the drill string became stuck with the bit at 5702.1 mbrf (1016.1 mbsf). We were unable to rotate the drill string or move it up or down. Rotation and movement were successfully regained at 0045 hr on 27 May. We decided not to continue operations in this hole and began to trip out using the top drive for rotation and circulation up to 5432.7 mbrf (746.7 mbsf). The top drive was removed, and the bit cleared the seafloor at 0615 hr. The drill collars were racked back in the derrick, and the LWD/MWD logging tools were laid down. The drill bit cleared the rig floor at 1710 hr on 27 May, ending Hole 808I. The thrusters and hydrophones were raised, and the seafloor positioning beacon was turned off. We began the transit to Kochi at 1715 hr on 27 May.

Heave Compensation Experiments

At Site 808 we used the MWD tool to measure downhole drilling parameters, including downhole WOB, torque, and bit bounce. Given the strong MWD pressure signals obtained at the surface during Site 1173 MWD operations, we increased the MWD data transmission rates at Site 808 to 6 bits/s. Surface data from the RIS, including surface rotations per minute, torque, WOB, ship heave, pitch, and roll, were recorded synchronously. Ship heave was between 0.5 and 1.5 m during drilling at this site.

Eight experiments were conducted while drilling ahead with the AHC off (4917.2–4946.0, 5013.2–5032.1, 5118.6–5137.9, 5214.5–5233.7, 5320.2–5349.1, 5416.5–5435.7, 5522.3–5541.6, and 5724.4–5734.0 mbrf). One of these intervals (5522.3–5541.5 mbrf) was partially drilled with the AHC preloaded at a set surface weight to evaluate this practice in comparison to similar tests conducted at Site 1173. The comparison of downhole MWD parameters with the surface information will be analyzed postcruise to evaluate the shipboard heave compensation system and to compare drilling conditions with those encountered at Site 1173.

Transit from Hole 808I to Kochi, Japan, and Kochi Port Call

The 96-nmi transit to Kochi, Japan, began at 1718 hr on 27 May and ended at 1118 hr on 28 May. Because the local port authorities would not allow the vessel into the harbor before 1130 hr, the harbor pilot was aboard at 1126 hr, and the first line ashore was at 1230 hr. After customs and immigration formalities were completed at 1345 hr, 20 scientific staff members departed and 9 boarded the ship. The afternoon was filled with public tours for local television stations, newspapers, government officials, Kochi University officials, and university students. Nearly 100 people toured the ship.

At 1345 hr, we began offloading the LWD/MWD tools, 10 joints of 20-in casing, 30 joints of 10¾-in casing, a broken mud motor, a 22-in underreamer, a broken air conditioner compressor, and three-dimensional seismic computer work stations. Equipment loaded included food, scientific equipment for the ACORK and thermistor experiments, 64 joints of 4½-in casing, nine external casing packers, 11 joints of 10¾-in screened casing, two ROV platforms, one replacement mud motor (Drilex 7¾ in), inner core barrels, 10¾-in casing centralizers, 4½-in casing centralizers, one 30-ft knobby drill pipe, one 20-ft knobby drill pipe, one tapered drill collar, one pup joint of 16-in casing, one 16-in casing hanger, and a few steel I-beams. Loading/offloading operations were completed at 0330 hr on 29 May, and the equipment and casing were stored and secured for departure. After the port call, we returned to Site 1173 for ACORK operations.

Hole 808I ACORK Operations

After finishing ACORK operations in Hole 1173B, we returned to Hole 808I. Despite the short distance between Sites 1173 and 808, we were unable to transit in dynamic positioning (DP) mode while tripping the pipe because of the current. We arrived back at Hole 808I at 0140 hr on 14 June after a 1.5-hr transit. The seafloor positioning beacon was turned on at 0240 hr. Because of our drill pipe loss at the end of Hole 1173B, our operations began with retrieving 75 additional joints of 5-in drill pipe from the riser hold, making them up into stands, and putting them in the drill pipe racker.

During LWD/MWD drilling earlier in the leg, Hole 808I had been drilled with a 9⅞-in bit to 5743 mbrf (1057 mbsf). Our next step in preparing this hole for an ACORK was to open the existing 9⅞-in hole to 17½ in. A drilling BHA was assembled with a 9⅞-in pilot bit and a 17½-in hole opener. The aluminum pipe protectors were removed from six joints of 5½-in drill pipe so that these joints could be used as transition joints in the BHA. Once this was assembled, the bit was lowered to 4380 mbrf, and the VIT camera was deployed at 2115 hr on 14 June; the drill line was slipped and cut while the camera was being lowered. At 2315 hr we resumed lowering the drill string until it reached 4669 mbrf, where it was spaced out for reentry.

We began the search for the reentry cone at 0000 hr on 15 June. Hole 808I was reentered at 0210 hr. Once we were in the hole, the drill pipe was lowered to 4812 mbrf (126 mbsf), and the top drive was picked up at 0345 hr. The VIT camera was retrieved; at 0615 hr we started drilling ahead at 4846 mbrf (160 mbsf). Twenty-barrel mud (sepiolite) sweeps were pumped every 40–50 m. The hole opening continued until we reached a total depth of 975.3 mbsf at 2025 hr on 17 June. The net penetration rate for the last 24 hr of drilling was ~10 m/hr. The driller noted tight spots from 5632.0 mbrf (946.0 mbsf) to 5660.0 mbrf (974.0 mbsf). Drilling parameters were a WOB of 10–20 klb, 60–70 top drive rpm, 200–350 A torque, and 130 spm at 1600–1700 psi.

We circulated a 40-bbl mud sweep and then started pulling out of the hole. The top drive was racked back at 0430 hr on 18 June when the bit reached 5129 mbrf (443 mbsf). As the pipe trip continued, tight spots were encountered from 4985 mbrf (299 mbsf) to 4971 mbrf (285 mbsf) and around 4956 mbrf (270 mbsf), which required up to 30 klb overpull. No additional problems were encountered and the bit cleared the seafloor at 0730 hr on 18 June. The bit cleared the rotary table at 1555 hr.

After the drilling tools were secured, we began moving the ship ~70 nmi upcurrent (west-northwest; ~250°) to begin assembling the ACORK. The transit began at 1600 hr on 18 June. During the transit, the drill floor crew prepared to run the 10¾-in ACORK casing. As soon as the transit ended at 0000 hr on 19 June, we began assembling the ACORK.

The first screen joint was moved to the rig floor; a casing collar was welded to the bottom pin connection to act as a guide shoe. The lowermost packer was made up as the second joint in the string, and a single ¼-in stainless steel tube was run from the top of the screen to the bottom of the packer. The hydraulic umbilical was started at the top of the lowermost packer. As the casing, screens, and uppermost packer were assembled, hydraulic connections were made at the top and bottom of each screen and packer. Three centralizers were added to each joint, and the umbilical was strapped to the casing near each centralizer with ⅝-in metal banding.

During the remainder of 19 June, 68 additional joints of 10¾-in casing and five more screen joints were added to the ACORK assembly. From 0000 to 0500 hr on 20 June, eight more casing joints, one packer, and the landing joint were added to the string. At 0500 hr the casing running tool, ACORK head, and ported sub assembly were moved to the rig floor and attached to the top of the landing joint. The total length of the ACORK assembly was 964.3 m. The completed ACORK assembly was lowered below the rig floor and hung off the moonpool doors by 0700 hr on 20 June.

The next step was to assemble the drilling BHA that would pass through the ACORK assembly, allowing the bit and underreamer to extend below the guide shoe on the bottom of the ACORK. First, we had to remove the crossover subs that came with the mud motor, as they had 7⅝-in instead of 6⅝-in connections; an ODP crossover sub connected the mud motor to the 8¼-in drill collar above. We then discovered that the crossovers for the underreamer were incorrectly listed in inventory as 4½-in regular connections and therefore could not be securely made up to those on the underreamer. Because of the previous BHA losses on this leg, no other appropriate crossovers were available, so we welded one of the existing crossover subs directly to the underreamer. The other crossover required the fabrication of a spacer ring to fill a gap between the mating shoulders before it could be welded to the underreamer. A total of 9 hr was required for these modifications.

The remainder of the drilling BHA was assembled without additional problems. The complete drilling BHA contained the following components: a 9⅞-in bit, a bit sub with float valve, three crossover subs, a 17-in underreamer, a crossover sub, a mud motor, a crossover sub, nine 8¼-in drill collars, a crossover sub, 91 joints of 5½-in drill pipe, one 5-ft 5½-in drill pipe pup joint, a crossover sub, a landing saver sub, one 8¼-in drill collar pup joint, a jet sub, a motor-driven core barrel (MDCB) latch sleeve sub, the casing running tool, two 8¼-in drill collars, one tapered drill collar, six joints 5½-in drill pipe, and a crossover sub. The total length of BHA from the running tool to the bit was 975.43 m.

When the drilling BHA was assembled and the casing running tool latched to the ACORK head, the complete assembly was lowered so that the final umbilical connections could be made in the moonpool area. After the ACORK assembly was dipped into the water for purging air from the hydraulic lines, the ACORK assembly and drilling BHA were lowered until the bit was at 1294 mbrf. At 0400 hr the VIT camera was deployed so that we could verify the space out of the underreamer with respect to the bottom of the casing as well as the functioning of the mud motor and underreamer. Once these tests were finished, the VIT camera was recovered at 0545 hr on 21 June. We then lowered the pipe to 3462.2 mbrf, where it was kept during the transit back to the site in DP positioning mode.

During the entire assembly/testing of the ACORK and the drilling BHA, the ship was in a controlled drift back toward Hole 808I. The initial offset from the site was ~70 nmi at 0000 hr on 19 June. We arrived back at Hole 808I at 0330 hr on 22 June.

On 21 June (0620–0645 hr), the *Aso Maru* arrived to deliver two engineers to assist with the thermistor string deployment later in the leg. A number of small packages, fresh fruit, and vegetables were also delivered. Two small pieces of failed drill pipe were offloaded for forensic analysis. Also, during the DP transit back to the site, 113 aluminum pipe protectors were removed from the drill pipe, as they would no longer be used.

We resumed lowering the drill pipe once we were back on site and ran the pipe down to 3798 mbrf, where we stopped to deploy the VIT camera at 0430 hr on 22 June. The pipe trip then continued at 0500 hr. Once the drill string reached 4662 mbrf, it was spaced out in preparation for reentering Hole 808I. After only 20 min, Hole 808I was reentered at 0805 hr on 22 June.

The drill bit/mud motor and casing shoe encountered some resistance passing through the reentry cone hanger at 4686 mbrf. After lowering the drill string to 4842 mbrf (156 mbsf), we began washing and drilling in the ACORK, reaching 5269 mbrf (583 mbsf) at 2400 hr on 22 June. Twenty-barrel mud (sepiolite) sweeps were circulated at 295, 430, 497, 555, and 574 mbsf. The drilling parameters were a WOB of 0–20 klb with a circulation rate of 100–120 spm and a pressure of 1450–2200 psi.

On 23 June, we continued drilling in the ACORK from 5269 mbrf (583 mbsf) to 5452 mbrf (766 mbsf). The VIT camera had to be retrieved at 2030 hr. Twenty-barrel mud (sepiolite) sweeps were circulated at 660, 670, 747, and 764 mbsf. The penetration rate for 22 June was 7.6 m/hr. The drilling parameters were a WOB of 10–20 klb and a circulation of 120 spm with a pressure of 2200 psi.

From 24 to 26 June, the ACORK was advanced from 5452 mbrf (766 mbsf) to 5611 mbrf (925 mbsf) with a penetration rate of only ~2 m/hr. Twenty-barrel mud (sepiolite) sweeps were circulated every 10–20 m. The drilling parameters were a WOB ranging up to ~180 klb and a circulation of 70– 120 spm with a pressure up to 2200 psi.

As the penetration rate was so low and any increase in WOB would cause concern for the safety of the casing and drill string, we decided to deploy the VIT camera at 1400 hr on 26 June and perform some WOB tests. Once the camera was on the bottom at 1615 hr, we noted that the drill string, ACORK head, casing, and reentry cone all appeared to be intact. We then attempted to increase the WOB to the maximum deemed safe and saw no significant increase in penetration or bending of the drill string or ACORK. We also tried to raise the drill string to see if recovering the entire assembly was an option; it could not be raised. During these tests, circulation was observed coming out of the reentry cone, which indicated that, although a flow path existed, the casing was being held by skin friction. The VIT was retrieved at 1950 hr on 26 June.

Because it was clear that we could not pull out of the hole, we continued to try to advance the ACORK in the hope that we could advance enough to either latch it in the reentry cone or get it low enough so that it could remain upright on its own. On 27 June, we advanced from 5611 mbrf (925 mbsf) to 5620 mbrf (934 mbsf) at ~0.4 m/hr. Two 100-

bbl mud sweeps were pumped at 927 and 929 mbsf, as were two 20-bbl sweeps at 931 and 933 mbsf. The drilling parameters were a WOB of 180 klb and a pump rate of 70–120 spm with a pressure of 1000–2200 psi.

From 0000 to 0430 hr on 28 June, we continued to work the drill string, but it would not advance below 5620 mbrf (934 mbsf). In a last-ditch effort, we pumped 500 bbl of heavy (11.3 lb/gal) mud into the hole at 0430 hr and continued to work the pipe until 0730 hr with no success. At this point, we decided to inflate the packers. The circulation sub was shifted open with the wireline-shifting tool. The go-devil was dropped; once it landed, a slow pump rate was used to inflate the two packers and close the spool valves. This was completed at 0900 hr.

We then released the casing running tool at 1100 hr and raised the drill string from 5620 mbrf (934 mbsf) to 5574 mbrf (888 mbsf). Because it seemed unlikely that conditions would allow a bridge plug to be installed, the science party requested heavy mud be placed in the hole, so 100 bbl (10.5 lb/ gal) of mud was pumped into the hole. Tripping operations resumed at 1215 hr, with the top drive being racked back and the 20-ft knobby laid out.

The VIT camera was deployed and run in the hole from 1245 to 1315 hr on 28 June to observe the withdrawal of the drilling BHA from the ACORK head. At 1533 hr the drilling BHA came out of the reentry cone, and the ACORK head slowly bent toward the seafloor and went out of sight (Fig. F31). The drill string and VIT camera were lowered for a closer inspection and the ACORK casing was observed to be bent over the edge of the reentry cone (Fig. F32). With the camera, we followed the casing away from the reentry cone. The compass on the camera indicated the casing fell to the north. No damage was seen to the ACORK umbilical, casing, or head. The ACORK head was lying flat on the seafloor, and ~60% of the ACORK head appeared above the seafloor. Most important, the underwater-mateable connector was sticking straight up so that a submarine or ROV can still connect to download the data.

We started to recover the VIT camera at 1645 hr on 28 June. The drill string was pulled to 4491 mbrf, and knobbies were installed so that the drill string could be hung off during the DP transit back to Hole 1173B. The seafloor positioning beacon was released at 1815 hr. Once the VIT camera was back on board at 1845 hr, the hydrophones were raised and the ship began the DP transit back to Hole 1173B.

After completing the camera inspection at Site 1173 (see **"Operations,"** p. 5, in the "Site 1173" chapter), the drilling assembly used to drill in the Hole 808I ACORK was recovered. The underreamer arms were missing. This likely contributed to our inability to fully lower the ACORK into the hole.

QUALITY OF LWD LOGS

Figure F5 shows the quality control logs for Hole 808I. A target ROP of 50 m/hr was chosen, and the averaged ROP throughout the whole section was 34 m/hr. To record one sample per 15 cm, the ROP must be maintained at 65 m/hr or lower. This was achieved for 99% of the total section in Hole 808I (Fig. F5). Although RAB image resolution would improve with even slower drilling rates, the quality of RAB images is still high (~3-cm pixel) and no significant reduction in resolution is observed.

F5. Quality-control logs, p. 37.

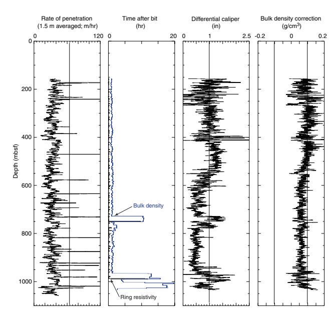

Time-after-bit (TAB) measurements are <1 hr for 99% of the resistivity and gamma ray logs and <3 hr for 90% of the density and neutron porosity logs throughout the whole section (Fig. F5). Density TAB values of 10–20 hr at 728–750, 967–989, and 1003–1028 mbsf coincide with hole conditioning operations (see "Operations," p. 5). The differential caliper (DCAL) is the best indicator of borehole conditions. In typical logging applications a standoff of <1 in between the tool and borehole wall indicates high-quality density measurements with an accuracy of ±0.015 g/cm³. The differential caliper values are <1 in over 65% of the total section in Hole 808I. The differential caliper values in the long TAB intervals at 728–750 and 967–989 mbsf are significantly higher than adjacent intervals. Apparently, the long TAB measurements directly resulted in borehole enlargements and low-quality density measurements. The differential caliper values are <1 in over 30% of the 268- to 530-mbsf interval (log Units 1 and 2; see "Definition of Log Units," p. 13). This interval corresponds to zones of borehole breakouts and the frontal thrust (see "Logs and Structural Geology," p. 18). The bulk density correction (DRHO) shows a trend similar to the differential caliper log and varies from 0 to 0.1 g/cm³ below 530 mbsf and from 0 to 0.2 g/cm³ above 530 mbsf (Fig. F5). Comparisons to core data clearly show that enlarged sections of the borehole yield unreliable density and associated porosity data (see below). Thus, these density and porosity results should be used cautiously until more complete correction and editing is completed postcruise.

As in Holes 1173B and 1173C, raw waveforms from the ISONIC tool were successfully recorded with high signal-to-noise ratios in Hole 808I. Preliminary waveform processing and evaluation of *P*-wave velocities were carried out by Anadrill-Schlumberger in Houston, Texas, during and after Leg 196. The preliminary *P*-wave velocity log (Fig. F29) does not correspond closely with core and other independent values and may be subject to significant errors in *P*-wave phase identification. This log will require continued processing and may be substantially modified postcruise (see "Logs and Physical Properties," p. 23).

DEFINITION OF LOG UNITS AND LITHOLOGIC INTERPRETATION

The uppermost 156 m of LWD data was not used because of the 20-in casing that influenced logs considerably. Below 156 mbsf the following logs are available for a composite log interpretation and a determination of logs units: gamma ray, resistivity, density, neutron porosity, photoelectric effect, and differential caliper.

Because the velocity log was processed after the cruise at Anadrill-Schlumberger in Houston, Texas, it was not available on the ship and thus is not used in the following.

Definition of Log Units

The logs and log units are shown in Figure F6. Four log units and six subunits were defined through a combination of visual interpretation and multivariate statistical analysis (see "Identification of Log Units," p. 9, in the "Explanatory Notes" chapter). The cluster analysis shows four prominent clusters. The calculated cluster log, log units, and log curves are shown in Figure F7. The mean values and standard devia-

F6. Visual interpretation of log units, p. 38.

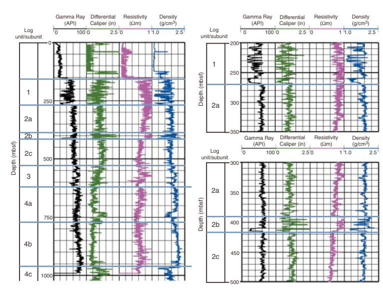

F7. Definition of log units based on statistical analysis, p. 40.

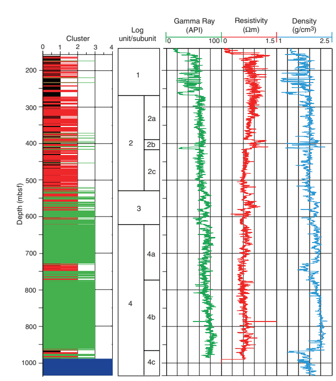

tions of log properties for each log unit or subunit are summarized in Table T2 and Figure F8.

Log Unit 1 (156–268 mbsf) is characterized by the overall lowest mean values of gamma ray (46.5 API), density (1.68 g/cm^3), and photoelectric effect (2.93 b/e$^-$) and overall highest mean values of resistivity (0.84 Ωm) and neutron porosity (0.61 pu). The base of log Unit 1 is defined by positive shifts in the gamma ray and density logs of ~50 API and ~0.4 g/cm^3, respectively.

Log Unit 2 (268–530 mbsf) is divided in three subunits. Log Unit 2 is characterized by constant values of gamma ray (50–70 API) and neutron porosity (0.4–0.7 pu) and a downhole decreasing resistivity log (1 to 0.5 Ωm). This interpretation should be used cautiously because many intervals have differential caliper values >1 in, which suggests that the log data and especially density data may be unreliable. Log Subunit 2a (268–389 mbsf) has relatively high mean values of density (1.88 g/cm^3) and neutron porosity (0.56 pu). The base of log Subunit 2a is placed at the top of an increasing resistivity log trend (from 0.5 to 1.05 Ωm). Log Subunit 2b (389–415 mbsf) may be significantly influenced by a highly variable differential caliper (0.4–2.2 in). Here, all logs have high mean values and high standard deviations: 0.91 ± 0.12 Ωm for resistivity, 3.00 ± 0.28 b/e$^-$ for photoelectric factor, 1.87 ± 0.25 g/cm^3 for density, and 57.6 ± 14.6 API for gamma ray. The base of Subunit 2b is defined by an abrupt decrease in resistivity from 0.85 to 0.65 Ωm. Log Subunit 2c (415–530 mbsf) has a rather low mean value of resistivity (0.63 Ωm). All other logs have similar mean values as those of log Subunit 2a. The base of log Subunit 2c has a significant increase in gamma ray from 65 to 75 API.

Log Unit 3 (530–620 mbsf) is defined by a significant increase of the mean values of gamma ray (68.6 API), density (1.98 g/cm^3), and photoelectric effect (3.15 b/e$^-$). The base of log Unit 3 is defined by an increase in resistivity (from 0.5 to 0.65 Ωm) and gamma ray (from 55 to 70 API).

Log Unit 4 (620–1035 mbsf) is generally characterized by the overall very high values of gamma ray (60–90 API) and density (1.6–2.4 g/cm^3) and the very low values of resistivity (0.4–0.9 Ωm). Log Unit 4 is divided into three subunits: Subunit 4a (620–776 mbsf) is characterized by the highest mean value of photoelectric effect (3.20 b/e$^-$) and a relatively low mean value of resistivity (0.62 Ωm). This log unit shows a slight downhole decrease in gamma ray (from 90 to 60 API), resistivity (from 0.85 to 0.45 Ωm), and neutron porosity (from 0.6 to 0.4 pu). Close to the base of log Subunit 4a (~730 mbsf) the differential caliper increases to >1 in and obviously influences the density log. The base of log Subunit 4a shows a positive shift in the resistivity log from 0.5 to 0.85 Ωm. Subunit 4b (776–965 mbsf) is characterized by high mean values of density (2.17 g/cm^3) and gamma ray (76.5 API) and low mean values of neutron porosity (0.48 pu) and resistivity (0.65 Ωm). The base of log Subunit 4b is defined by a decrease in density (from 2.3 to 1.3 g/cm^3) and resistivity (from 0.65 to 0.55 Ωm). Subunit 4c (965–1035 mbsf) is characterized by very low mean values of resistivity (0.58 Ωm) and density (1.82 g/cm^3) and very high mean values of gamma ray (76.8 API) and neutron porosity (0.53 pu).

T2. Log unit properties, p. 67.

F8. Statistical data for each log unit, p. 41.

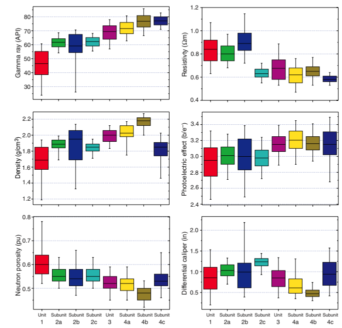

Logs and Lithology

Leg 196 Hole 808I is located ~107 m northeast at an azimuth of 48° from Leg 131 Hole 808C. The core descriptions from Leg 131 Site 808 (Shipboard Scientific Party, 1991) are presented in Figure F9. Each lithologic description that follows is partially reproduced hereafter from the Leg 131 *Initial Reports* volume (Taira, Hill, Firth, et al., 1991). Here only lithologic Units II to IV, which correlate with the defined log units, are described.

F9. Summary of Site 808 log and lithologic data, p. 42.

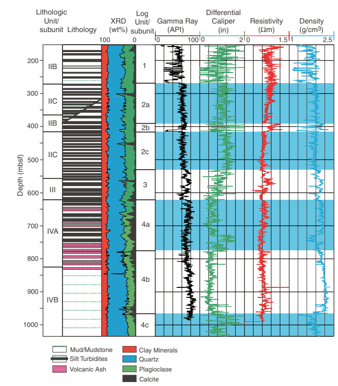

Unit II Trench-Fill Facies (20.55–556.80 mbsf)

Subunit IIA (20.55–120.60 mbsf) is characterized by silty to very coarse grained sands in beds/units showing considerable variation in bed thickness and internal structure. A few very thin (<1 cm thick) ash layers also occur. The sand-rich nature of Subunit IIA, together with its seismostratigraphic position, suggests that it represents axial trench, sandy channel and nonchannel (overbank and sheet) deposits. Hemipelagic settling and fine-grained turbidity currents probably caused sedimentation of muddy interbeds in Subunit IIA.

Subunit IIB (120.60–264.90 and 365.90–409.54 mbsf) comprises very thin to thin-bedded, very fine grained sandstones, the mudstone-pebble conglomerate used as a marker bed, very thin to thin-bedded siltstones, and mud (clayey siltstone/silty claystone). Ash constitutes a minor lithology. The conglomerate provides an important correlative deposit that is duplicated across the frontal thrust zone. The stratigraphic position of Subunit IIB, the relative fine bulk grain size, and thin beds, when compared to overlying Subunit IIA, suggest that it represents axial trench deposits, probably deposited in the outer part of the trench floor.

Subunit IIC (264.90–355.50 and 409.54–556.80 mbsf) is defined from immediately below the matrix-supported, mudstone-pebble conglomerate to the first occurrence of a thick tuff in Hole 808C. Subunit IIC differs from overlying Subunit IIB in that it contains little sand. There are very few ash/tuff layers relative to underlying Unit III.

Unit III Trench–Basin Transition Facies (556.80–618.47 mbsf)

Unit III is defined from the first occurrence of a thick tuff unit to the last ripple-laminated siltstone turbidite in Hole 808C. Unit III is dominated by thoroughly bioturbated clayey siltstone/silty claystone with ash/tuff layers up to 25 cm thick. The stratigraphic position of Unit III, between trench-fill deposits and the predominantly hemipelagic Shikoku Basin deposits, suggests that this unit represents trench–basin transition deposits, perhaps including sediments that were deposited on the outer trench.

Unit IV Shikoku Basin Facies (618.47–1243.00 mbsf)

The characteristic feature of Subunit IVA (618.47–823.74 mbsf) is the abundance of thin layers of tuff and vitric sandstone, intercalated within a thoroughly bioturbated (mottled) mud succession rich in foraminifers. Volcaniclastic beds reach thicknesses up to 20–50 cm. The seismostratigraphic position of Subunit IVA, together with the absence of terrigenous sandy or silty turbidites, suggests that this subunit represents the upper Shikoku Basin deposits dominated by hemipelagic sedimentation and the accumulation of volcanic layers.

The top of Subunit IVB (823.74–1243.0 mbsf) corresponds to the disappearance of the abundant, intact ash/tuff layers and the base corresponds to the appearance of predominantly acidic volcaniclastic deposits. Subunit IVB comprises an essentially monotonous succession of thoroughly bioturbated clayey siltstones and silty claystones with traces of disseminated volcanic glass. The seismostratigraphic position of Subunit IVB, between upper Shikoku Basin deposits and the acidic volcaniclastic unit that rests on basaltic basement, suggests that Subunit IVB represents hemipelagites of the lower Shikoku Basin deposits.

Bulk Mineralogy

The following descriptions of bulk mineralogy are taken from the Site 808 core descriptions (Shipboard Scientific Party, 1991).

Calcite percentages are overall low (0–5 wt%) but there are some intervals (600–880, 950–1000, and 1120–1210 mbsf) with values >10 wt%. The calcite content increase coincides with the lower part of lithologic Unit III and all of Unit IV, which are composed of siltstone turbidite, clayey siltstone/silty claystone with ash/tuff layers (Unit III), and tuff and vitric sandstone, a mud succession, clayey siltstones, and silty claystones (Unit IV).

The overall scatter in quartz content decreases downhole in response to a decrease in the amount and frequency of sediment influx via turbidity currents. The quartz content remains constant between 156 and 850 mbsf in the range of 40 to 55 wt%. At 850 mbsf quartz content increases abruptly to 55–60 wt%, which is caused by silt and ash-rich units in the finer grained hemipelagic facies within lithologic Subunit IVB. Below 850 mbsf the section is characterized by a fluctuation in quartz content.

Plagioclase content decreases continuously downhole from 30 to 20 wt% in response to the decrease in amount and frequency of turbidity currents. There are intervals with higher variability that may reflect sand layers that are typically enriched in plagioclase relative to the muddy interturbidite deposits.

Total clay content is constant from 156 to 860 mbsf in the range between 10 and 25 wt%. Below 860 mbsf clay mineral content varies.

Correlation of Lithologic Units with Log Units

The depth boundaries differ between the log and lithologic units because casing influenced the logs significantly; thus the interval between 0 and 156 mbsf is not used to determine log units.

The interval from log Unit 1 through Subunit 4b shows overall increasing trends in gamma ray and density, which suggests an increase in clay content with depth.

Log Unit 1 (156–268 mbsf) coincides with lithologic Subunit IIB (120.6–264.9 mbsf), which consists of very fine grained sandstones, siltstones, and clayey siltstone/silty claystone. The very low gamma ray and density values confirm the coarse-grained lithology described in the cores. The mudstone-pebble conglomerate mentioned in the core description as a marker for the base of lithologic Subunit IIB is observed in the logs at the base of log Unit 1 at ~260 mbsf, where gamma ray, resistivity, and density are characterized by very low values and neutron porosity by very high values.

Log Unit 2 is divided into three subunits. Log Subunits 2a and 2c are both characterized by similar trends and value ranges of gamma ray, density, photoelectric effect, and neutron porosity. Additionally, log Subunit 2a (268–389 mbsf) shows positive shifts in the gamma ray and density logs and a negative shift in the neutron porosity log compared to log Unit 1. Log Subunit 2a is equivalent to the upper segment of lithologic Subunit IIC (264.9–365.9 mbsf), which is composed of a mudstone-pebble conglomerate and the first occurrence of a thick tuff. Lithologic Subunit IIC contrasts with overlying Subunit IIB in containing little sand, which is reflected in higher gamma ray values. Log Subunit 2b (389–415 mbsf) is defined by its high variability of LWD data, which may be caused by large borehole washouts indicated by the high differential caliper values. The density, resistivity, and photoelectric effect logs are characterized by high values. Log Subunit 2b coincides with the lower part of lithologic Subunit IIB (365.9–409.54 mbsf), which comprises very fine grained sandstones, mudstone-pebble conglomerate, siltstones, and mud (clayey siltstone/silty claystone). The pronounced drop in gamma ray values at the base of log Subunit 2b may mark the mudstone-pebble conglomerate noted at ~409 m in the cores and may correlate to a similar log signature at the base of Log Unit 1. Log Subunit 2c (415–530 mbsf) coincides with lithologic Subunit IIC (409.54–556.80 mbsf), which consists of silt turbidites and hemipelagic mudstones.

Log Unit 3 (530–620 mbsf) coincides with lithologic Unit III (556.80–618.47 mbsf), which is composed of clayey siltstone/silty claystone with ash/tuff layers. Log Unit 3 is characterized by high gamma ray, density, and photoelectric effect and an overall high variation of values.

Log Subunit 4a (620–776 mbsf) coincides with lithologic Subunit IVA (618.47–823.74 mbsf), which consists of ash/tuff, sandstone, and hemipelagic mud. Log Subunit 4a is characterized by high photoelectric effect and low resistivity values. High photoelectric effect is also probably related to a relatively high carbonate content.

Log Subunit 4b (776–965 mbsf) is characterized by high values of density and gamma ray and low values of neutron porosity and resistivity. The transition between log Subunits 4b and 4c is defined by a decrease in density and photoelectric effect and an increase in neutron porosity and resistivity. Log Subunit 4b is equivalent to the lower part of lithologic Subunit IVA (618.47–823.74 mbsf) and the upper part of lithologic Subunit IVB (823.74–1243 mbsf). The lower part of log Subunit 4b represents the décollement zone identified at Leg 131 Site 808.

Log Subunit 4c (965–1035 mbsf) is characterized by low values in resistivity and density and high values in neutron porosity and gamma ray. This log subunit coincides with the lower part of lithologic Subunit IVB.

Lithology and Log Comparison

The crossplot of gamma ray vs. photoelectric effect reflects the change in lithology according to log units (Fig. F10A). These two logs were used because of a lower sensitivity to sediment compaction than density and resistivity logs. Overall, a positive correlation between gamma ray and photoelectric effect is observed. A continuous increase in gamma ray and photoelectric effect is observed from log Unit 1 which reflects the increase in clay and calcareous content. The data of log Units 2, 3, and 4 overlap significantly, which shows the similarity of their sediment composition. High gamma ray values reflect a high clay

F10. Crossplots of log properties, p. 43.

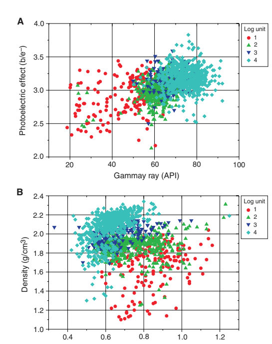

content and a low content of material such as sand and silt, which fits quite well with lithologic descriptions. In contrast, log Unit 1 is characterized by much lower gamma ray values, which coincides with a higher sand content.

The crossplot of resistivity vs. density shows the increasing compaction with depth (Fig. **F10B**). The entire data set shows no apparent correlation between resistivity and density (correlation coefficient = –0.03). However, focusing in detail log Units 3 and 4 are characterized by a positive correlation (+0.52 and +0.54, respectively), whereas log Units 1 and 2 show no clear correlation (+0.19 and +0.18, respectively). Overall, the four log units differentiate well. This is based on a continuous increase in density and a slight decrease in resistivity with depth.

LOGS AND STRUCTURAL GEOLOGY

Structural data were determined from RAB images using Schlumberger's Geoframe software. Full details of structural interpretation methods from resistivity images are outlined in **"Interpreting Structure from RAB Images,"** p. 9, in the "Explanatory Notes" chapter. Structural interpretations reported here were made using RAB images of medium-focused button resistivity, which images at a penetration depth of 3 in (7.6 cm). Comparisons between shallow-, medium-, and deep-focused resistivity images indicated little variation for structural analysis. In situ stress orientation measurements determined from borehole breakouts utilized all three depth images (shallow, medium, and deep).

Hole 808I successfully penetrated both the frontal thrust and décollement zones in the toe of the accretionary prism, allowing detailed structural analysis of these zones and the state of deformation between them. Unfortunately, insufficient penetration of the underthrust section below the décollement zone prevented structural analysis of this zone. In addition, strong borehole breakouts were recorded in the RAB images throughout much of the hole, allowing an initial determination of in situ horizontal stress orientation at Hole 808I and direct comparison with other structural data. An increase in deformation and fracturing is noted at Site 808 in comparison with reference Site 1173. Direct comparisons with structural data from core analysis of Leg 131 Site 808 reveal many similarities. The frontal thrust and décollement zones are easily identified and correlated and, in addition, several more minor fractured intervals can be correlated between Leg 131 cores (Shipboard Scientific Party, 1991) and Leg 196 RAB images (Fig. **F11**). Methods for interpreting structure and bedding differ considerably between Legs 131 (core analysis) and 196 (RAB image analysis) (see **"Interpreting Structure from RAB Images,"** p. 9, in the "Explanatory Notes" chapter). This should be considered when comparing the two data sets directly.

F11. Leg 196 fracture dip and strike and Leg 131 core fracture frequency, p. 44.

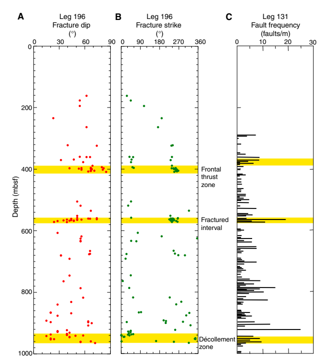

F12. RAB image of all interpreted fractures, p. 45.

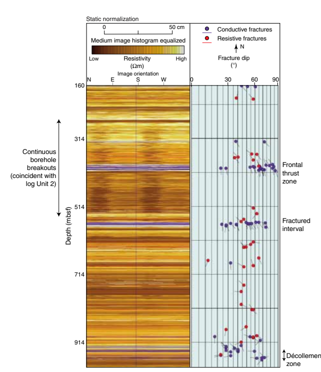

Interpretation of Hole 808I RAB Images

Fractures were differentiated according to resistivity as conductive vs. resistive (Fig. **F12**). Conductive fractures are generally confined to major deformation zones and are interpreted to represent open fractures or alternatively fault planes coated with conductive pyrite (as tentatively identified on small fault planes through XRD analysis at Leg 131 Site 808; Shipboard Scientific Party, 1991). Resistive fractures occur mostly between distinct deformation zones and may signify increases in fault gouge (low-conductivity clays), brecciation, or mineralization (although a complete absence of mineral veining was noted in Leg 131 cores). Deformation zones are characterized by generally high resistivity, possibly signifying intense deformation and brecciation with microfaulting (microfaulting is unidentifiable at the resolution of RAB images) or porosity collapse due to overall compactive deformation, cut by discrete conductive fractures (e.g., Fig. F13).

F13. RAB image of the frontal thrust zone, p. 46.

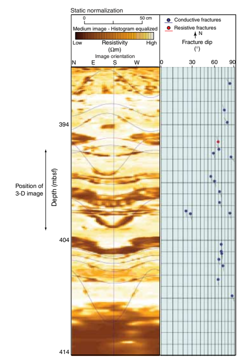

Fractures

As expected, an increase in deformation and fracturing is noted at Site 808 in comparison with reference Site 1173. Fracture frequency (Figs. F11, F12) increases significantly at major deformation zones, such as the frontal thrust zone (~400 mbsf), a major fractured interval at ~560 mbsf, and the décollement zone (~940–960 mbsf). These zones also correspond to increases in deformation seen in Leg 131 Site 808 cores. Fractures at the RAB image scale are relatively sparse between these zones. Deformation (in the form of identifiable fractures) is almost absent between the frontal thrust zone and the fractured interval at 560 mbsf, whereas an increase in background fracture frequency (predominantly resistive fractures) occurs below this depth. These trends are in agreement with patterns of fault frequency recorded at Leg 131 Site 808 (Fig. F11).

A dominant fracture strike of ~northeast-southwest (more specifically, east-northeast–west-southwest) is present throughout the borehole (Figs. F11, F14). This trend deviates slightly from the Nankai plate convergence vector of ~310°–315° (Seno et al., 1993; Fig. F14), but this deviation is within the error of RAB azimuth measurements and may be insignificant. This orientation is particularly clear within the major deformation zones (frontal thrust and 560-mbsf fractured interval) but is more variable between them (e.g., above 400 and at 600–900 mbsf; Fig. F11). A dominant strike of north-south occurs within and just above the décollement zone. Fracture dips range from ~25° to 90° with highest dips recorded within the frontal thrust zone. No evidence of displacement was imaged at this site in contrast to Site 1173 where normal offset was observed. The broad range of fracture dips does not rule out any style of faulting. Fracture dip direction shows some variability throughout Hole 808I with distinct patterns developing within the discrete deformation zones.

F14. Stereographic plot and Rose diagram of poles to fracture planes, p. 47.

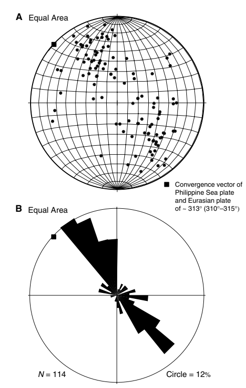

Bedding

Bedding dips are predominantly low angle at Hole 808I (almost all dip <25°), with the majority <5°–7° (the minimum resolvable dip on RAB images collected here, shown as 0° on Fig. F15). The total range of bedding dips is 0°–50°. Increases in bedding dip cannot be correlated with zones of deformation (as was observed at Leg 131 Site 808) as bedding planes were difficult to identify due to masking by a generally high resistivity deformation signature. However, an absence of subhorizontal dips (<5°–7°) is observed within these zones and a slight increase in average bedding dip in their vicinity. Predominantly shallow bedding dips were also observed in Leg 131 core data (0°–15°).

Bedding orientation appears to be fairly random above ~650 mbsf (Fig. F15) but with a more dominant northeast-southwest trend below this depth (particularly within the interval 650–800 mbsf) and a north-

F15. Bedding dip and strike, p. 48.

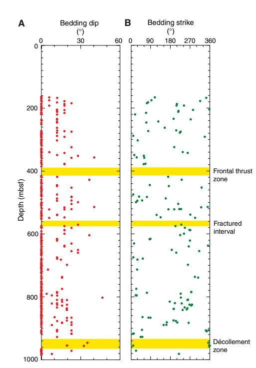

south trend at the décollement zone. This northeast-southwest trend is similar to fracture orientations in the same interval and throughout the borehole (Figs. **F11, F12**). A north-south trend of fractures within the décollement zone is also observed.

Identification of bedding planes and differentiation between fractures and beds was problematic within RAB images at Hole 808I, partly because bedding and fracture strike and dip were likely to be similar at this location within the accretionary prism. In addition, the inaccuracy of bedding strike from low-dipping bedding planes is likely to be high due to the resolution of RAB images. The possibility of misinterpretation of bedding planes and fractures is discussed at length elsewhere (see **"Interpreting Structure from RAB Images,"** p. 9, in the "Explanatory Notes" chapter and immediately below). This is particularly relevant for highly conductive steeply dipping features observed within the frontal thrust zone and the 560-mbsf fractured interval (see **"560-mbsf Fractured Interval,"** p. 21), which may represent conductive open fractures or steeply dipping conductive beds.

Frontal Thrust Zone

The frontal thrust zone (389–414 mbsf) represents the most strongly deformed interval in Hole 808I RAB images and in the cores of Leg 131 Site 808 (Shipboard Scientific Party, 1991). In RAB images, the zone is characterized by overall high resistivity with mostly conductive (open?) fractures (Fig. **F13**). The high resistivity is interpreted as a response to porosity collapse due to overall compactive deformation in the frontal thrust zone. The majority of fractures are oriented ~east-northeast–west-southwest and are south-dipping. A progression from a few north-dipping fractures in the upper part of the deformation zone to dominantly south-dipping in the middle and lower parts of the zone is observed. These south-dipping fractures are antithetic to the northward dip of the main frontal thrust zone (imaged in seismic data). Figure **F16** shows a three-dimensional (3-D) image of part of the frontal thrust zone (location indicated on Fig. **F13**) showing the original cylindrical form of the borehole RAB image and south-dipping conductive fractures. The view is slightly elevated and from the south-southwest (200°). Fractures are mostly steeply dipping (50°–90°) throughout the frontal thrust zone (Figs. **F11, F13**), with significant increases in dip compared to sections above and below. The frontal thrust zone occurs at a slightly greater depth (389–414 mbsf) than at Leg 131 Site 808 (357–395 mbsf), which may reflect, in part, the horizontal separation of the two boreholes.

F16. 3-D RAB image of frontal thrust zone, p. 49.

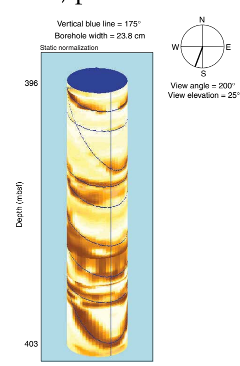

We cannot rule out the possibility that some interpreted fractures within this zone may represent conductive bedding planes within a highly deformed high-resistivity zone, as steeply dipping beds were recognized in this interval at Leg 131 Site 808. However, the anomalously high conductivity of the planar features (relative to the surrounding stratigraphy) suggests that they are mostly fractures. Fractures and bedding are likely to have similar strikes and dips in this interval and are therefore likely to be difficult to differentiate. If the conductive features with progressive changes in dip represent bedding planes, this interval provides evidence for folding. Evidence of folding and steep (50°–90°) to overturned beds was also reported within this zone at Leg 131 Site 808 (pp. 115 and 139 in Shipboard Scientific Party, 1991).

The general northeast-southwest strike of fractures is in agreement with measurements from Leg 131 and with the plate convergence vector of ~310°–315° (Seno et al., 1993). Fracture orientations are specifically closer to an east-northeast–west-southwest trend (Figs. **F11, F13**) as also observed for all fractures within Hole 808I (Fig. **F14**). This orientation deviates slightly from the convergence vector (Fig. **F14**) and orientations of borehole breakouts (described in detail below). However, this deviation may be within the error of RAB orientation and convergence vector measurements.

560-mbsf Fractured Interval

A prominent fractured interval (similar in intensity to the frontal thrust zone ~150 m above) occurs at 559–574 mbsf (Figs. **F11, F12**). This zone is similar to the other major deformation zones at Hole 808I by being characterized by high-conductivity (open?) fractures within a zone of overall high resistivity. Fracture orientations are very similar to those of the frontal thrust zone (east-northeast–west-southwest) and are steeply dipping to the south. Core analysis of Leg 131 Site 808 also revealed an increase in fault frequency at this interval (Fig. **F11**). Initial attempts to identify this apparent fault zone within seismic data across Hole 808I have proved inconclusive. As discussed in **"Frontal Thrust Zone,"** p. 29, we cannot rule out the possibility that several of the conductive features interpreted as fractures may be steeply dipping bedding planes within this interval.

Décollement Zone

In general, the décollement zone and fractured intervals above it show minimal deformation in comparison with the frontal thrust zone and 560-mbsf fractured interval. In the vicinity of the décollement zone, a series of discrete fractured intervals composed of conductive fractures are separated by relatively undeformed sections. This deformed interval occurs between 897 and 965 mbsf, with fractured intervals at 897–904, 937–942, and 959–965 mbsf. This entire deformed zone is characterized by patchy intervals of mottled high resistivity. Analysis of cores from the décollement zone at Leg 131 Site 808 (Shipboard Scientific Party, 1991) observed marked brecciation, which may be represented by the high-resistivity mottled texture at Leg 196 Hole 808I. We define the décollement zone itself as the base of this interval, at 937–965 mbsf (orange dashed lines on Fig. **F17**). The base of the décollement zone is sharply defined as the maximum extent of conductive fracturing (Fig. **F18**) and is marked by changes in physical properties (Fig. **F17**), including a sharp high in density and a low in porosity. The upper boundary of the décollement zone is more difficult to define in RAB images. An alternative interpretation of the décollement zone may constitute only the lowest fractured interval (959–965 mbsf) or it may include the entire deformed 897- to 965-mbsf interval. Our choice of the 937- to 965-mbsf interval is marked by a general increase in fracture frequency and by marked variability in physical properties (Fig. **F17**). The décollement zone as defined from core data at Leg 131 Site 808 showed both clear upper and lower boundaries at 945–964 mbsf (blue lines on Fig. **F17**). The Leg 196 décollement zone (937–965 mbsf) is a slightly broader zone than seen in Leg 131 cores (945–964 mbsf) but the bases of the two zones are coincident. Some of these differences may be in part caused by the 107-m horizontal offset between Holes 808C and 808I. It should also be noted that the discrete fractured inter-

F17. Physical properties of the décollement zone, p. 50.

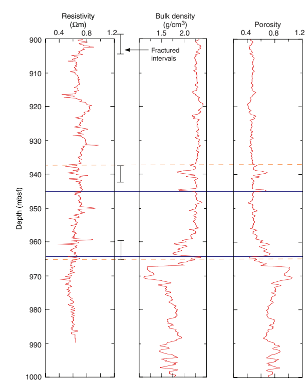

F18. RAB image of the basal décollement zone, p. 51.

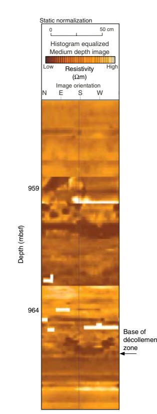

vals (containing conductive fractures) show clear lows in resistivity (e.g., 937–942 and 959–965 mbsf; Fig. F17).

Borehole Breakouts and In Situ Stress

Borehole breakouts were recorded throughout much of Hole 808I and indicate a consistent orientation. Breakouts are indicated by two vertical lines of low resistivity (high conductivity) running along the RAB image (Figs. F19, F20). The high-conductivity breakouts are due to elongation of the borehole in the direction of the minimum horizontal compressive stress orientation (Barton, 2000; σ_2 in this case) and represent the opening or enlargement of the borehole (hence conductive) in this direction. The two breakout "lines" occur opposite each other (~180° apart) in the borehole, indicating a vertical plane. A consistent northeast-southwest orientation is recorded, with an overall range of N30°–70°E down the borehole and an average of N40°–50°E. This trend is consistent with the plate convergence vector of ~310°–315° (Seno et al., 1993), which would be expected to be in alignment with the maximum horizontal compressive stress orientation, σ_1. The orientation of breakouts deviates slightly from the dominant trend of fractures (east-northeast–west-southwest, see preceding discussion and Fig. F14), but whether this deviation is real or within measurement error remains unknown.

In the upper part of the borehole, continuous strong breakouts are recorded between ~270 and 530 mbsf, coincident with log Unit 2 and bracketing the frontal thrust zone (Fig. F12). The development of continuous borehole breakouts through this interval may either be caused by (1) a distinctive stress regime in the vicinity of the frontal thrust zone or (2) the presence of a particular lithology and mechanical state conducive to breakout formation in this interval (see also "Discussion and Synthesis," p. 29). Borehole breakouts occur if the tangential stress exceeds the compressive sediment strength; we, therefore, infer with the latter hypothesis that the strength of log Unit 2 is reduced relative to overlying and underlying lithologies. Below this depth (530 mbsf) borehole breakouts are patchy and intermittent with possible examples of conjugate breakouts, and may be induced by changes in drilling parameters.

Figures F19 and F20 show similarities and differences in breakout patterns between shallow (recorded at 1-in depth from the borehole), medium (3-in depth) and deep (5-in depth) images. Figure F19 shows a decrease in breakout resistivity from shallow to deep, suggesting minimal deformation and invasion 5 in away from the borehole. In contrast, Figure F20 illustrates a consistent resistivity signature in all depth images, suggesting a similar degree of deformation and invasion at 1, 3, and 5 in from the borehole. These differences may be related to variable drilling parameters, but their consistency within certain sections of the borehole and the contrasting resistivity of the two intervals (Fig. F19 images generally high resistivity interbedded sediments, whereas Fig. F20 images low-resistivity sediments) suggests that the degree of breakout invasion may be lithologically controlled.

F19. RAB images of borehole breakouts, 280–325 mbsf, p. 52.

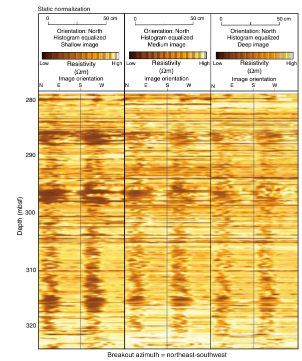

F20. RAB images of borehole breakouts, 460–505 mbsf, p. 53.

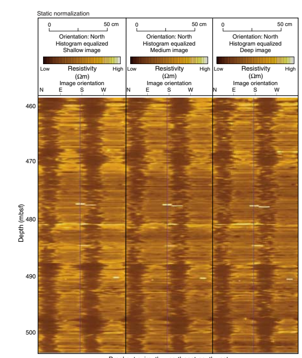

LOGS AND PHYSICAL PROPERTIES

Density

Overall, the LWD density (RHOB) log shows a good fit to the core bulk density (Fig. **F21**). The LWD density log generally underestimates the core values between 0 and 550 mbsf, and overpredicts the core values at 550–970 mbsf, by up to 0.1 g/cm³. LWD density (Fig. **F21**) mostly records the density of seawater between 0 and 156 mbsf where the log was taken inside the 20-in borehole casing. Below 156 mbsf the LWD density log shows a steady increase from ~1.7 to ~1.95 g/cm³ at 389 mbsf (log Unit 1 and Subunit 2a). At the frontal thrust zone (log Subunit 2b) density exhibits large variations associated with fluctuations in the differential caliper, corresponding to the thrust identified between 389 and 415 mbsf in RAB images at Hole 808I, which was also identified in Hole 808C from cores at 357–395 mbsf. Below the frontal thrust zone density decreases sharply, then remains fairly constant at ~1.85 g/cm³ to a depth of ~530 mbsf (log Subunit 2c), where density once more increases steadily to ~2.1 g/cm³ at 725 mbsf. Between 725 and 776 mbsf density drops sharply to ~1.75 g/cm³, corresponding to a period of borehole wiper trips; thus the data may be of questionable quality. Density increases more rapidly from ~1.95 g/cm³ at 776 mbsf to 2.25 g/cm³ at 930 mbsf. From 930 to 965 mbsf it decreases steadily to ~2.15 g/cm³, where it steps down to 1.4 g/cm³. This corresponds to the décollement zone, identified in cores at 945–964 mbsf. Below the décollement zone density increases steadily from ~1.7 g/cm³ at 975 mbsf to ~2.0 g/cm³ at 1034.79 mbsf.

F21. Comparison of LWD and core densities, p. 54.

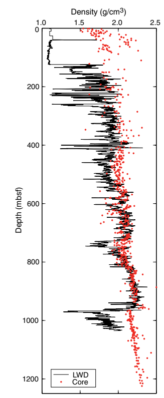

Porosity Calculations from LWD Density Logs

Grain density data from Site 808 core measurements (Fig. **F22**) were used to calibrate a density to porosity transform for the LWD density logs below 156 mbsf. Core grain density measurements indicate changes with depth associated with lithologic variation. Although small-scale trends are observed, the data follow two general trends below 156 mbsf, divided by an abrupt change in grain and bulk density corresponding to the transition from upper to lower Shikoku Basin facies at ~823.7 mbsf. Least-squares regression (Fig. **F22**), after manual removal of low and high density spikes, was used to evaluate these trends in grain density (ρ_g).

F22. Least-squares fits of core grain densities, p. 55.

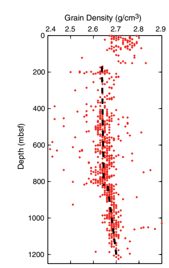

For 156 to 823.7 mbsf,

$$\rho_g = 2.6353 + (1.2065 \times 10^{-5} \times z),$$

and for 823.7 to 1223.79 mbsf,

$$\rho_g = 2.5805 + (1.0 \times 10^{-4} \times z),$$

where z is the depth in meters. Porosity (ϕ) was calculated from the LWD density log values (ρ_b) using

$$\phi = (\rho_b - \rho_g)/(\rho_w - \rho_g),$$

assuming a water density (ρ_w) of 1.035 g/cm³. The resulting porosity (Fig. **F23**) shows an overall slightly steeper gradient with depth than

F23. Comparison of LWD-derived and core porosities, p. 56.

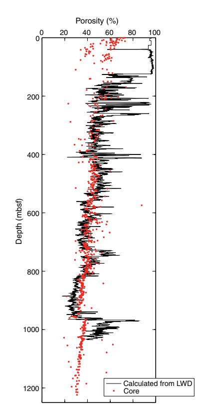

that calculated from cores. Initially, at shallow depths, core data underestimate LWD values, but this trend is gradually reversed around 535 mbsf. Laboratory measurements tend to overestimate porosity (Brown and Ransom, 1996) due to clay-bound water and the rebound of samples from in situ temperature and pressure conditions (Hamilton, 1971). Rebound effects increase with depth. Between 156 and 270 mbsf, where porosity (calculated from LWD density data) shows large fluctuations from 40% to 90%, the LWD-calculated porosity shows mostly higher values than those calculated from cores. Between 270 and 535 mbsf core and LWD porosity are in close agreement at ~45%, except at the frontal thrust zone at ~390–415 mbsf, where LWD porosity fluctuates from 30% to 80%. From 535 to 965 mbsf LWD porosity is increasingly offset from core values, reaching a maximum misfit of ~7% at ~930 mbsf, except from 725 to 750 mbsf, where porosity is artificially high due to the effects of the enlarged borehole caused by the wiper trip (see **"Operations,"** p. 5). At 965 mbsf LWD-calculated porosity increases sharply and is higher than core values by up to 40%, corresponding to the base of the décollement zone. From 970 to 1223.79 mbsf LWD porosity decreases more abruptly than in the cores. Most of the increase in porosity and decrease in density in and below the décollement zone is due to borehole effects (see **"Quality of LWD Logs,"** p. 12).

Comparison of Density and Porosity Results from Sites 1173 and 808

Lithologic units sampled by LWD at Sites 1173 and 808 are of similar composition but at different stages of diagenesis and distances from the influence of tectonic deformation. Comparison of density and porosity results from these sites may provide information on the processes associated with subduction, as primary changes in physical properties are the result of the tectonic forces associated with subduction and formation of the accretionary prism at the Nankai Trough. Below the nearly 400 m of lower slope–apron and trench-wedge sediments at Site 808 (lithologic Units I and II), the trench–basin transition facies (Unit III), although having a greater thickness than its contemporary Subunit IB at Site 1173, exhibits very similar LWD density (Fig. **F24**) and porosity (Fig. **F25**) characters, although with a shift in absolute values. Density shows quite large fluctuations (0.4 g/cm³ at Site 808 and 0.2 g/cm³ at Site 1173) with fairly broad peaks and troughs but no significant average variation with depth (2.0 g/cm³ at Site 808 and 1.7 g/cm³ at Site 1173). The higher density at Site 808 is reflected in the lower porosity (37% at Site 808 and 60% at Site 1173) (Fig. **F25**).

The upper Shikoku Basin facies (lithologic Subunit IVA at Site 808 and Unit II at Site 1173) exhibits a similar trend at both sites, although the wiper trip at Site 808 has somewhat degraded the density data at around 750 mbsf (Fig. **F24**). At Site 1173 the density oscillates by ~0.1 g/cm³ but follows a near constant trend of ~1.66 g/cm³ to a depth of ~200 mbsf, where there is a gradual reduction in density, before returning to a near constant trend of ~1.64 g/cm³. Site 808 conversely has a greater oscillation of ~0.15 g/cm³ and shows a greater offset between the upper and lower near-constant trend, dropping from ~2.11 to 2.06 g/cm³.

The upper part of the lower Shikoku Basin facies (lithologic Subunit IVB at Site 808 and Unit III at Site 1173) shows a very similar density trend at Sites 1173 and 808. At Site 808 there is a gradual increase from ~2.17 to 2.26 g/cm³ just above the décollement zone (930–965 mbsf).

F24. Comparison of densities at Sites 808 and 1173, p. 57.

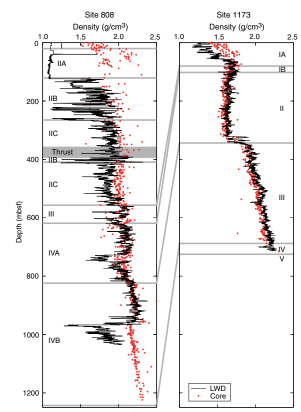

F25. Comparison of porosities at Sites 808 and 1173, p. 58.

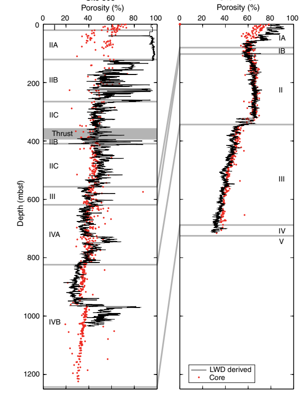

Although no décollement zone is present at Site 1173, density increases from ~1.91 to ~2.0 g/cm^3 in the same lithologic interval. Below the décollement zone at Site 808, LWD density recovers rapidly following reduction at the base of the accretionary wedge, with a trend much steeper than the contemporary sediments at Site 1173. However, the LWD results below the décollement zone at Site 808 are not consistent with core results (Fig. F24), which show a similar trend to LWD and core density at Site 1173.

Resistivity

Figure F26 shows a comparative plot of the five resistivity logs run at this site (see "Logging while Drilling," p. 1, in the "Explanatory Notes" chapter for technical details). Identical downhole trends in resistivity occur in all five resistivity logs and log unit boundaries are clearly identified. As is the case for other parameters from the upper 156 m, logs from this interval did not give meaningful readings, as they were acquired in the 20-in borehole casing. The bit resistivity signal is generally smoother with a smaller degree of variation than other resistivity measurements, but the resolution is lower. Following is a description of each log unit as observed on the ring resistivity log. Log Unit 1 has an average resistivity of ~0.8–0.9 Ωm. After a sharp decrease in resistivity from 1.3 to 0.5 Ωm between 156 and 168 mbsf, the signal shows an increasing trend downward to the log Unit 1/2 boundary. Log Unit 2 is characterized by an overall decreasing trend in resistivity from ~0.9 to ~0.6 Ωm. However, this trend is sharply offset at 389–415 mbsf (log Subunit 2b), where the resistivity values are ~ 0.3 Ωm higher. This zone corresponds to the frontal thrust zone. Log Unit 3 is characterized by a higher degree in variability of the resistivity signal. The variation in the resistivity signal is lower again in log Unit 4. The average value of resistivity in this interval is ~0.6 Ωm. At about the top of the décollement zone (~925 mbsf) in log Unit 4 the resistivity trend changes from gradually increasing to gradually decreasing (Fig. F26).

Figure F27 presents a superposition of the different resistivity measurements to emphasize the differences between bit and ring resistivity on one hand and shallow-, medium-, and deep-focused resistivity on the other hand. There is a noticeable difference in the resistivity values obtained at the bit and at the ring, with the latter being on average 0.05 Ωm higher. The correlation diagram (Fig. F28A) emphasizes this observation. It also shows that the correlation between the two measurement types stays very good throughout the whole section. A superposition of the deep, medium, and shallow button resistivity measurements (Fig. F27) shows good agreement between them. As was observed at Site 1173, shallow resistivity values are systematically higher than both medium and deep resistivity values. This feature is probably related to the measurement conditions and applied corrections. The general shape of the shallow and deep button resistivity correlation diagram (Fig. F28B) confirms this trend.

ISONIC *P*-wave Velocity

As at Site 1173, the preliminary ISONIC *P*-wave velocity values from Hole 808I do not closely correspond to core measurements and previous wireline data (Fig. F29). The preliminary data show a strong tendency for a near-constant value of ~2.2 km/s from ~500 to 1000 mbsf, with excursions to lower values, raising suspicion about log quality.

F26. RAB resistivity logs, p. 59.

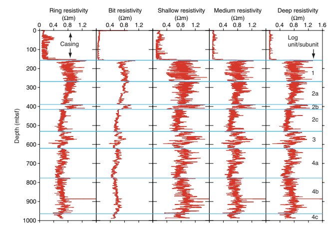

F27. Comparison of ring, bit, and button resistivities, p. 60.

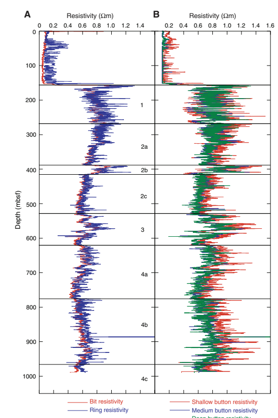

F28. Resistivity correlation diagrams, p. 61.

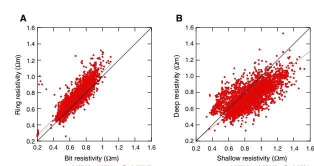

F29. Comparison of ISONIC, core, wireline, and VSP *P*-wave velocities, p. 62

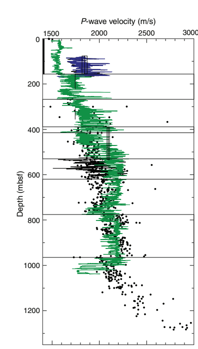

Depth trends also correlate poorly with the density log, except between ~700 and 800 mbsf. All of these observations suggest systematic error in the preliminary coherency analysis and traveltime picks from which the velocity was derived. Further postcruise waveform analysis will be required to derive a reliable velocity log from the ISONIC data.

Summary

1. LWD density logs generally are in good agreement with core bulk density data from Leg 131, slightly underestimating core density down to 550 mbsf and overestimating core density from 550 to 970 mbsf. Poor hole conditions due to frequent wiper trips especially around 750 mbsf and below the décollement zone are clearly reflected in unrealistically low density values.
2. All five resistivity logs show similar downhole trends, clearly delineating the boundaries of all log units. Bit resistivity shows the smallest degree of variability, whereas ring resistivity provides better resolution. Deep-, medium-, and shallow-focused button resistivity measurements are in good agreement, although shallow resistivity is systematically higher than both medium and deep resistivity as at Site 1173.

LOGS AND SEISMIC DATA

Synthetic Seismogram

We generated a synthetic seismogram from Site 808 data using the LWD density and ISONIC velocity curves and a source wavelet extracted from the seismic reflection data as described in **"Core-Log Seismic Correlation and Seismic Resolution,"** p. 10, in the "Explanatory Notes" chapter (Fig. **F30**). LWD densities from Hole 808I were used from 150 mbsf to TD. As the LWD densities from 0 to 150 mbsf were unreliable due to the interference with casing, we used an exponential curve that changed sharply in the near surface from 1.1 g/cm^3 at 0 mbsf to the first measured LWD density value at 150 mbsf. For velocities we used a similar curve for 0–150 mbsf to that used for the densities. The seafloor velocity was set at 1500 m/s, and values were interpolated to the first ISONIC LWD velocity measurement at 150 mbsf.

Figure **F30** shows the fit of the synthetic seismogram with 10 traces on either side of Hole 808I. Although there is a good match at the seafloor in both waveform and amplitude, the synthetic seismogram exhibits a reflectivity series generally inconsistent with the reflectivity in the seismic data. There are several zones where a reflector or sequence of reflectors in the synthetic correlate with the seismic data in depth but not in amplitude and waveform: ~170–270, ~400–450, ~525–640, ~700–750, and ~900–925 mbsf (Fig. **F30**). Although there are mismatches in amplitude and waveform, some of these zones can be correlated to specific log units or to boundaries between them: (1) the base of the ~170- to 270-mbsf sequence of reflections correlates with the log Unit 1/2 boundary, (2) the ~525- to 640-mbsf sequence of reflections correlates with log Unit 3, and (3) the remainder of the synthetic seismogram correlates with log Unit 4. The frontal thrust zone reflection is observed in the synthetic trace at ~400 mbsf, but the amplitude is a factor of 2–3 times higher than the seismic traces nearest the borehole. The décollement zone at ~900–925 mbsf produces a reflection, but it

F30. Summary of synthetic seismogram analyses, p. 63.

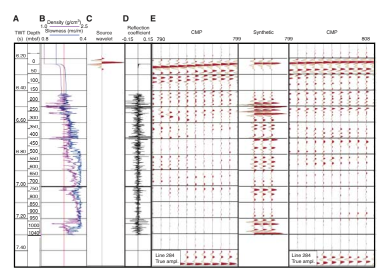

matches poorly with the real data. A sequence of high-amplitude reflections in the synthetic seismogram beneath the décollement zone is not observed in the seismic data.

The match in amplitude and waveform between the synthetic and collected seismic data is notably poor between ~170 and 270 mbsf, between ~750 and 850, and below ~925 mbsf (Fig. **F30**). The interval from ~170 to 270 mbsf exhibits large variations in both velocity and density that produce reflections not seen in the seismic data. The interval between ~750 and 850 mbsf exhibits density values that are unreasonably low and correlates with (1) reflectivity in the synthetic seismogram that is not observed in the seismic reflection data and (2) poor hole conditions as suggested by differential caliper values >1 in. The high-amplitude reflections in the synthetic seismogram below ~925 mbsf are probably caused by inaccurate data acquired as hole conditions quickly deteriorated after penetrating the décollement zone. Some mismatch between the synthetic seismogram and the 3-D data may be caused by the poor quality of the ISONIC log; however, matched reflections at 725 mbsf and below the décollement zone, for example, are produced by the density log.

In summary, beneath the depth of the casing (~150 mbsf) correlations between the synthetic seismogram and seismic reflection data broadly reflect the defined lithologic boundaries or units. However, the details of amplitude and waveform throughout most of the section do not match the seismic data. Amplitudes in the intervals ~200–400 mbsf, ~750–850 mbsf, and below ~925 mbsf are significantly higher in the synthetic section than in the seismic data and are generated by numerous suspiciously low velocity and density values. Production of a more realistic synthetic seismogram awaits careful correction of the density and velocity curves, which now include spurious values.

ACORK INSTALLATION

Precruise planning for the ACORK in Hole 808I emphasized packer and screen placement for long-term hydrogeologic monitoring within two zones: the upper oceanic crust and the décollement zone. The original planned ACORK configuration included five packers and six screens configured to focus on these two zones as follows: (1) a screen at oceanic basement with a packer immediately above and (2) a symmetric four-packer, five-screen array centered on the décollement zone. This was an ambitious plan, a plan that would have involved deployment of the third deepest DSDP or ODP casing ever, focused on the top-priority targets for studying the relationship of fluid flow and deformation at the toe of the Nankai accretionary prism.

During the leg, these plans were modified in accordance with operational realities for two reasons. First, as is fully described in **"Operations," p. 5**, during the LWD operations extremely poor drilling conditions were encountered immediately below the décollement zone. This required the ACORK configuration to be modified to eliminate the basement objective and penetration below the décollement zone. Second, the installation of the 728-m-long ACORK in Hole 1173B encountered increasingly difficult drill-in conditions in the deepest 100 m. A number of hypotheses were considered to explain this behavior and the most likely seemed to be the drag encountered at the upper limit of the lower Shikoku Basin deposits by the array of packers ultimately emplaced across the stratigraphic equivalent of the décollement zone. As the packers are the largest diameter components in the ACORK, we reasoned that limiting the number of packers would be required in the even deeper installation at Site 808.

Given these constraints, a number of options were considered for the actual ACORK configuration in Hole 808I, ranging from a short, four-packer, five-screen installation focused only on the shallow frontal thrust zone to a multipacker, multiscreen configuration at and immediately above the décollement zone. In the end, we decided to utilize six screens and only two packers, one to be set in the 20-in casing and one immediately above the décollement zone. We reasoned that the décollement zone was the most likely zone to be overpressured and therefore the most important zone to isolate with a single packer in the formation. From an operational standpoint, placing the single open-hole packer as deep in the string as possible was thought to minimize the risk during installation, as it would follow as closely as possible behind the underreamer used to run the entire string into place. We also reasoned that the formation would eventually collapse around the other screens not individually isolated by packers.

Hence, the two packers and six screens were assembled in a 964-m-long ACORK string, to emphasize long-term observations of pressures in three principal zones, as follows:

1. The décollement zone and overlying section of lower Shikoku Basin deposits. A screen was placed immediately above the casing shoe, with a packer immediately above the screen. The hole was opened with the intent of emplacing the screen just into the décollement zone, with the packer positioned in a competent zone immediately above the décollement zone. Three other screens were configured above the packer, to span the upper section of lower Shikoku Basin deposits to study the variation of physical properties and propagation of any pressure signals away from the décollement zone.
2. A fractured interval at 560–574 mbsf in the upper Shikoku Basin deposits, as identified in the RAB images (see **"Logs and Structural Geology,"** p. 18). A single screen was intended to be deployed in this zone.
3. The frontal thrust zone centered at ~400 mbsf. A single screen was intended to be deployed in this zone.

As described in more detail in **"Operations,"** p. 5, drilling conditions during installation of the ACORK steadily worsened starting at ~200 m above the intended depth. Despite a heroic effort by the rig crew and application of every available technique, progress stopped 37 m short of the intended installation depth. This left the screen sections offset above the intended zones (Fig. **F1;** Table **T3**), not an ideal installation but still viable in terms of the scientific objectives. In addition, this left the ACORK head 42 m above seafloor, again not an ideal situation because engineering calculations indicated that the exposed ACORK casing string was probably not strong enough to support its own weight. Indeed, when the drill string was pulled out of the ACORK, the VIT camera feed showed the ACORK slowly tipping over within seconds (Fig. **F31**).

But the Nankai dragon was feeling generous or perhaps was sleeping! Amazingly, the exposed ACORK components tipped gently and in the best possible direction. Careful inspection with the VIT camera (Fig. **F32**) showed the casing was not broken but bent continuously over the rim of the reentry cone and a large pile of cuttings. The orientation was

T3. ACORK components and their depths, p. 68.

F31. Video of ACORK fall, p. 64.

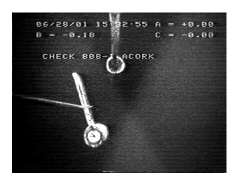

F32. Video of ACORK components lying on seafloor, p. 65.

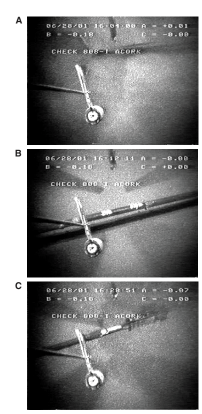

such that the critical hydraulic umbilical was undamaged and the components shown in Figure **F8A** were exposed. This left the data logger and, most important, its underwater-mateable connector in an excellent orientation for future data download by ROV or submersible. Note that the collapse of the above-seafloor section obviously precluded installation of a bridge plug as originally planned, but the bottom of the hole had been filled with heavy mud in anticipation of this outcome (see **"Operations,"** p. 5).

DISCUSSION AND SYNTHESIS

At Site 808, combining data from logs (intermediate-resolution measurements at in situ conditions,) and cores (high-resolution measurements at surface conditions) provides unique views into the processes operating in this active deformation zone (Fig. **F1**). Here we discuss preliminary interpretations from the logging results. These insights will undoubtedly be more focused once the data have been thoroughly processed, especially the density (and derived porosity) and sonic velocity measurements.

Breakouts

The borehole breakouts apparent in the RAB images suggest a maximum principal horizontal stress oriented at ~315°. This correlates well with both the shortening direction determined from the inversion of core-scale faults oriented at 305°–315° (Lallemant et al., 1993) and the convergence direction of ~310°–315° (Seno et al., 1993). The borehole breakouts are best developed bracketing the frontal thrust zone from 270 to 530 mbsf in log Unit 2. The breakouts are thus concentrated in a silty turbidite and hemipelagic mud unit, suggesting that their occurrence is in part lithologically controlled.

Frontal Thrust Zone

The gamma ray log shows two prominent lows at the base of log Unit 1 and near the base of the frontal thrust zone at ~414 mbsf. These log signatures correlate with a conglomerate bed that defined a frontal thrust zone offset of 145 m in the cores (Shipboard Scientific Party, 1991). The offset defined by the gamma ray log lows is ~150 m. The gamma ray low at ~410 mbsf is thinner than the low at 260 mbsf, probably because the former is partially cutoff by the frontal thrust zone that lies in a zone extending from 389 to 414 mbsf.

The frontal thrust zone shows a sharp and sustained increase in resistivity. Because the pore water shows no significant variations in composition through this zone (Shipboard Scientific Party, 1991) it is unlikely that the resistivity increase is caused by differing fluid composition. Rather, the increase in resistivity may indicate a densification of the rock unit caused by compactive deformation. The density curve in this interval shows large variations, with the lower values attributable to anomalously large hole size. However, the higher density values are not suspect and are consistent with densification occurring in the fault zone due to compactive deformation associated with thrusting.

The RAB images show concentrations of high- and low-angle apparent fractures in the frontal thrust zone. The apparent fractures show a mean strike perpendicular to the principal stress orientation estimated from the breakouts.

Décollement Zone and Underthrust Section

The top of the décollement zone, as determined from the RAB images, occurs approximately where the resistivity trend changes from gradually increasing to gradually decreasing. The pore water chemistry around the décollement zone shows no anomalies that would explain the decreasing resistivity trend. The decreasing resistivity trend is presumably a response to the increased amount of fluid-filled, unhealed fractures. Density also decreases over this interval, but part of this change is due to a slight enlargement of the hole and must be interpreted cautiously. Nevertheless, density measurements are consistent with the resistivity data, indicating an increase in bulk porosity over this interval. In contrast, core measurements of density increase in the décollement zone. Therefore, a combination of log and core measurements suggests that the décollement zone is an interval of enhanced porosity, probably fracture porosity, that encompasses blocks of sediment of relatively low porosity and high density. These lower porosity, higher density sediment blocks could have developed during episodic periods of deformation and drainage. Currently the fracture porosity of the décollement zone is probably held open by high fluid pressure, in contrast to the frontal thrust zone, which shows an overall densification and may not be as highly overpressured at present.

The base of the décollement zone and the underthrust sediment contact is marked by a sharp porosity increase that is also observed in cores. This porosity increase is apparent in both density (and derived porosity) and neutron porosity logs, although it is quantitatively suspect because of poor hole conditions.

REFERENCES

Bangs, N.L., Taira, A., Kuramoto, S., Shipley, T.H., Moore, G.F., Mochizuki, K., Gulick, S.S., Zhao, Z., Nakamura, Y., Park, J.-O., Taylor, B.L., Morita, S., Ito, S., Hills, D.J., Leslie, S.C., Alex, C.M., McCutcheon, A.J., Ike, T., Yagi, H., and Toyama, G., 1999. U.S.-Japan collaborative 3-D seismic investigation of the Nankai Trough plate-boundary interface and shallowmost seismogenic zone. *Eos,* 80:569.

Barton, C.A., 2000. Discrimination of natural fractures from drilling-induced wellbore failures in wellbore-image data—implications for reservoir permeability. *Proc. 2000, Ann. Mtg. Soc. Petrol. Eng.,* Paper 58993.

Becker, K., Fisher, A.T., and Davis, E.E., 1997. The CORK experiment in Hole 949C: long-term observations of pressure and temperature in the Barbados accretionary prism. *In* Shipley, T.H., Ogawa, Y., Blum, P., and Bahr, J.M. (Eds.), *Proc. ODP, Sci. Results,* 156: College Station, TX (Ocean Drilling Program), 247–252.

Brown, K.M., and Ransom, B., 1996. Porosity corrections for smectite-rich sediments: impact on studies of compaction, fluid generation, and tectonic history. *Geology,* 24:43–84.

Hamilton, E.L., 1971. Prediction of in-situ acoustic and elastic properties of marine sediments. *Geophysics,* 36:266–284.

Hill, I.A., Taira, A., and Firth, J.V., et al., 1993. *Proc. ODP, Sci. Results.,* 131: College Station, TX (Ocean Drilling Program).

Lallemant, S.J., Byrne, T., Maltman, A., Karig, D., and Henry, P., 1993. Stress tensors at the toe of the Nankai accretionary prism: an application of inverse methods to slickenlined faults. *In* Hill, I.A., Taira, A., Firth, J.V., et al., *Proc. ODP, Sci. Results,* 131: College Station, TX (Ocean Drilling Program), 103–122.

Moore, G.F., 1993. Data report: Vertical seismic profile data, Hole 808E, Nankai Trough. *In* Hill, I.A., Taira, A., Firth, J.V., et al., *Proc. ODP, Sci. Results,* 131: College Station, TX (Ocean Drilling Program), 417–422.

Moore, G.F., Taira, A., Klaus, A., Becker, L., Boeckel, B., Cragg, A., Dean, A., Fergusson, C.L., Henry, P., Hirano, S., Hisamitsu, T., Hunze, S., Kastner, M., Maltman, A.J., Morgan, J.K., Murakami, Y., Saffer, D.M., Sánchez-Gómez, M., Screaton, E.J., Smith, D.C., Spivack, A.J., Steurer, J., Tobin, H.J., Ujiie, K., Underwood, M.B., and Wilson, M., 2001. New insights into deformation and fluid flow processes in the Nankai Trough accretionary prism: results of Ocean Drilling Program Leg 190. *Geochem. Geophys. Geosyst.,* 2:10.129/2001GC000166.

Ransom, B., Spivak, A.J., and Kastner, M., 1995. Stable Cl isotopes in subduction-zone pore waters: implications for fluid rock reactions and the cycling of chlorine. *Geology,* 23:715–718.

Seno, T., Stein, S., and Gripp, A.E., 1993. A model for the motion of the Philippine Sea plate consistent with NUVEL-1 and geological data. *J. Geophys. Res.,* 98:17941–17948.

Shipboard Scientific Party, 1991. Site 808. *In* Taira, A., Hill, I., Firth, J.V., et al. *Proc. ODP, Init. Repts.,* 131: College Station, TX (Ocean Drilling Program), 71–269.

Taira, A., Hill, I., Firth, J.V., et al., 1991. *Proc. ODP, Init. Repts.,* 131: College Station, TX (Ocean Drilling Program).

Figure F1. Site 808 summary diagram showing combined results of Legs 131 and 196. From left to right: depth-converted seismic reflection data, core-based facies interpretation, core recovery, core-based lithologic units and lithology, log gamma ray, core and log density, core and log porosity (computed from the density log using core grain density values), pore water chlorinity, fracture dip from resistivity-at-the-bit (RAB) images, core *P*-wave velocity, log resistivity, log units, and a schematic diagram of the Advanced CORK (ACORK). CDP = common depth point, MWD = measurement while drilling. (See Fig. F7, p. 24, in the "Leg 196 Summary" chapter for an oversized version.) (Continued on next page).

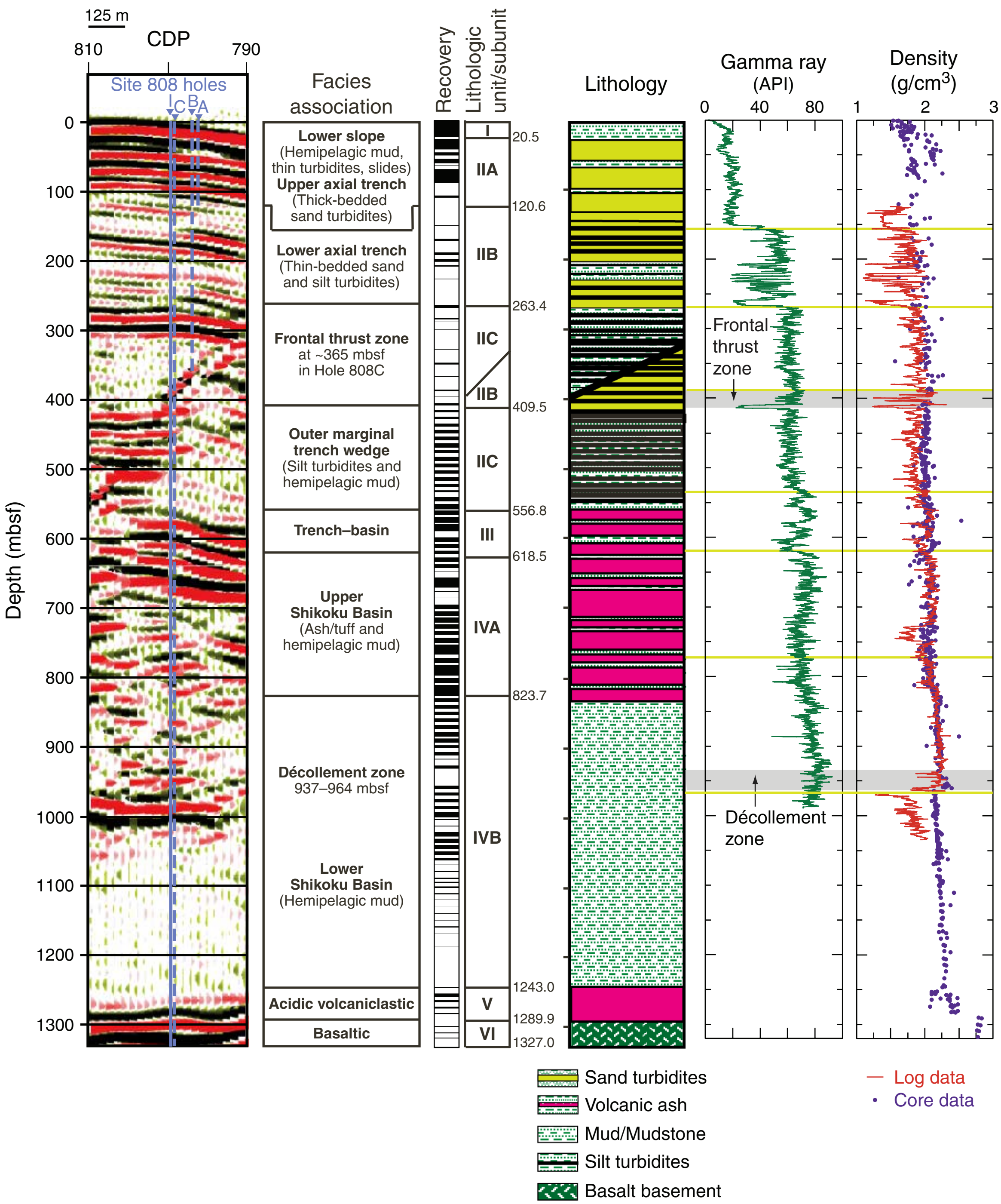

Figure F1 (continued).

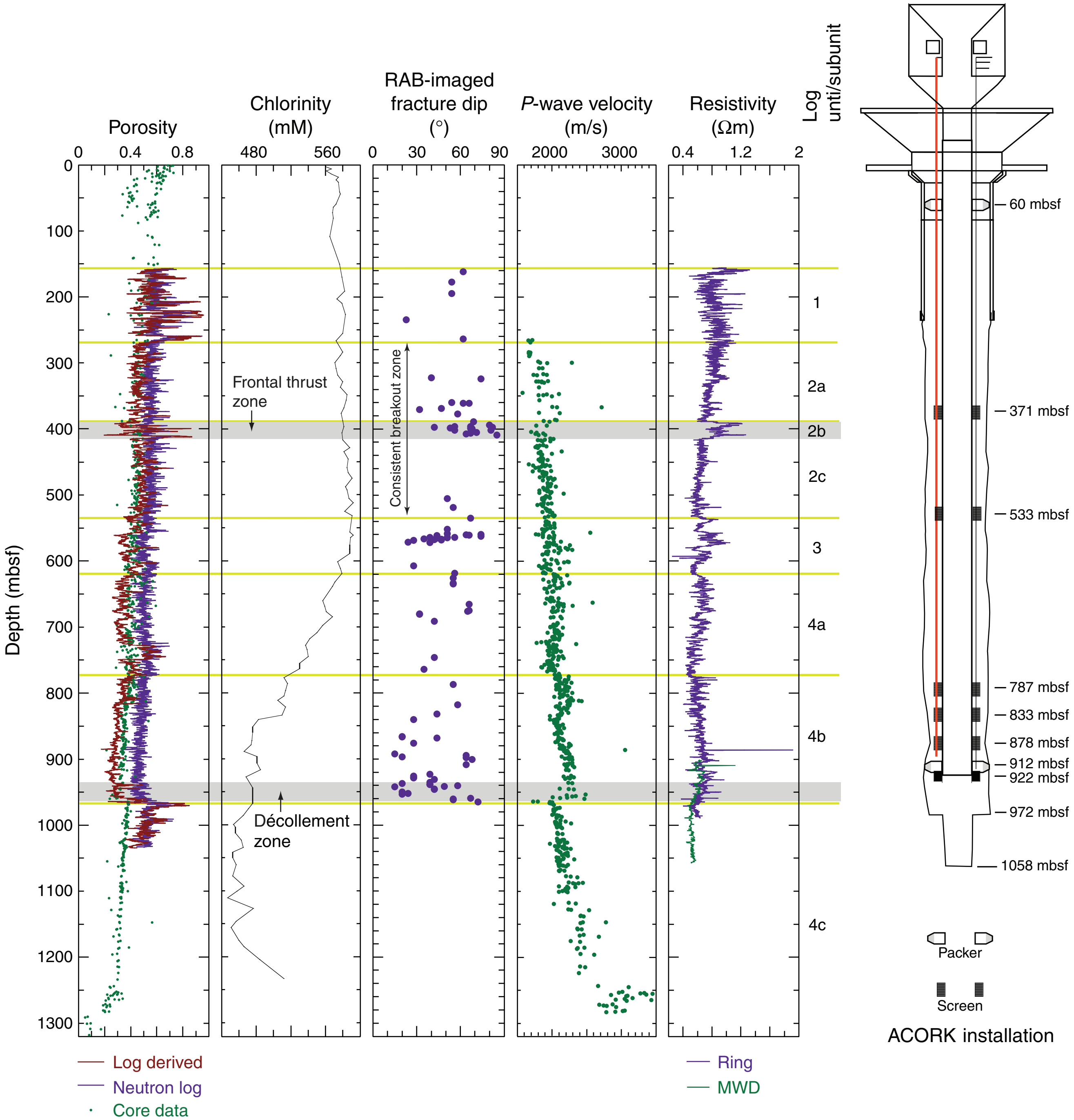

Figure F2. Locations of Leg 196 drill sites (yellow circles with black outlines). Site 808 is located at the seaward limit of the imbricate thrust zone, which is shown by the northeasterly oriented shaded ridges northwest of Site 1174. The line passing through Site 808 shows the location of the seismic profile shown in Figure F3, p. 35. The outlined area shows the extent of the three-dimensional seismic data coverage. Depth contours are in kilometers.

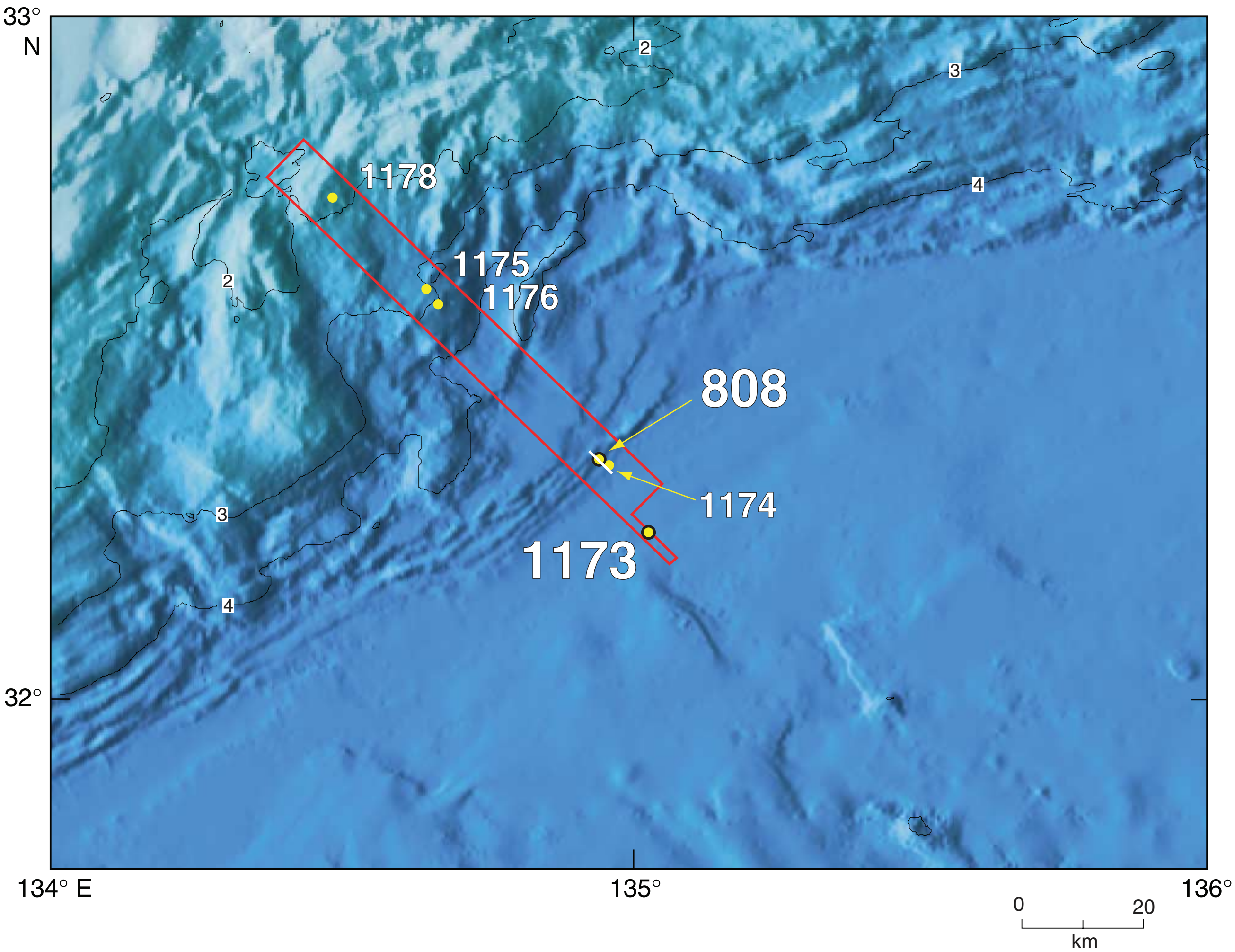

Figure F3. Seismic profile crossing Site 808 (Bangs et al., 1999). Location of seismic profile is shown in Figures F2, p. 34, and F4, p. 36. CDP = common depth point, VE = vertical exaggeration.

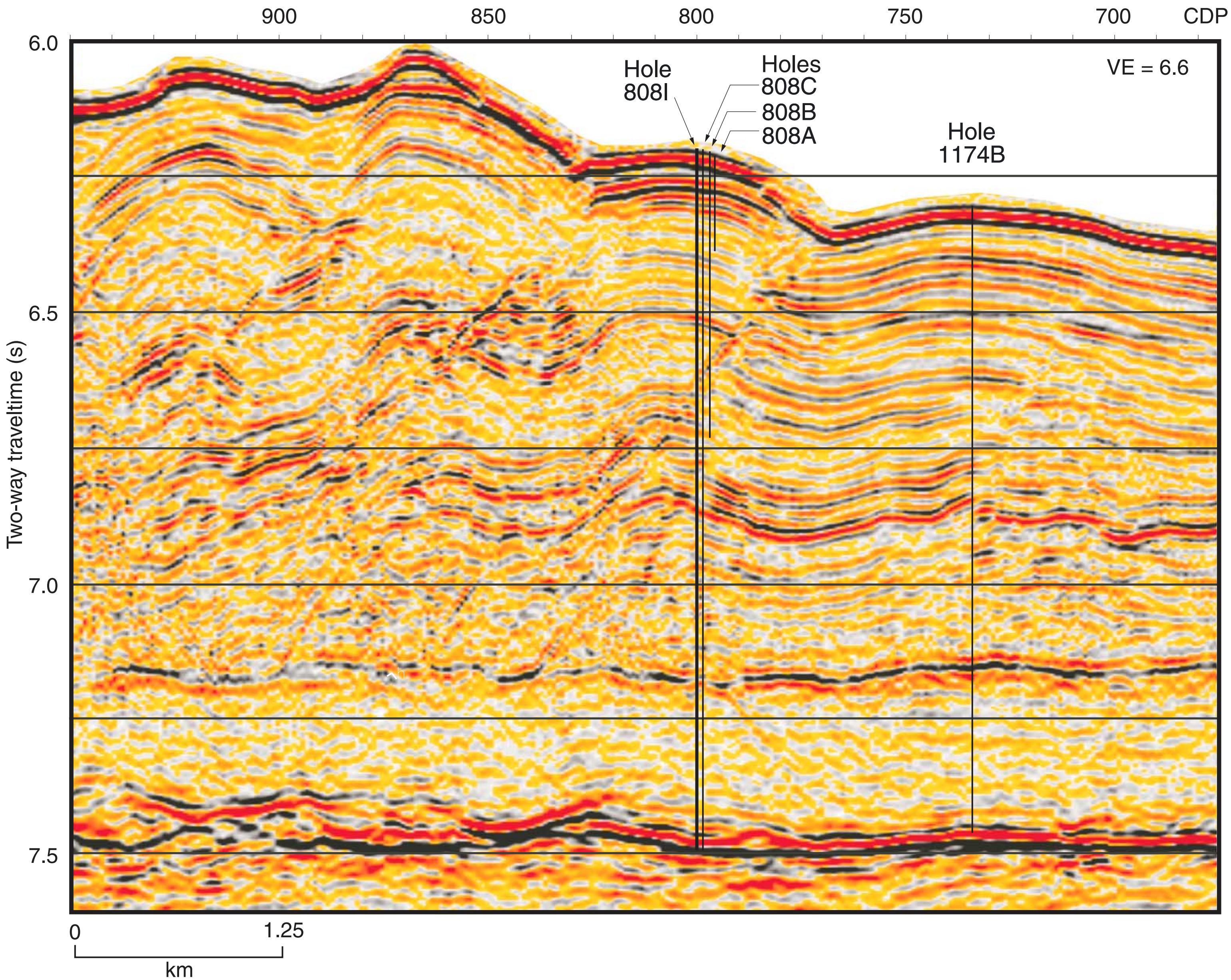

Figure F4. Locations of holes drilled at Site 808 during Legs 196 (red and black) and 131 (blue). Seismic data coverage is shown by solid lines. The bold line shows part of the profile shown in Figure F3, p. 35.

Figure F5. Summary of the quality-control logs, Hole 808I.

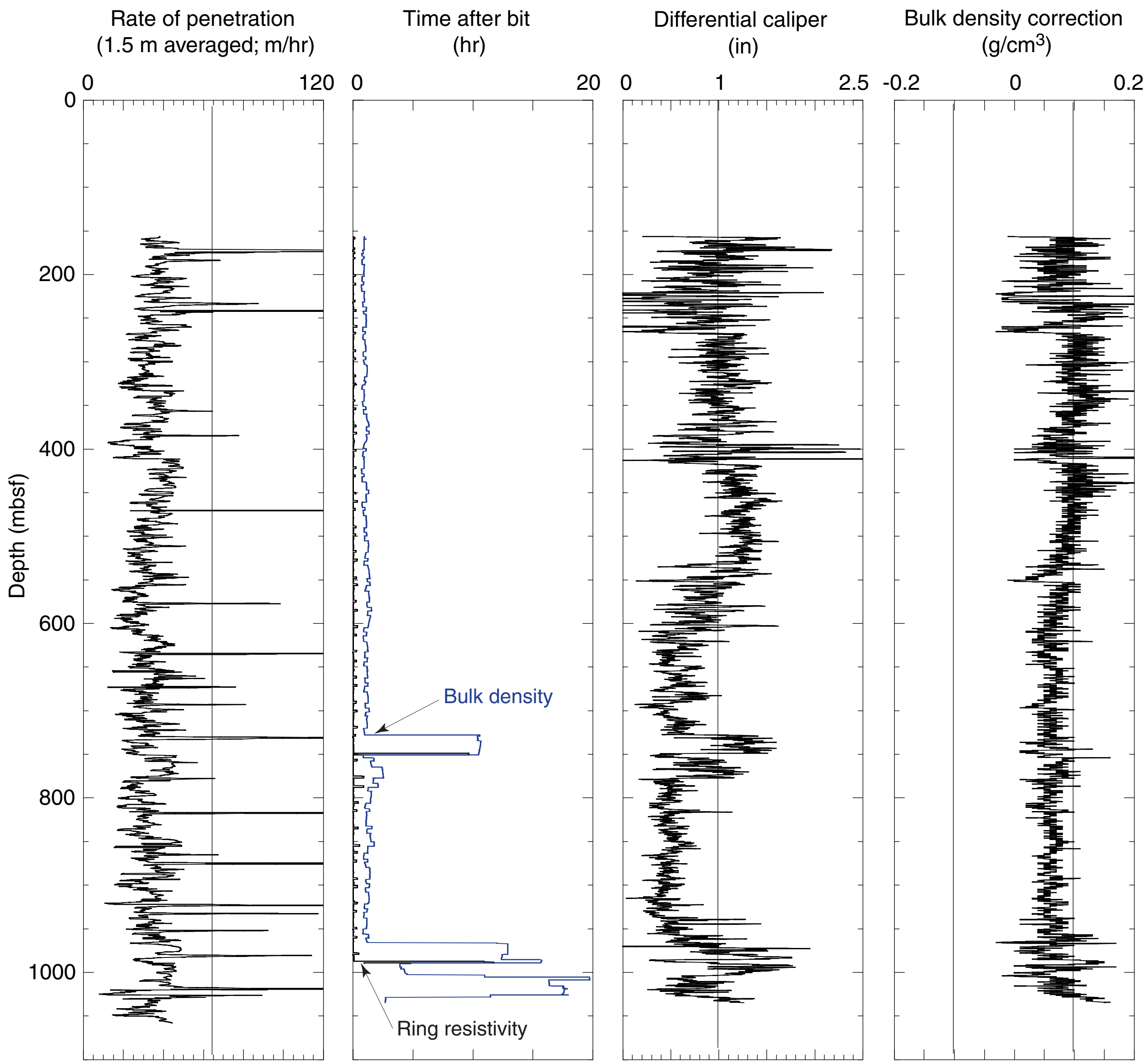

Figure F6. Visual interpretation of log units. Expanded-depth panels show changes in log trends in more detail. (Continued on next page.)

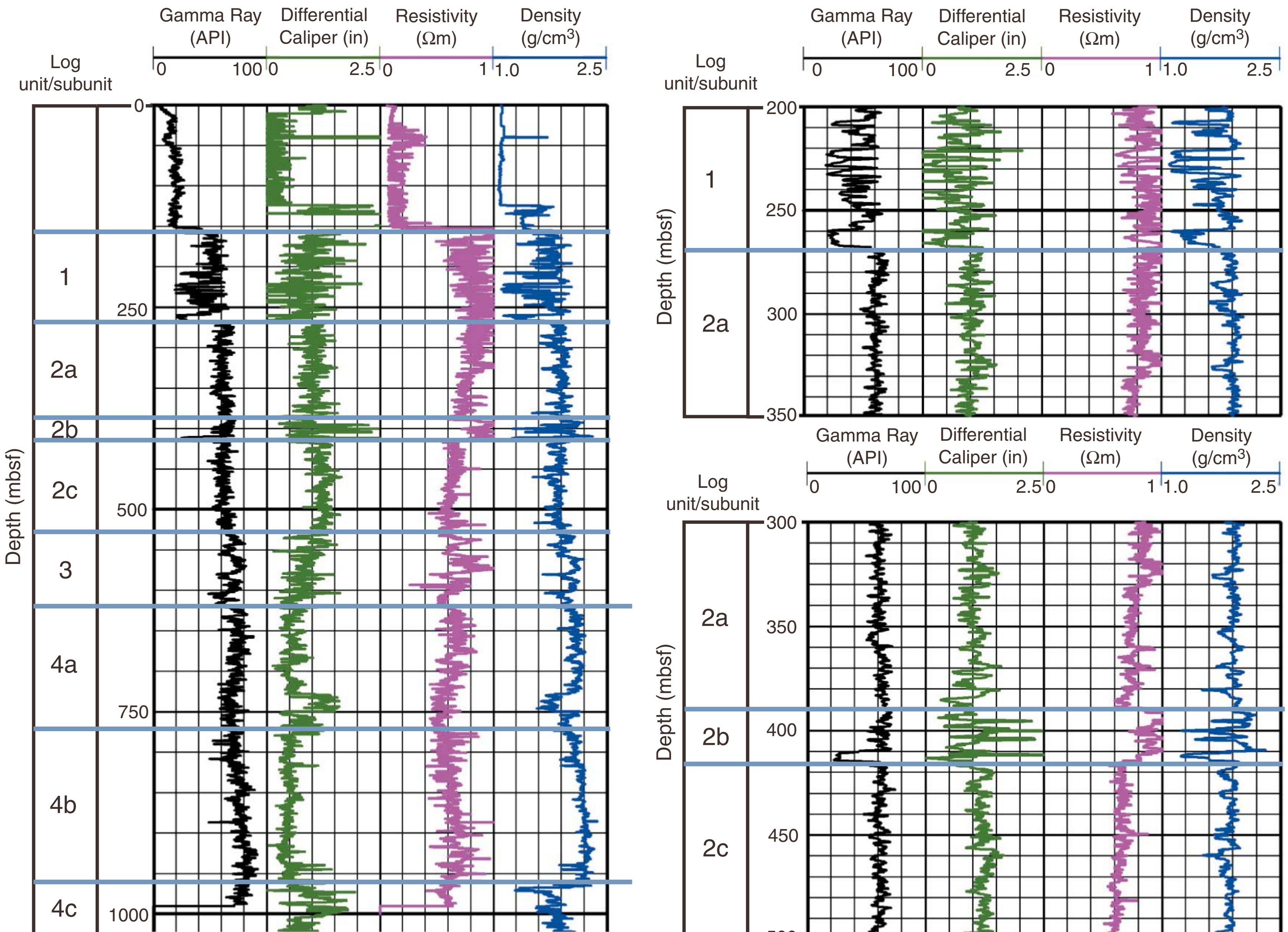

Figure F6 (continued).

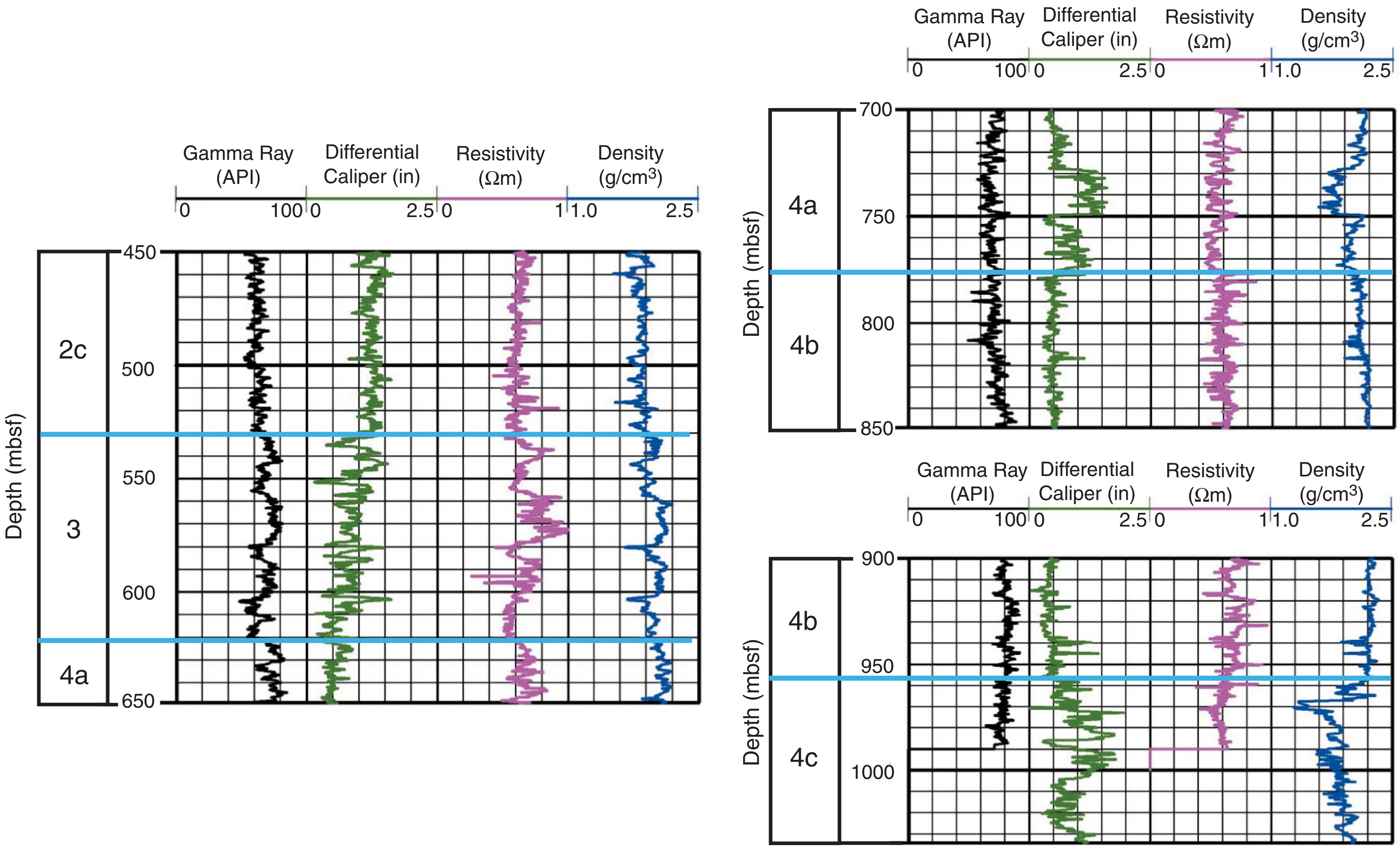

Figure F7. Definition of log units for Site 808 based on statistical analysis. Four clusters were derived, where each cluster describes a group with its specific physical properties. Boundaries between first-order log units correspond to changes in log character related primarily to lithology that are visible on the gamma ray, resistivity, and density logs. Second-order units represent subtle changes in log character.

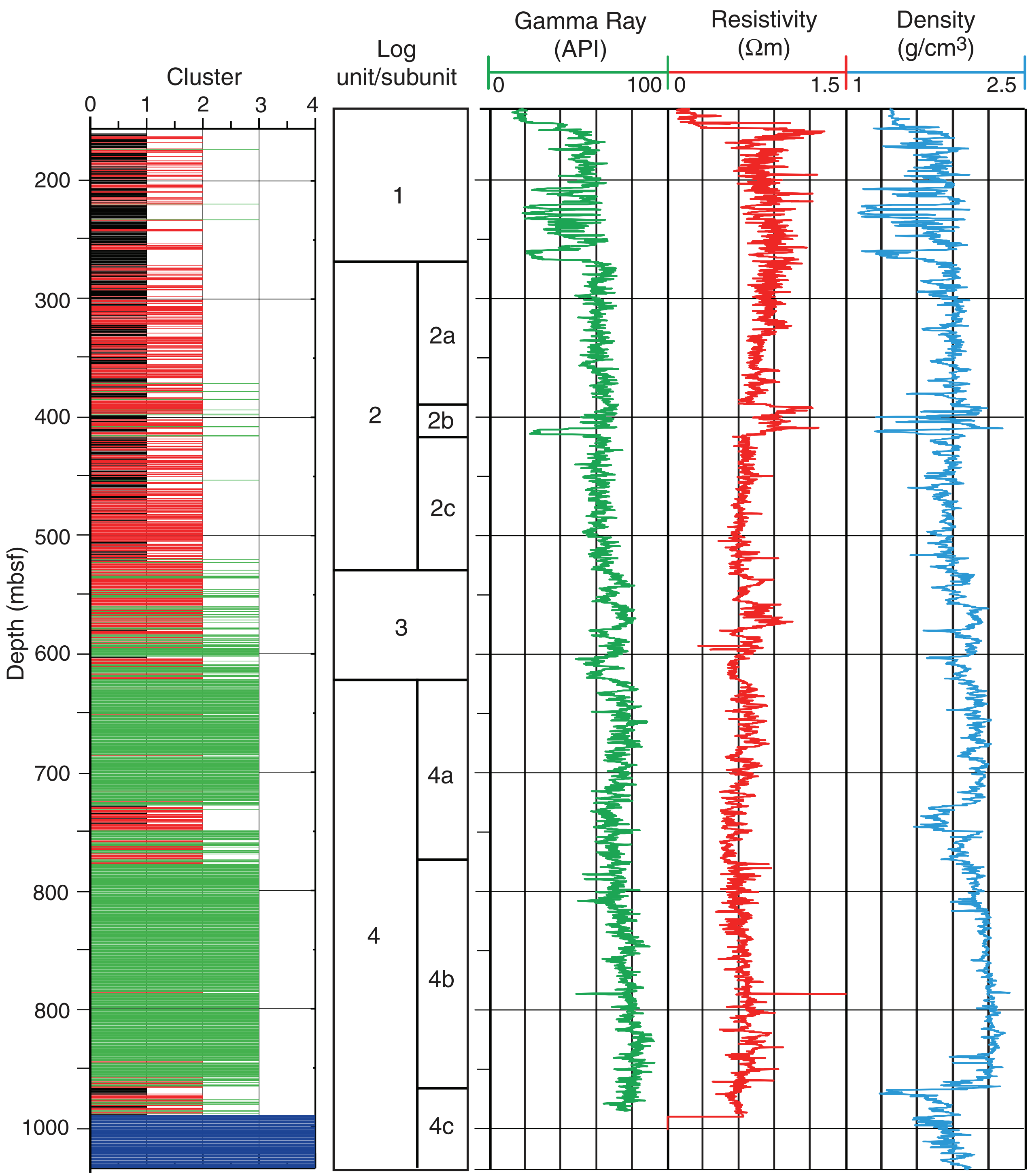

Figure F8. Statistical data for gamma ray, bulk density, resistivity, photoelectric effect, neutron porosity, and differential caliper logs for each log unit, Site 808. The horizontal line within each box shows the median value of each parameter. The box boundaries are equivalent to the 25th and 75th percentiles of values. The error bars mark the 5th and 95th percentiles.

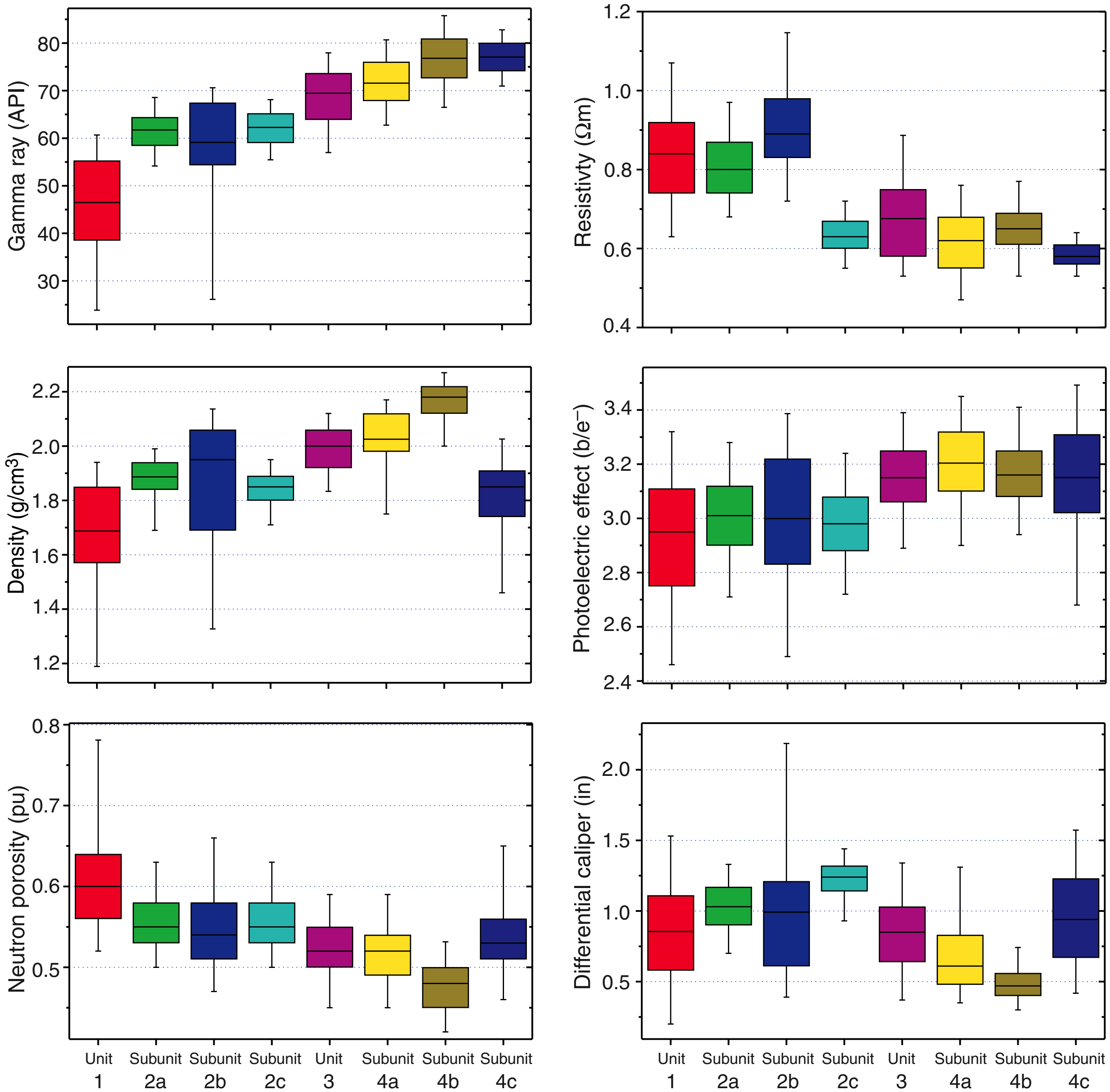

Figure F9. Summary of Site 808 log and lithologic data. The lithology and X-ray diffraction (XRD) mineralogy columns reflect the major lithologic units of Leg 131 Site 808 (Taira, Hill, Firth, et al., 1991). Blue and white marked areas in the log summary portion highlight the log units.

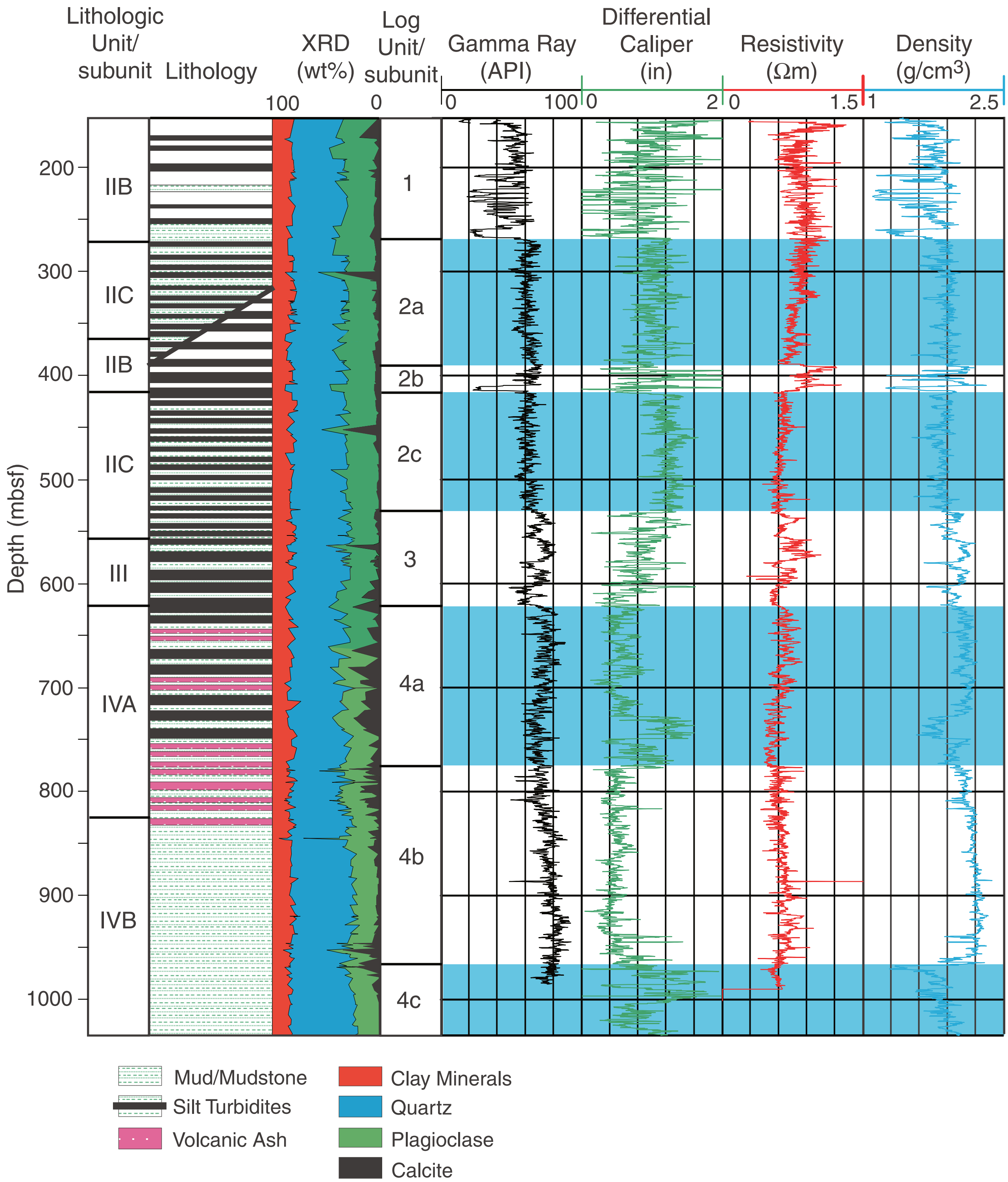

Figure F10. Crossplot of (**A**) gamma ray vs. photoelectric effect and (**B**) resistivity vs. density.

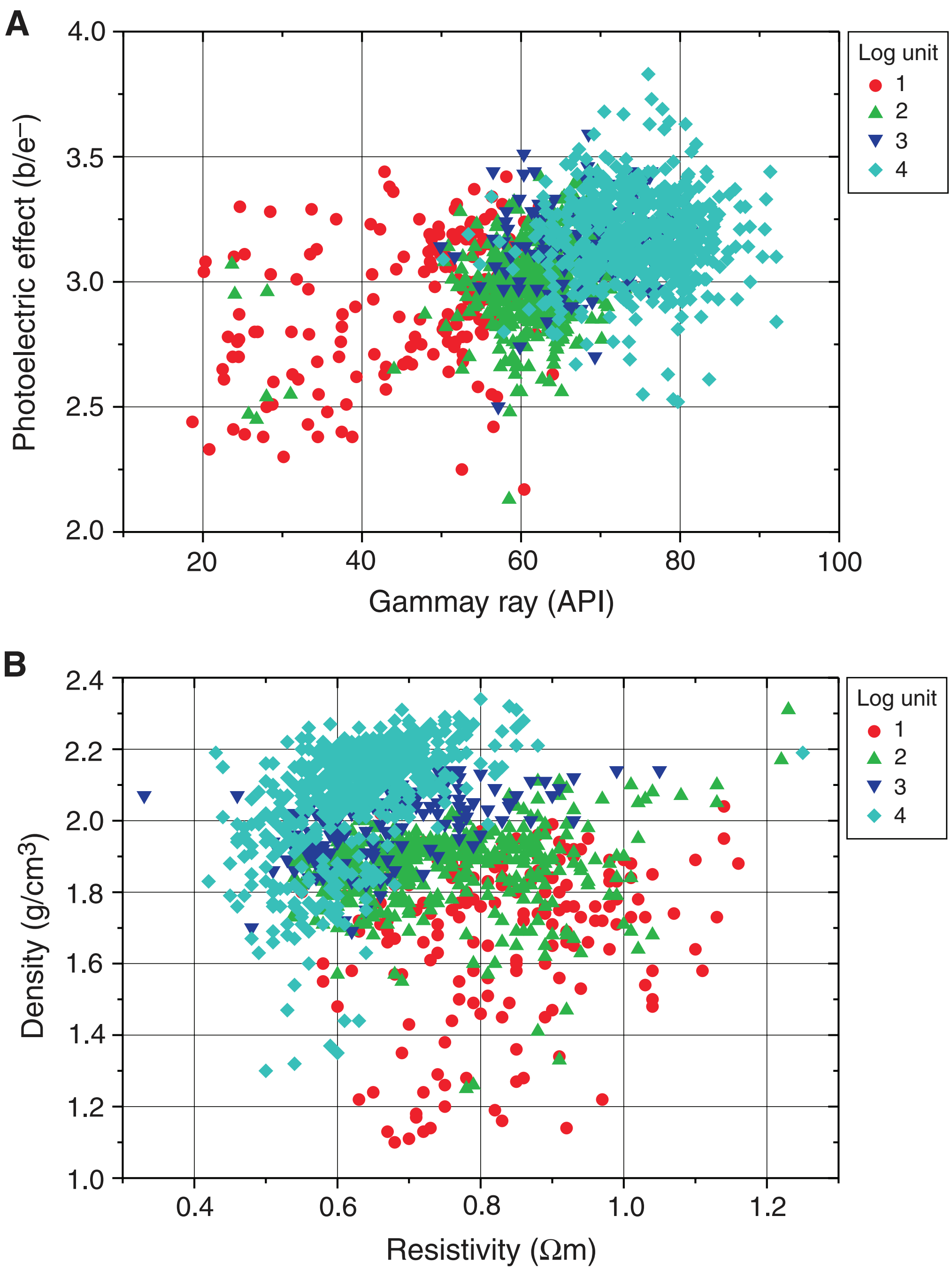

Figure F11. Fracture (**A**) dip and (**B**) strike from resistivity-at-the-bit image interpretation, Leg 196 Hole 808I. Fracture strike is plotted so that the dip direction is 90° counterclockwise from the strike (right-hand rule). **C.** Fault frequency from core analysis, Leg 131 Site 808. Fracture intensity at Hole 808I increases markedly at the frontal thrust zone (389–414 mbsf), fractured interval (559–574 mbsf), and slightly at the décollement zone (~937–965 mbsf). All three zones coincide with increases in fault frequency identified within cores (C), although the frontal thrust zone appears to be slightly shallower in Hole 808C (Leg 131). Fractures are predominantly east-northeast–west-southwest striking, particularly within the frontal thrust zone and fractured interval. Fractures are more randomly orientated at depths >600 mbsf, with a dominant north-south orientation within the décollement zone. Fractures are dominantly south-dipping within the frontal thrust zone and major fractured interval and west-dipping within the décollement zone.

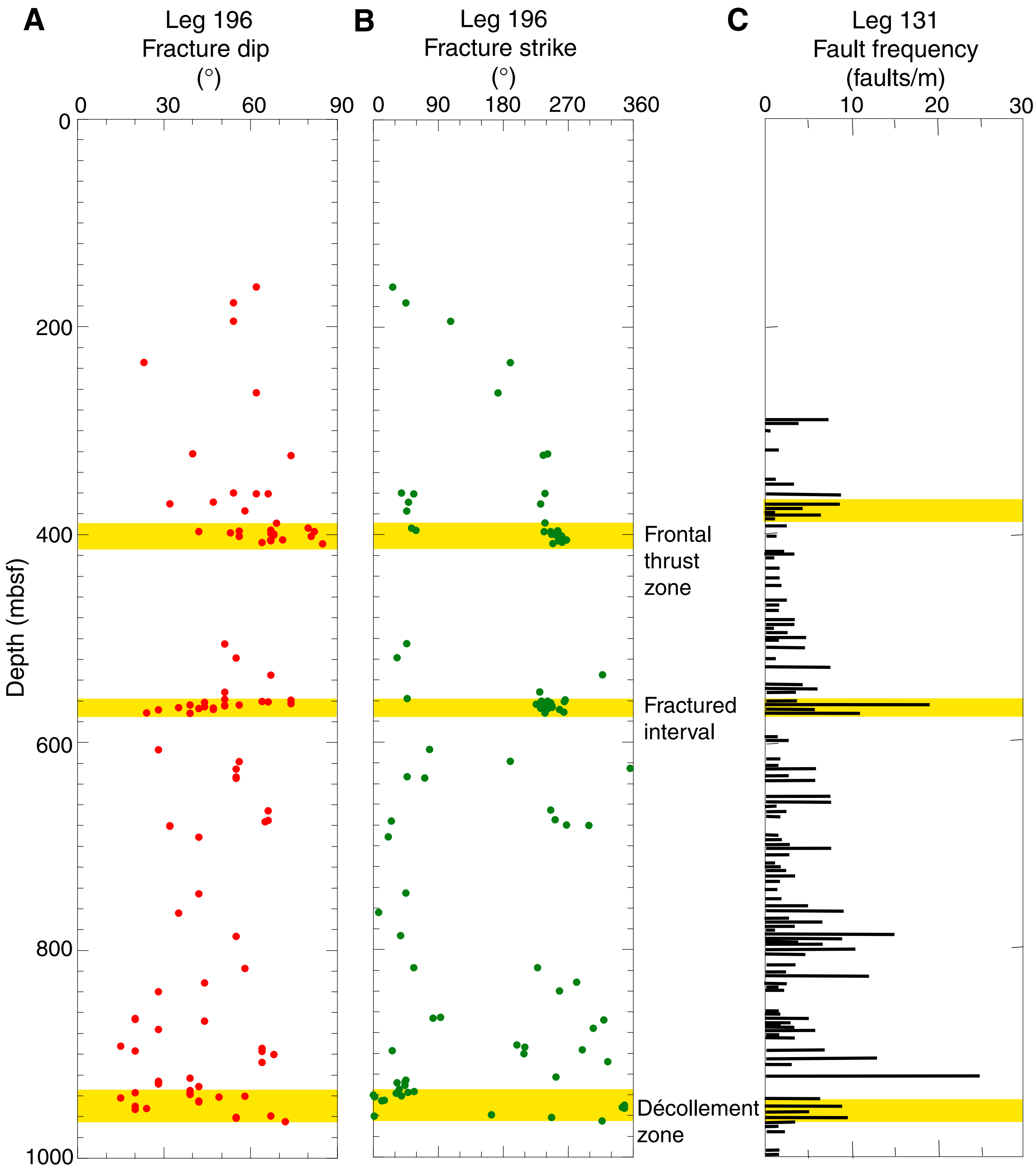

Figure F12. Resistivity-at-the-bit image showing all interpreted fractures. Fractures are separated into conductive (blue) and resistive (red) fractures. Tadpoles show fractures as dip direction with respect to north and dip (0°–90°). Deformation intensifies significantly at the frontal thrust zone (389–414 mbsf), a fractured interval also seen in Leg 131 Site 808 cores (559–574 mbsf), and the décollement zone (~950 mbsf). An interval of continuous strong borehole breakouts at ~270–530 mbsf coincides with log Unit 2 and brackets the frontal thrust zone. Fracture orientations are dominantly northeast-southwest (dip directions northwest-southeast) within the frontal thrust zone and 560-mbsf fractured interval, but are more variably oriented with depth. A north-south fracture orientation (east-west dip direction) is dominant within the décollement zone.

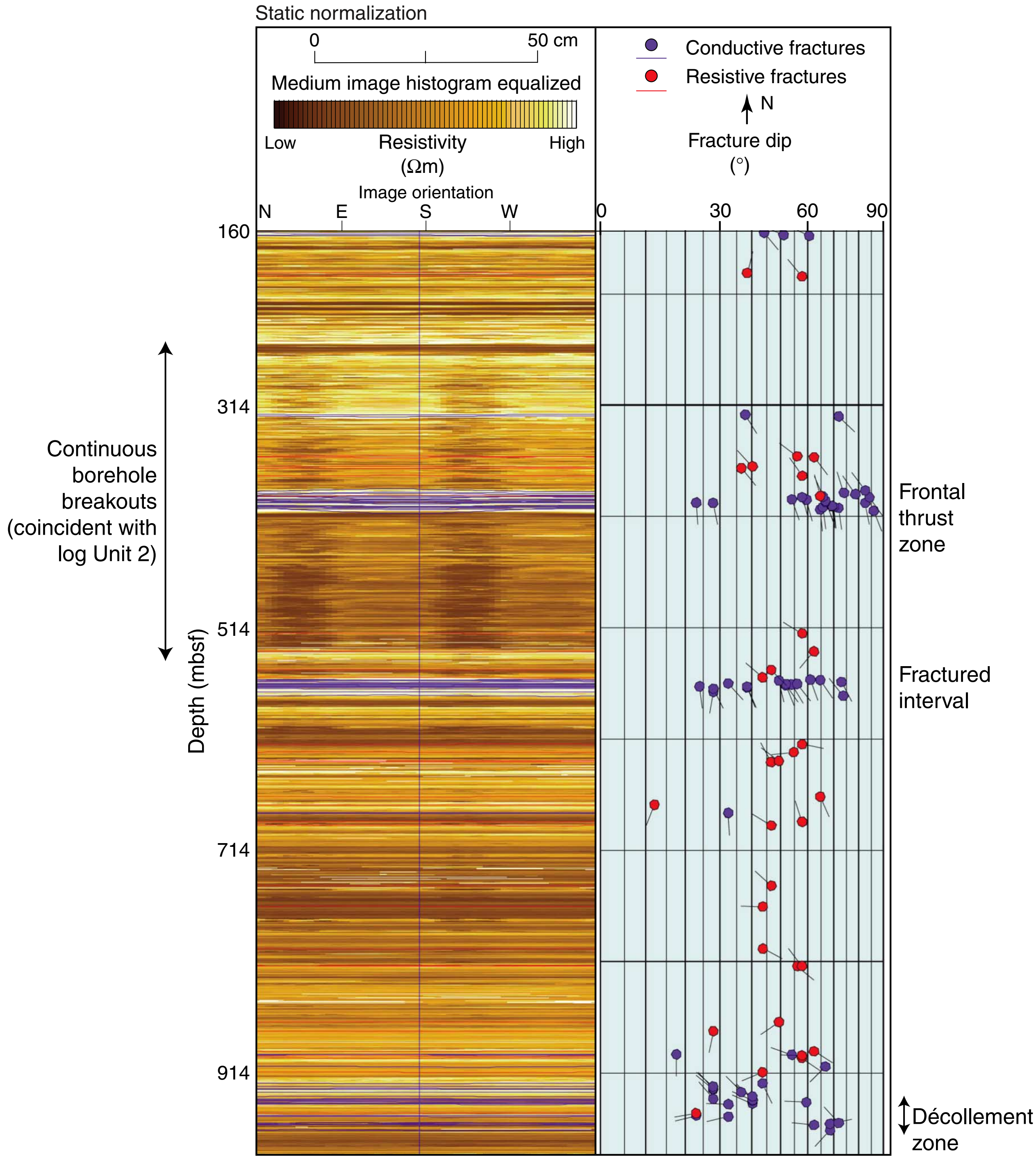

Figure F13. Resistivity-at-the-bit image of the frontal thrust zone at ~389–414 mbsf. The fault zone is characterized by a general increase in resistivity relative to the sections above and below with conductive (open?) high-angle fractures. Bedding is unclear within this image but the possibility remains that features interpreted as fractures could be steeply dipping high-conductivity bedding planes. The orientation of fractures appears to change from the upper to lower part of the fracture zone, from a northeast-southwest to an east-northeast–west-southwest strike. The average fracture strike of east-northeast–west-southwest (dip directions north-northwest and south-southeast) is slightly more easterly than the orientation of minimum horizontal stress determined from borehole breakouts in this part of Hole 808I (Figs. F19, p. 52, F20, p. 53). The position of the three-dimensional (3-D) borehole view of Figure F16, p. 49, is indicated.

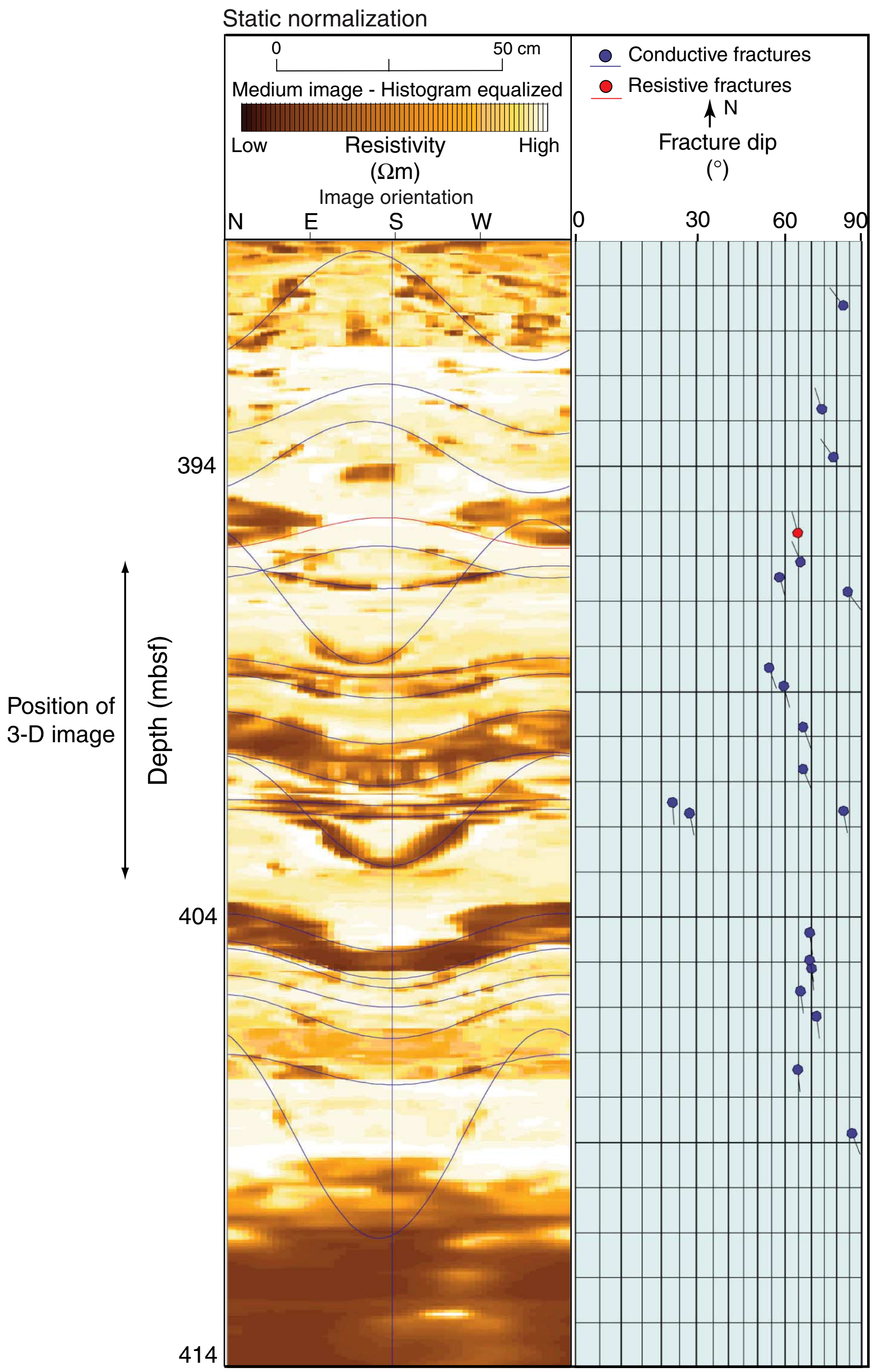

Figure F14. A. Stereographic plot of poles to fracture planes (equal-area lower-hemisphere projection). **B.** Rose diagram of azimuths of poles to fracture planes, with bounding circle representing 12% of data points. Black square represents the direction of plate convergence at the Nankai Trough (average of 313°; Seno et al., 1993). Fractures indicate a dominant northeast-southwest trend (with poles at 90° to this trend) with a slight difference between the average trend of poles and the convergence vector.

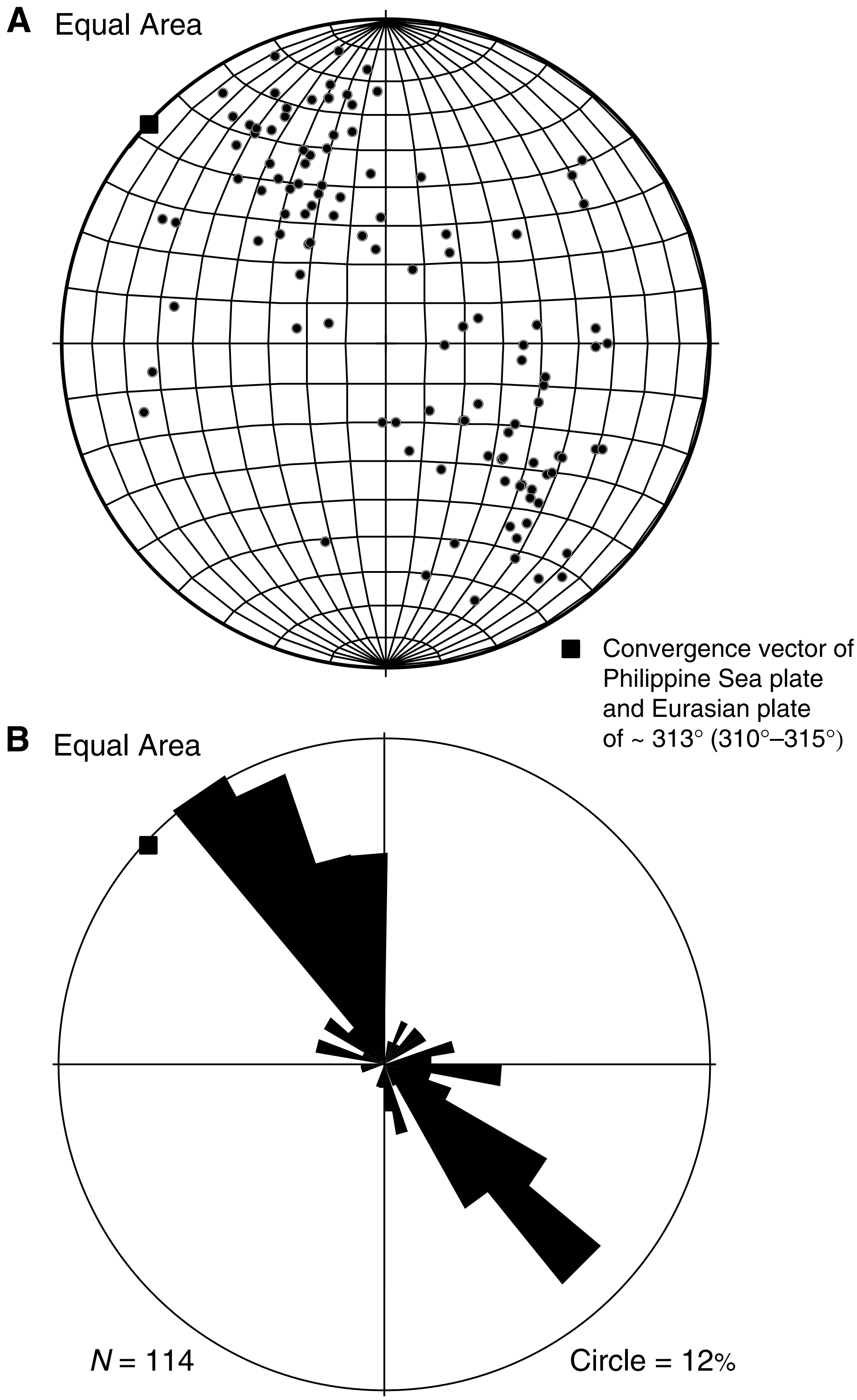

Figure F15. Bedding (**A**) dip and (**B**) strike from resistivity-at-the-bit image interpretation. Bedding strike is plotted so that the dip direction is 90° counterclockwise from the strike (right-hand rule). Bedding dips are predominantly shallow with a range of 0°–50°. Bedding interpretations are often absent from highly deformed zones (e.g., the frontal thrust zone) due to masking by a generally high resistivity signature within these zones (see Fig. F13, p. 46). Bedding orientations appear to be random at depths shallower than the fractured interval at ~560 mbsf, but show a dominant northeast-southwest trend below this interval. There is a prominent north-south orientation with west-dipping beds around the décollement zone (~900–960 mbsf).

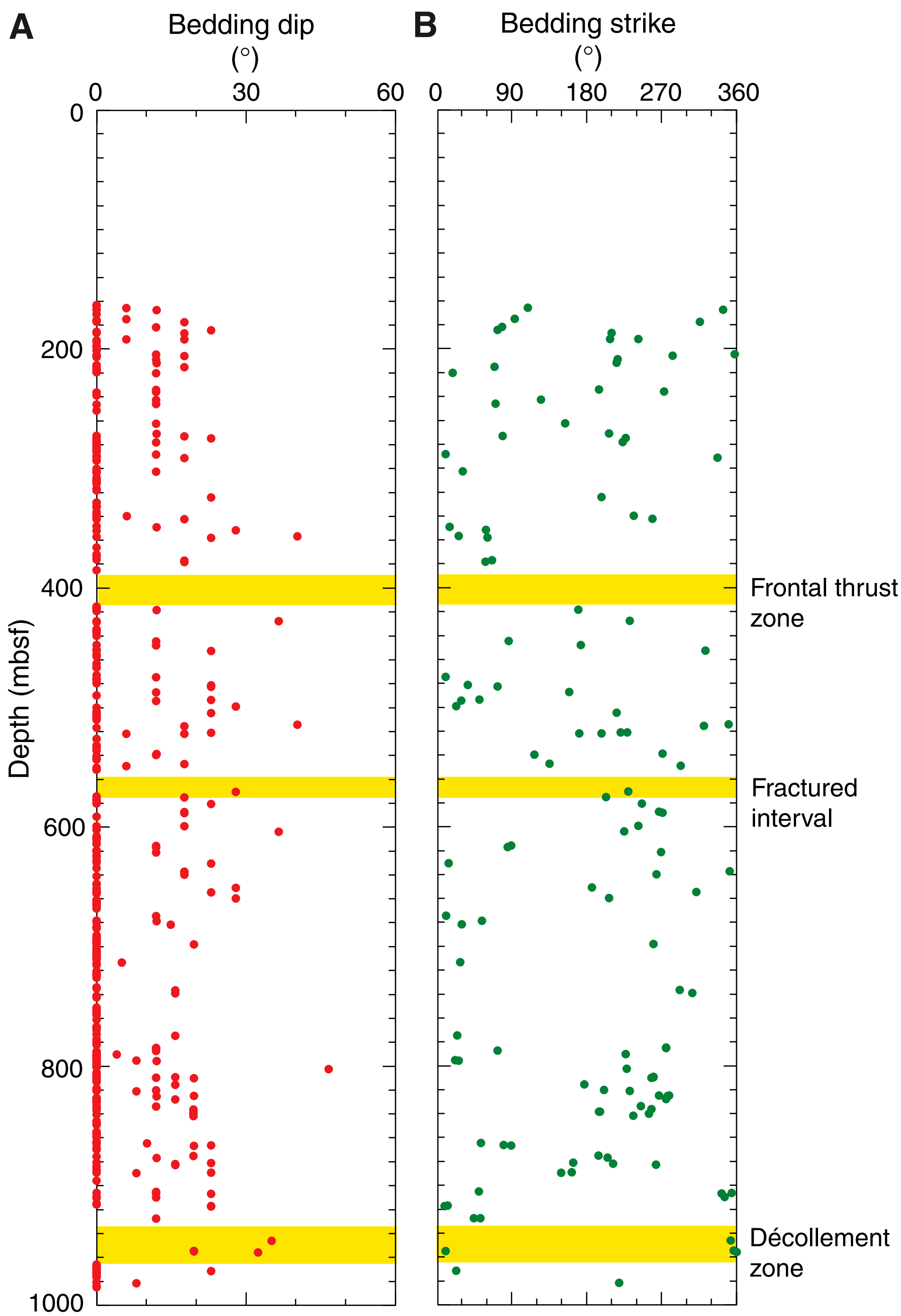

Figure F16. Three-dimensional (3-D) view of the resistivity-at-the-bit image of part of the frontal thrust zone shown in its cylindrical borehole form. The view is slightly elevated (25°) and from the south-southwest (200°). The image shows steeply south-dipping conductive fractures (picked out by blue circles) within a highly resistive deformation zone. Position of the 3-D image is shown in Figure F13, p. 46.

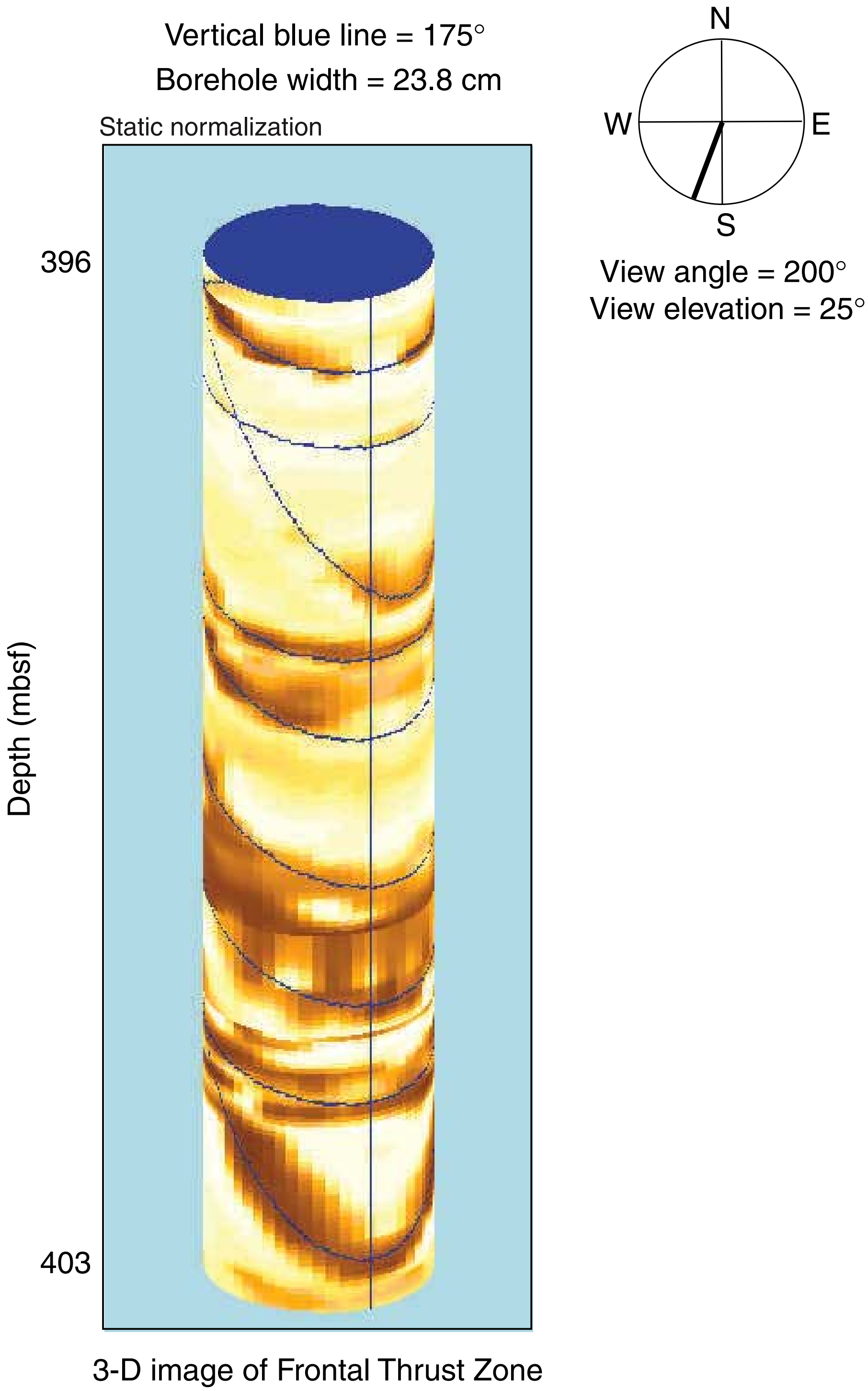

Figure F17. Physical properties of the décollement zone and surrounding sections, Hole 808I. Logs of resistivity, bulk density, and density-derived porosity are shown with depth. The décollement zone (from interpretation of deformation in resistivity-at-the-bit images) is indicated by orange dashed lines. Discrete fractured intervals within this zone occur at 897–904, 937–942, and 959–965 mbsf, corresponding to overall lower resistivity (characterized by conductive fractures) and lower density (as might be expected from open fractures). Blue solid lines show the décollement zone as identified in Leg 131 Site 808 cores.

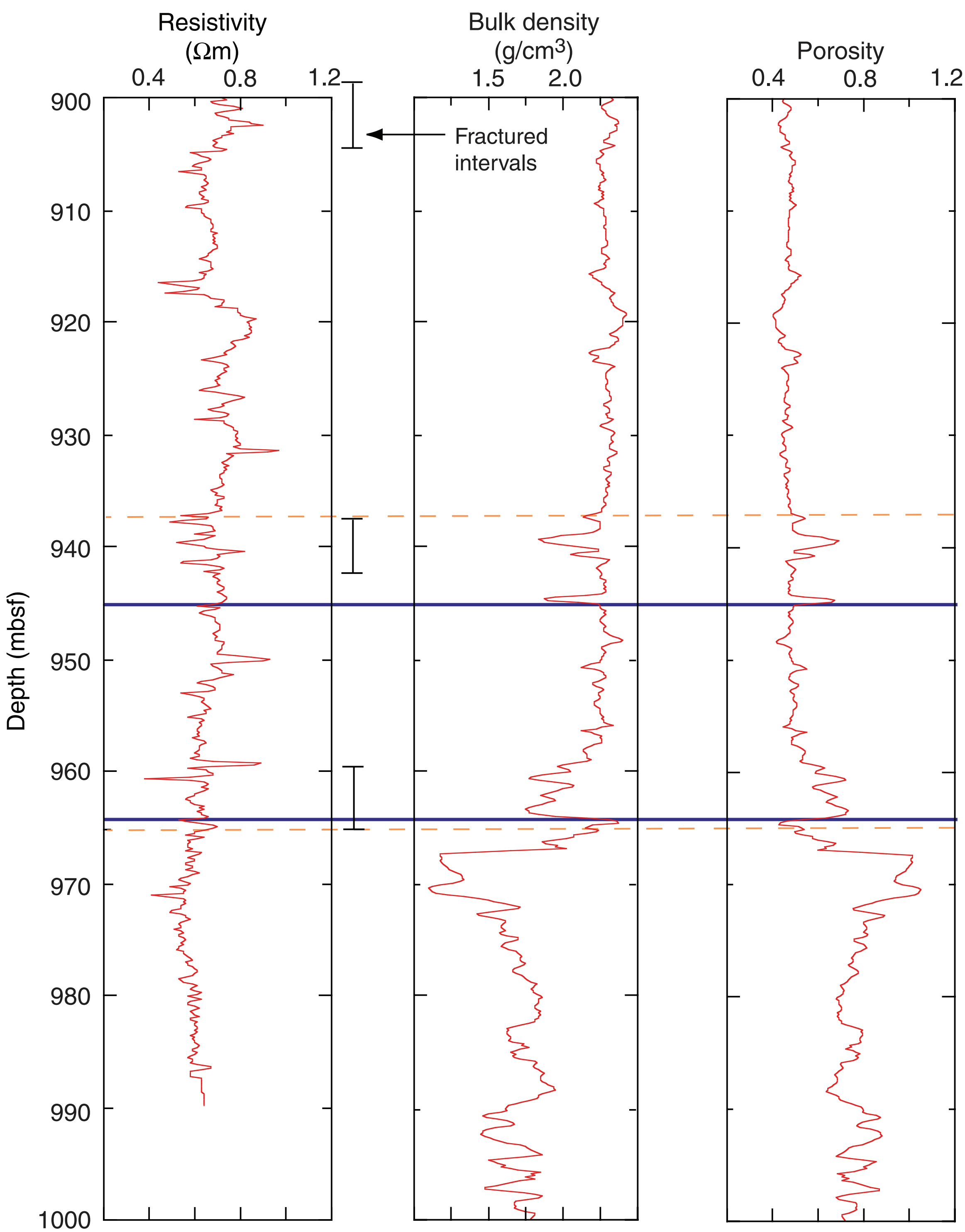

Figure F18. Resistivity-at-the-bit image of the base of the décollement zone. Minimal deformation is observed in the form of several discrete fractured intervals, containing high-angle conductive fractures (dark sinusoidal features at 959 and 965 mbsf).

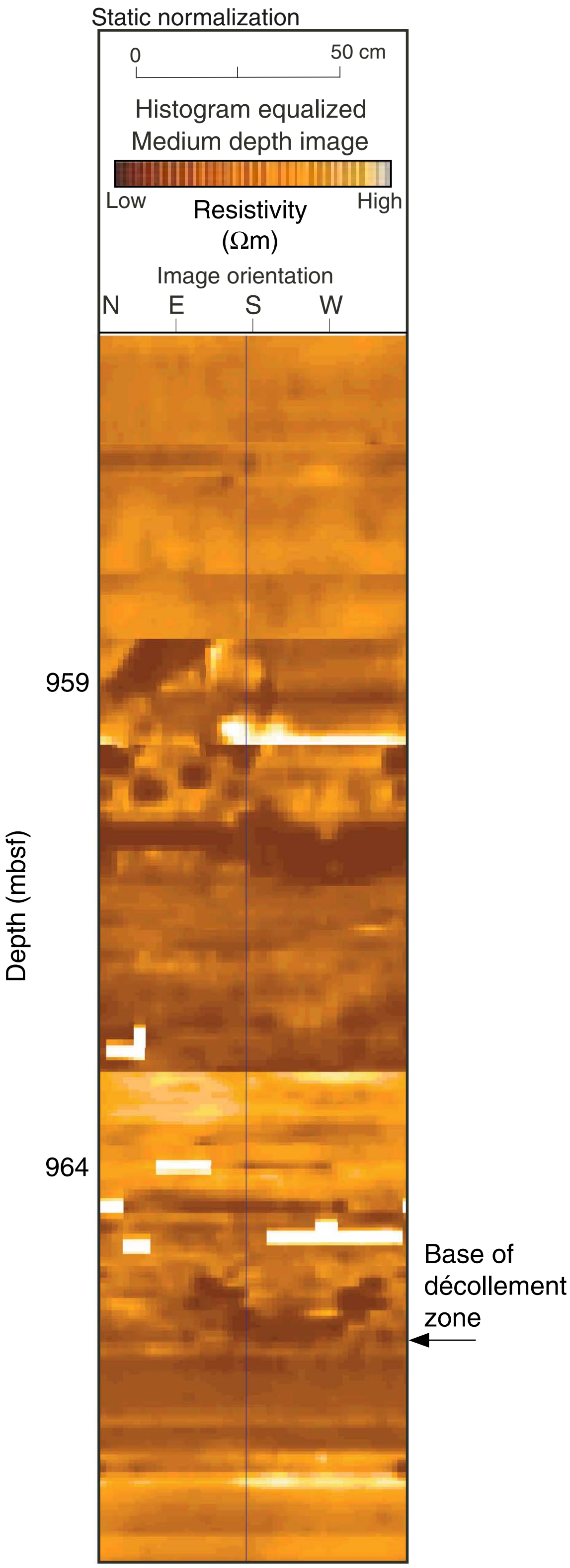

Figure F19. Resistivity-at-the-bit images of borehole breakouts (dark low-resistivity parallel lines) at 1-in (shallow), 3-in (medium,) and 5-in (deep) penetration from the borehole, 280–325 mbsf. Breakouts occur ~100 m above the frontal thrust zone within log Unit 2. The high-conductivity breakouts indicate elongation of the borehole in the direction of minimum horizontal compressive stress (σ_2 in this case). The two breakout lines occur opposite each other (~180° apart) in the borehole. The orientation of breakouts (northeast-southwest, or ~220°–230°) is in good agreement with the plate convergence vector of ~310°–315° that would be expected to be in alignment with the maximum compressive stress, σ_1. Notice that the resistivity of the breakouts increases from the shallow to deep image, suggesting minimal invasion and deformation 5 in away from the borehole.

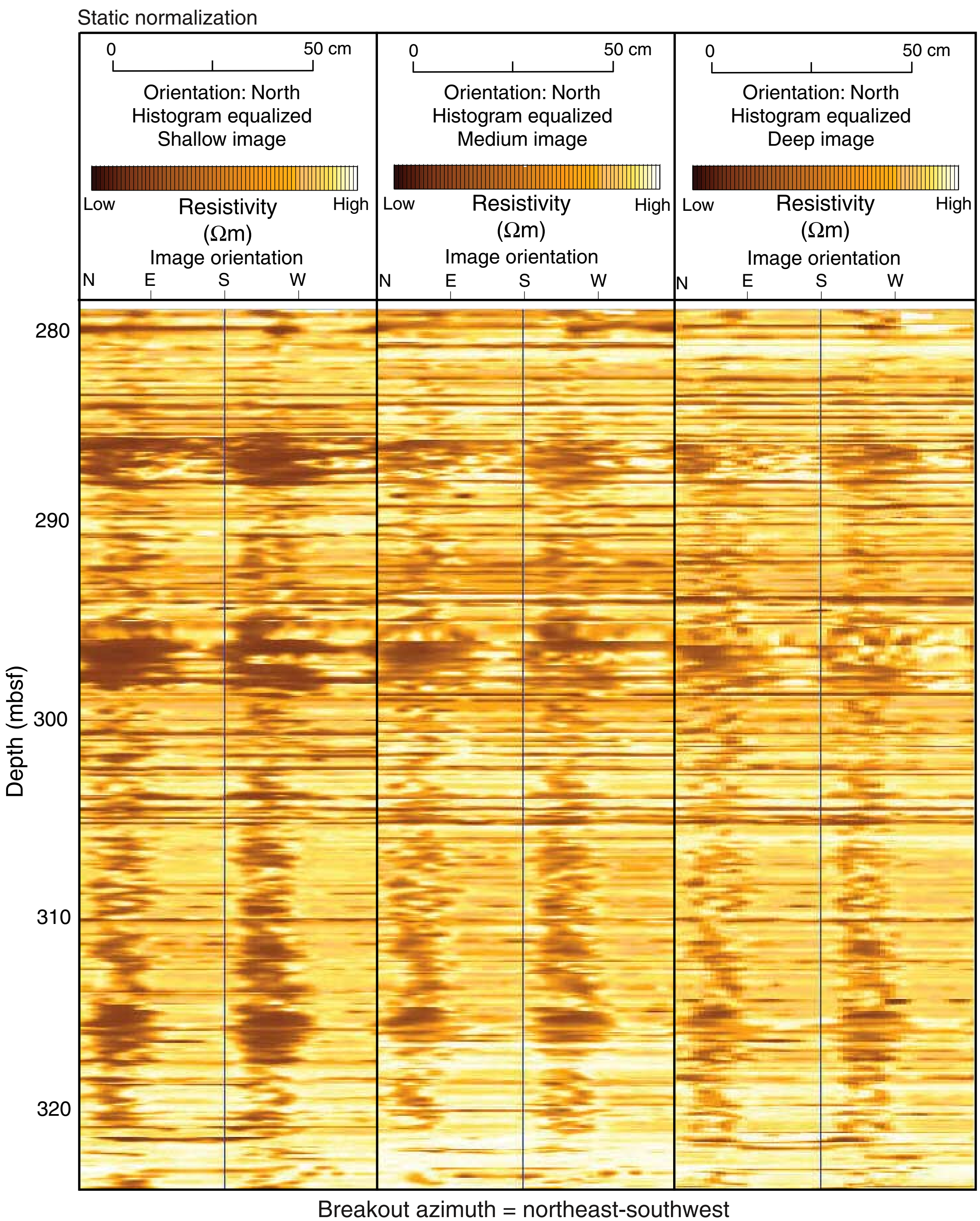

Figure F20. Resistivity-at-the-bit images of borehole breakouts at 1-in (shallow), 3-in (medium,) and 5-in (deep) penetration from the borehole, 460–505 mbsf. Breakouts occur ~100 m below the frontal thrust zone close to the base of log Unit 2. See Figure F19, p. 52, for details. Notice that the resistivity of breakouts shows little variation from the shallow to deep image, suggesting a similar degree of deformation and invasion at 1, 3, and 5 in from the borehole. This is in contrast to Figure F19, p. 52, where variability is seen between the three images. If possible variations in drilling parameters are excluded, this difference may be related to lithologic contrasts (note that sediments in the interval imaged by Figure F19, p. 52, have higher resistivity than the sediments imaged here).

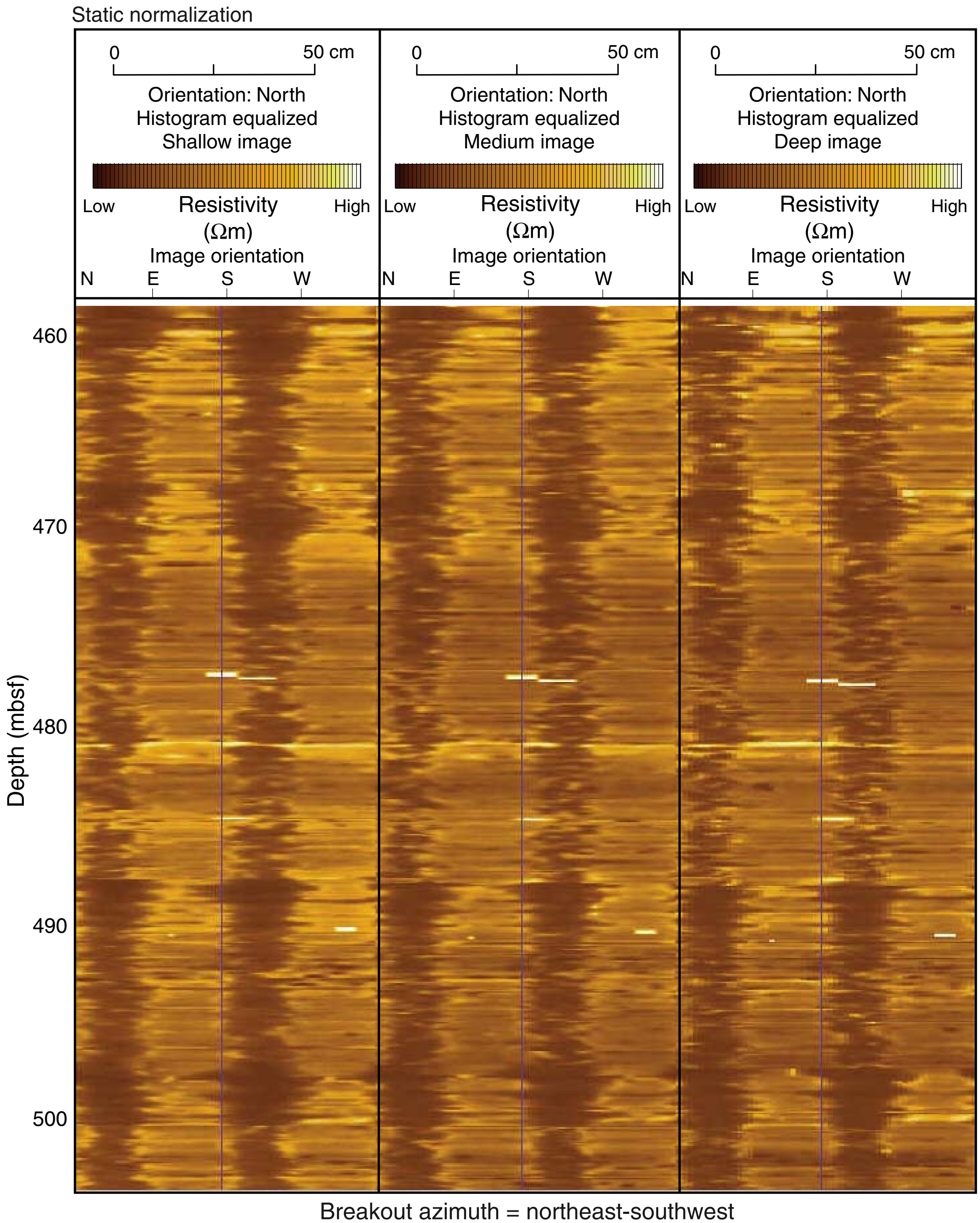

Figure F21. Logging-while-drilling (LWD) density (RHOB) profile from Hole 808I compared to bulk density values from Site 808 cores.

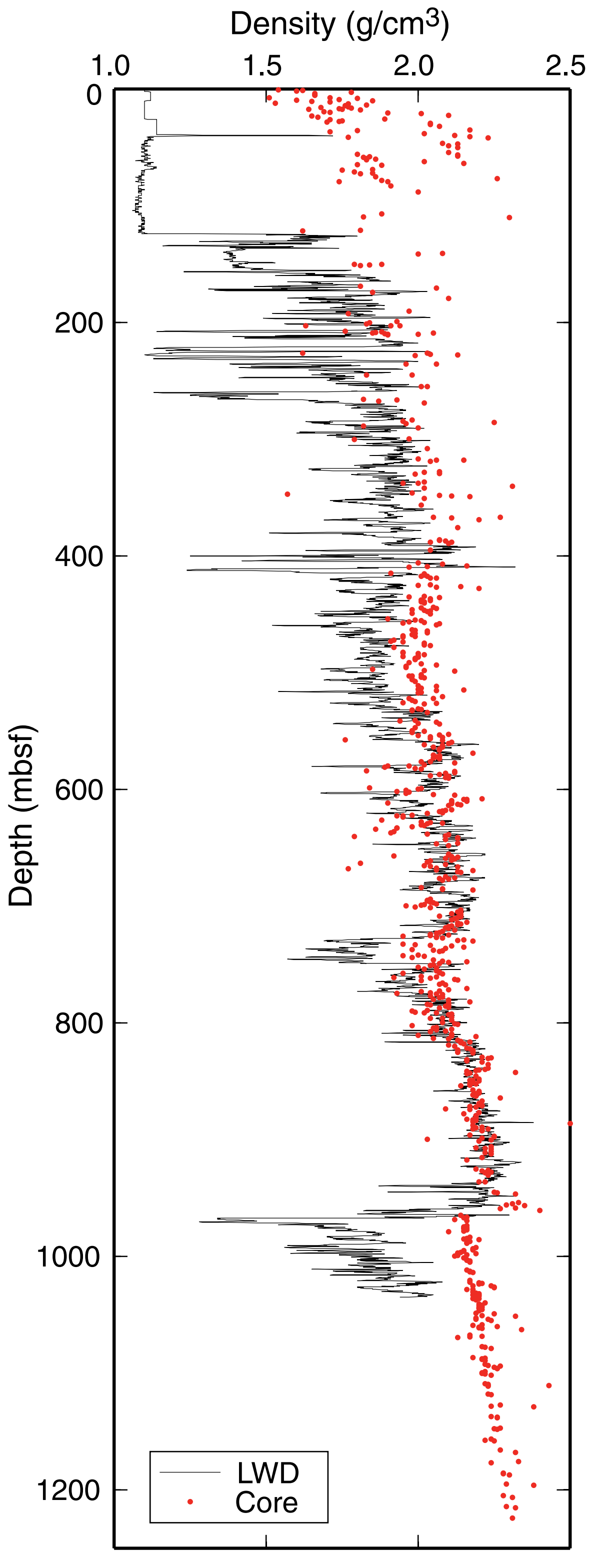

Figure F22. Least-squares regression fits of grain density values from Site 808 cores. The upper to lower Shikoku Basin facies boundary is at 823.7 mbsf.

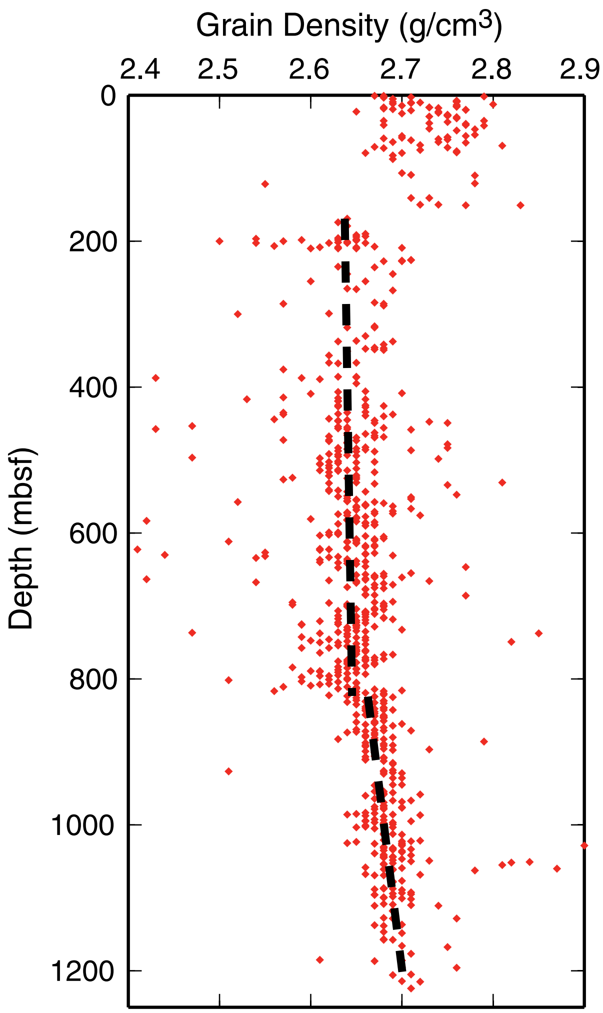

Figure F23. Porosity profile calculated from the Hole 808I logging-while-drilling (LWD) density (RHOB) log using the least-squares regression fit of grain density values from Site 808 (Fig. F22, p. 55), compared to porosity measurements from Site 808 cores.

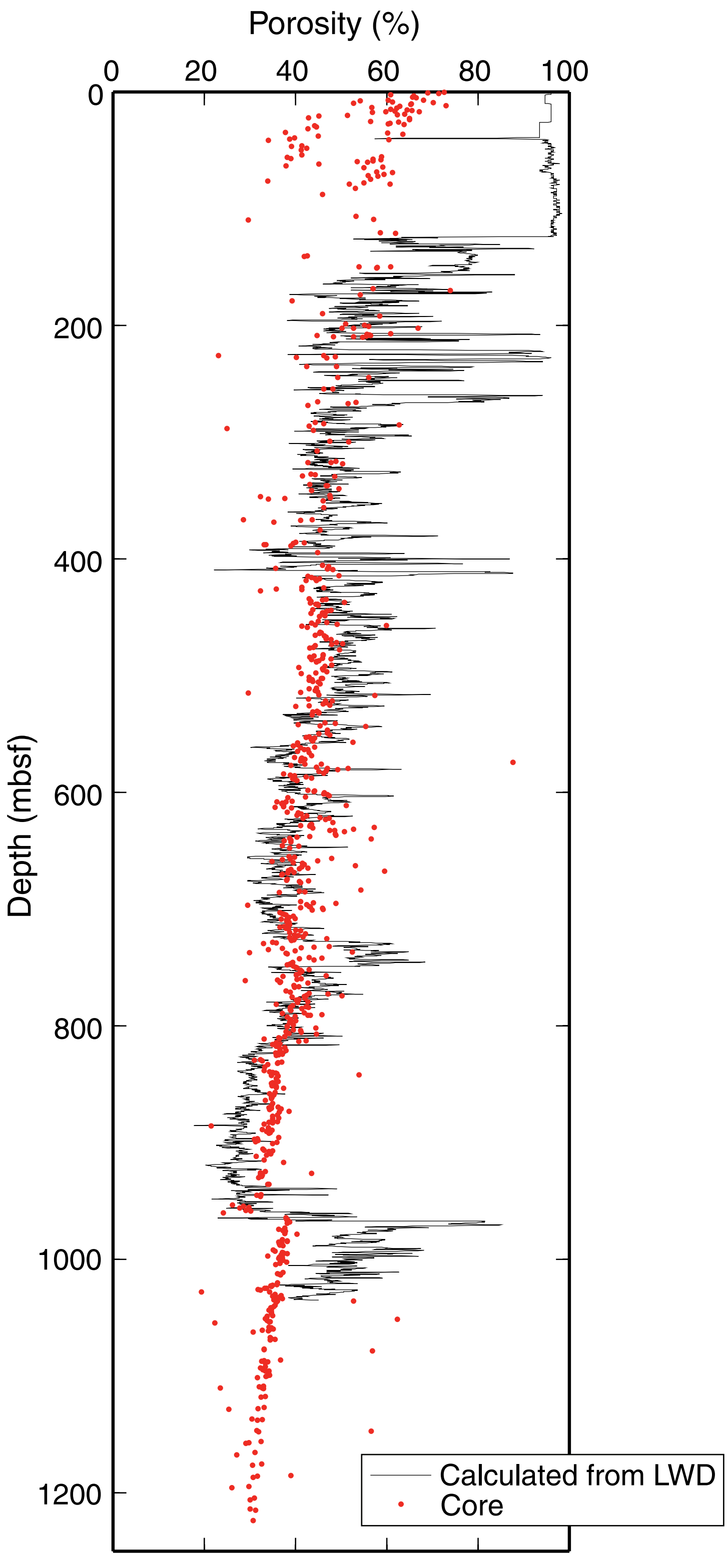

Figure F24. Comparison of logging-while-drilling (LWD) and core density logs, Sites 808 and 1173. Lithologic units are shown for each site.

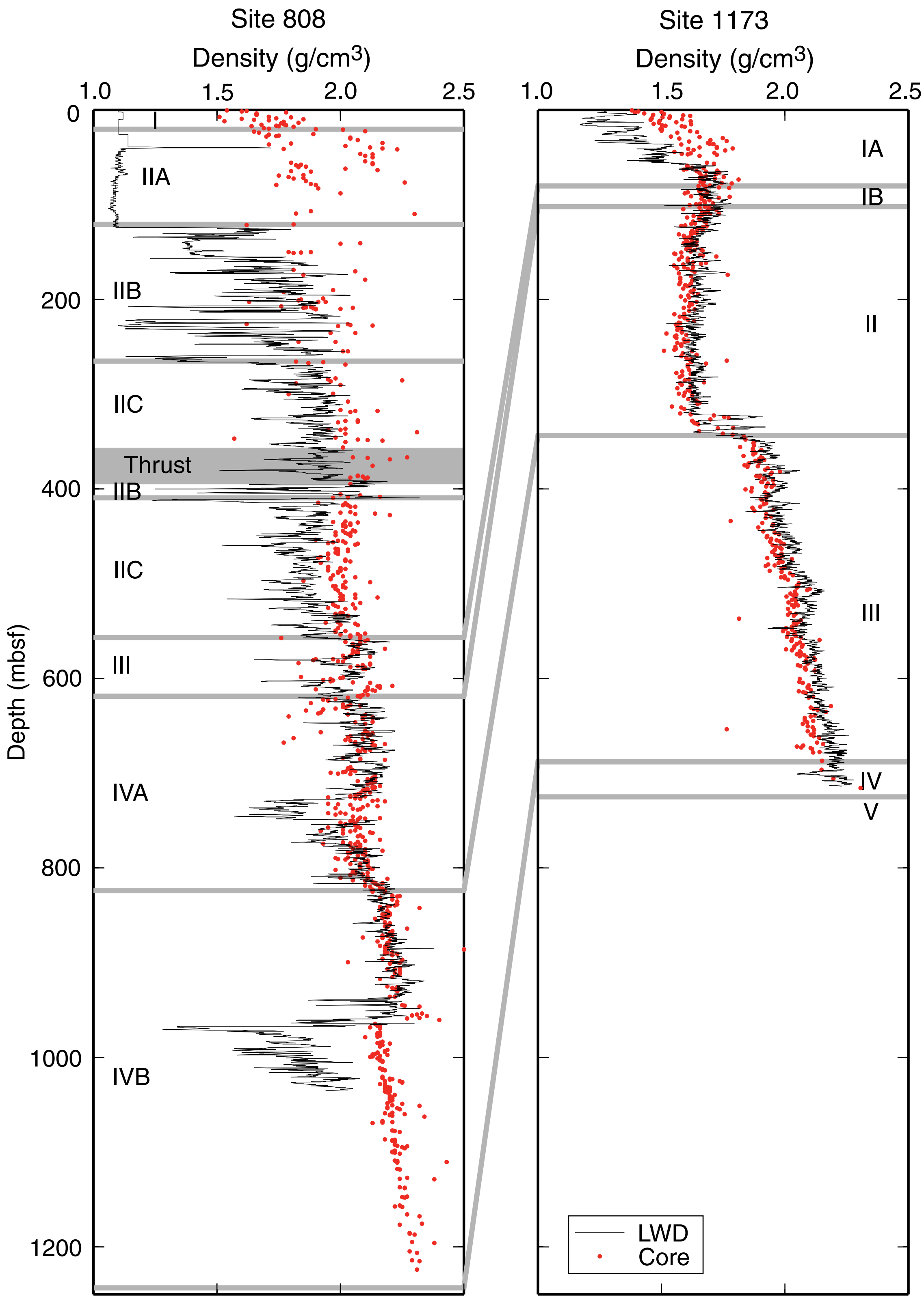

Figure F25. Comparison of logging-while-drilling (LWD) and core porosity logs, Sites 808 and 1173. The LWD porosity profile was calculated from the Hole 808I LWD density profile using the least-squares regression fit of grain density values from Site 808 (see Fig. **F22**, p. 55). Lithologic units are shown for each site.

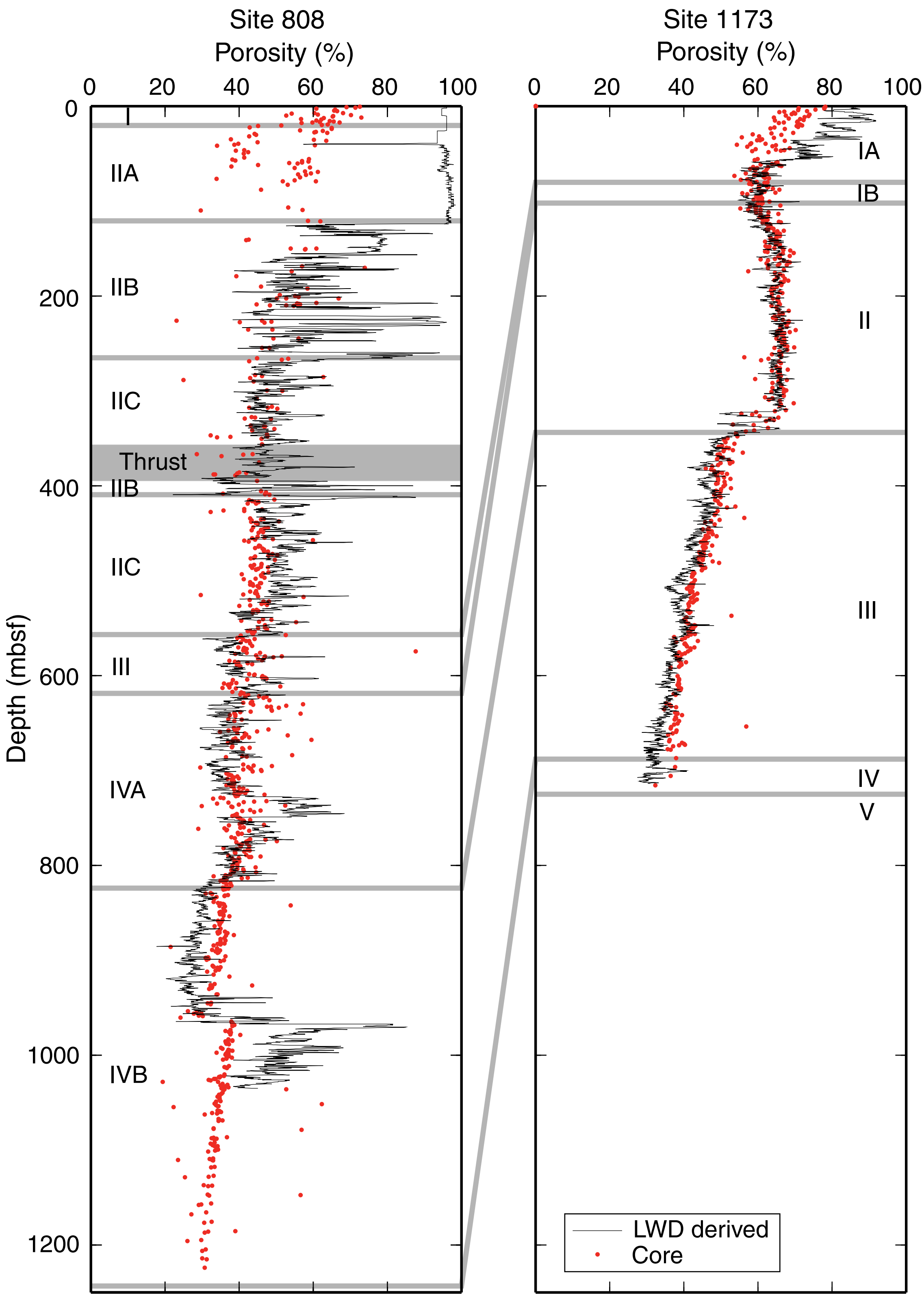

Figure F26. Five resistivity logs acquired with the resistivity-at-the-bit tool. Lines separate log Units 1–4.

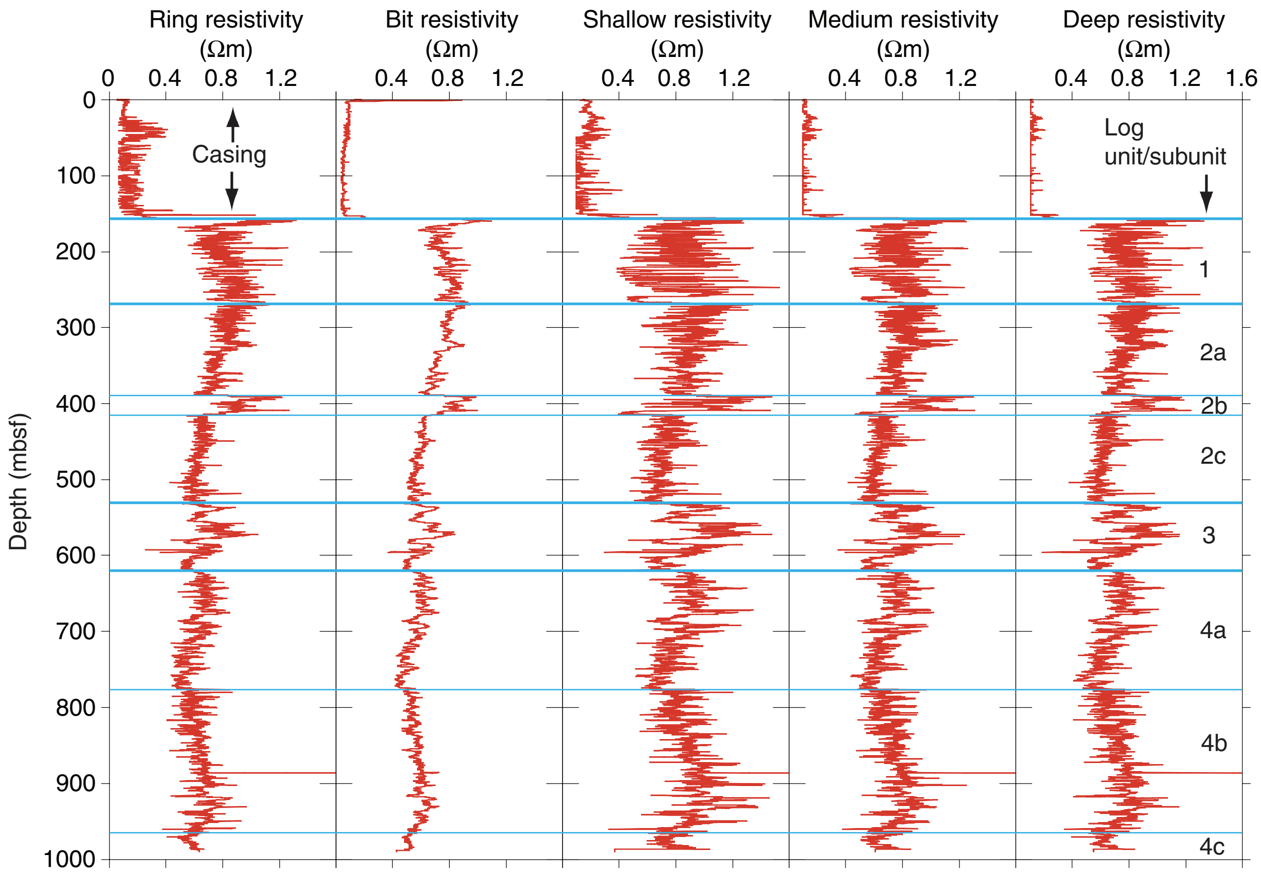

Figure F27. A. Ring and bit resistivity acquired with the resistivity-at-the-bit (RAB) tool. **B.** Shallow-, medium-, and deep-focused resistivity acquired with the RAB tool. Lines separate log Units 1–4.

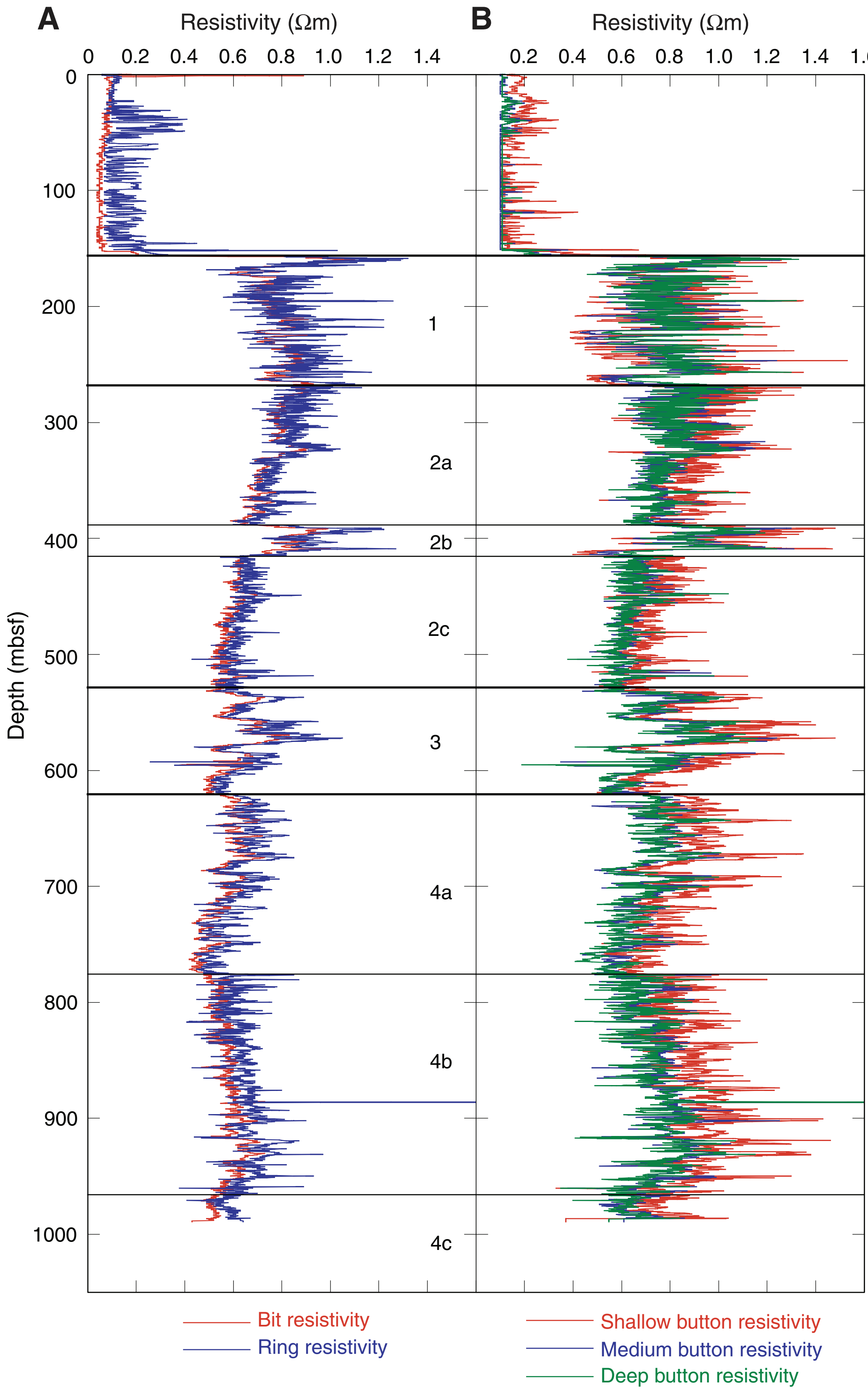

Figure F28. Correlation diagrams of (**A**) bit vs. ring resistivity and (**B**) shallow vs. deep resistivity. On each plot, the black line is the line of unit slope passing through the origin and the red line is the linear fit to the data. Equations describe the least-squares regression curves and *R* is the correlation coefficient.

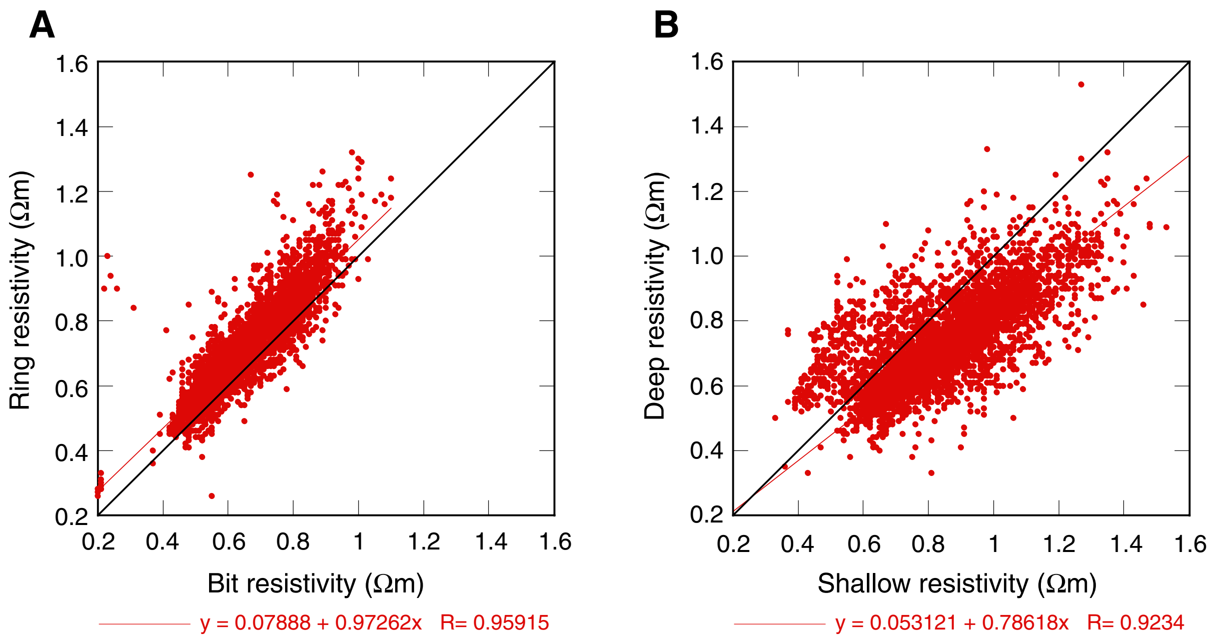

Figure F29. Preliminary IDEAL sonic-while-drilling *P*-wave velocity picks compared with core velocity data (solid circles), Leg 131 Hole 808B (blue curve) and Hole 808E (black curve) wireline logs, and Hole 808E vertical seismic profile values (black bars; rectangles = formal error of line fit [Moore, 1993]). Heavy line near depth axis shows extent of casing.

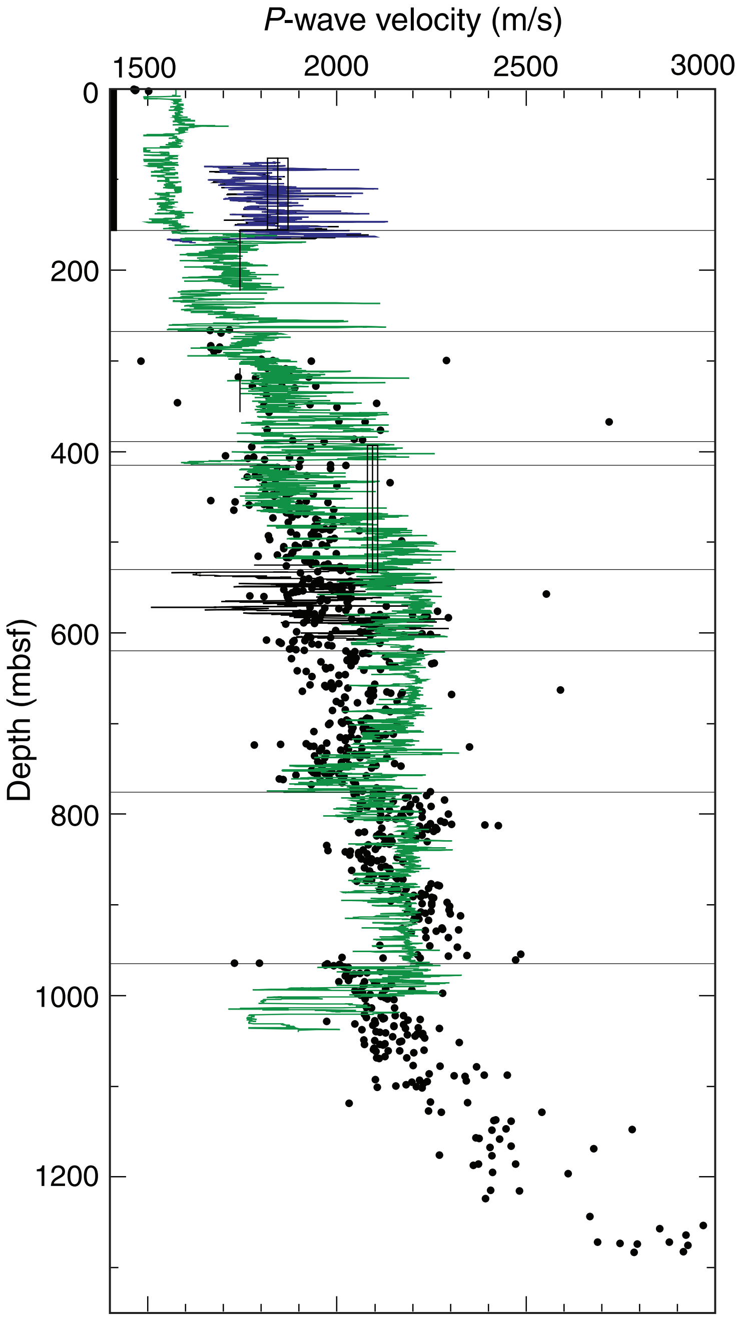

Figure F30. Summary of synthetic seismogram analyses, Site 808. **A.** Two-way traveltime (TWT) vs. depth relationship. **B.** Density and velocity curves where velocity is shown as slowness (inverse of velocity). **C.** Modeled source wavelet. **D.** Reflection coefficient. **E.** Common depth points (CMPs) 789–809 from Inline 284 with the synthetic seismogram displayed in the center as three identical traces. CMP spacing = 25 m, ampl. = amplitude.

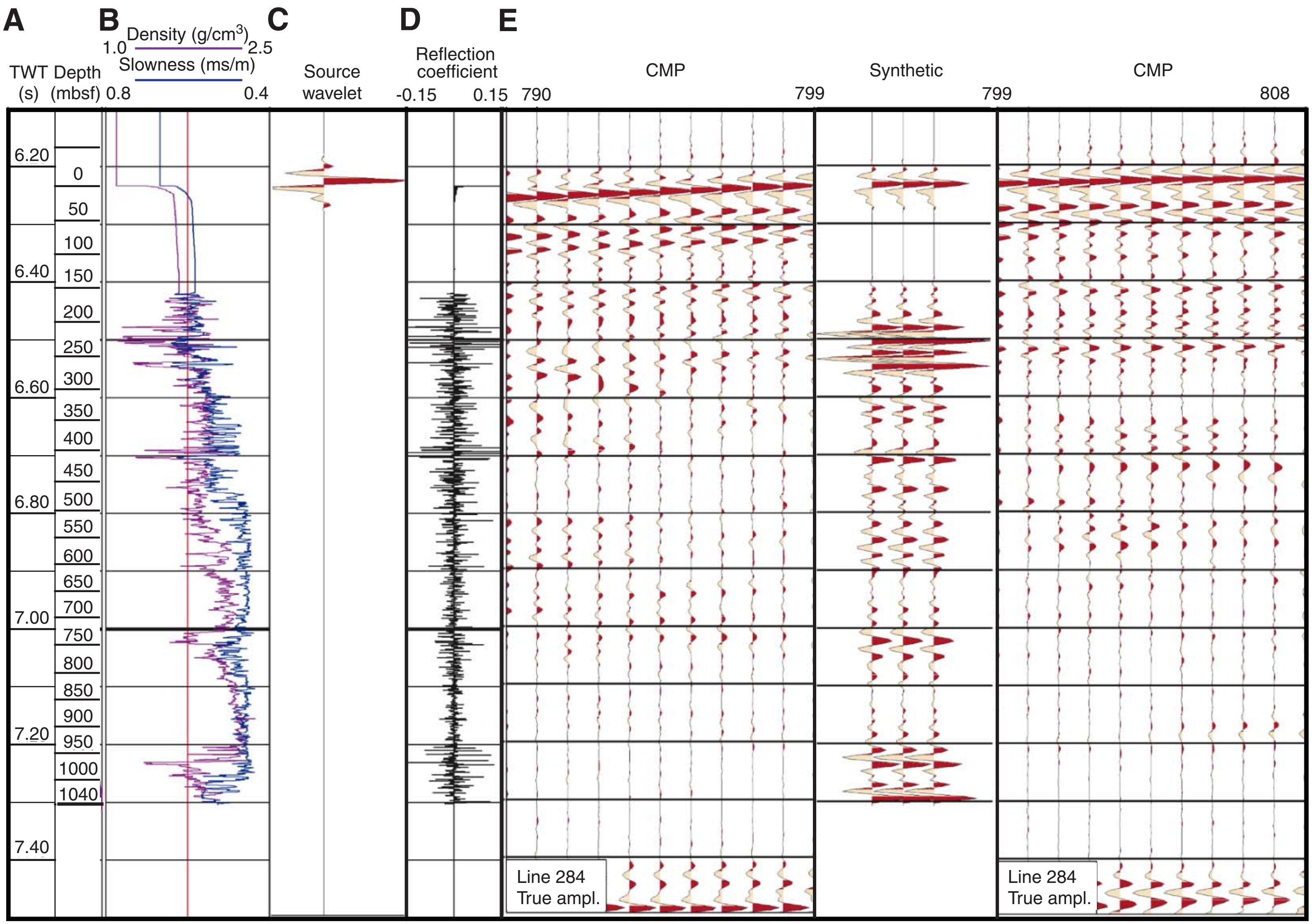

Figure F31. Video of the extraction of the drill string and ensuing fall of the 42 m of Advanced CORK (ACORK) and casing left above the seafloor in Hole 808I. (QuickTime software is available for the Macintosh and Windows platforms only. Please see **"QuickTime Movies"** in 196IR.PDF for further information. Click the image to play the movie.)

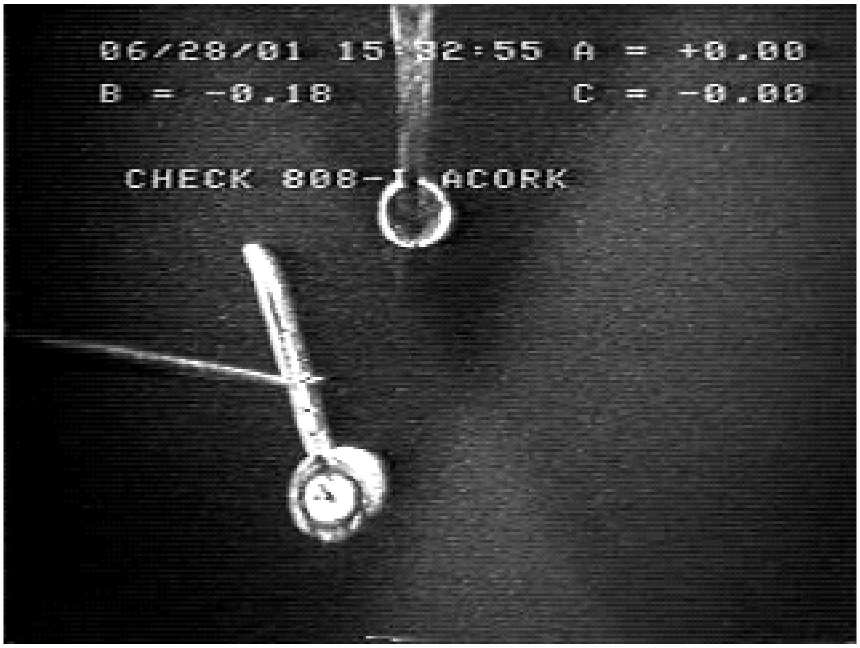

Figure F32. Video inspection of the Advanced CORK (ACORK) components left on the seafloor near Hole 808I. **A.** Reentry cone with bent ACORK casing extending to the north. **B.** Middle section of the exposed ACORK casing. The critical hydraulic umbilical is visible as a dark line on the east side of the casing (lower side in this view). **C.** The ACORK head with the data logger and underwater-mateable remotely operated vehicle connector facing up. (QuickTime software is available for the Macintosh and Windows platforms only. Please see **"QuickTime Movies"** in 196IR.PDF for further information. Click the image to play the movie.)

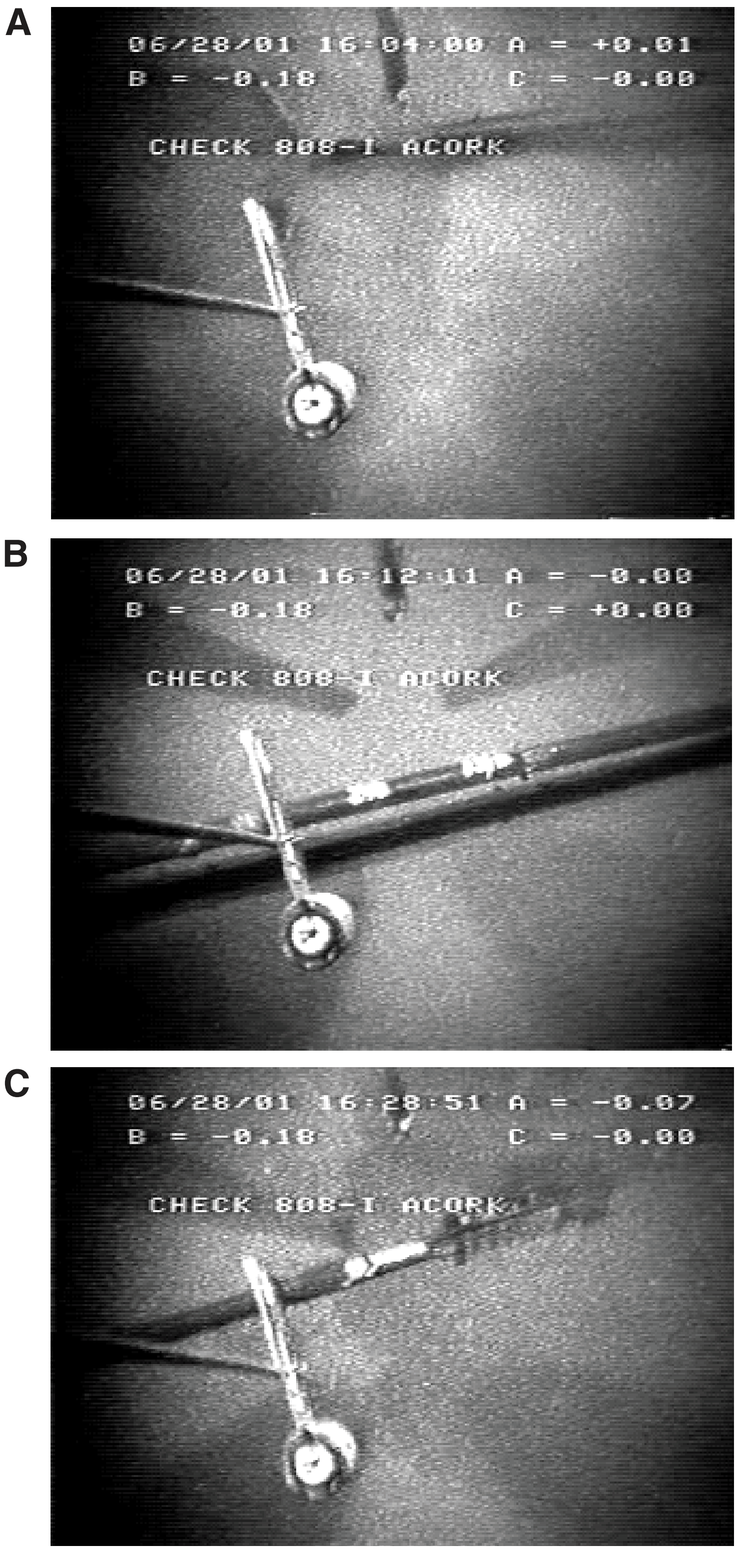

Table T1. Operations, summary, Site 808.

Hole 808H
Latitude: 32°21.2142′N
Longitude: 134°56.7009′E
Seafloor (drill pipe measurement from rig floor, mbrf): 4686.0
Distance between rig floor and sea level (m): 10.9
Water depth (drill pipe measurement from sea level, m): 4675.1

Hole 808I
Latitude: 32°21.2145′N
Longitude: 134°56.7003′E
Seafloor (drill pipe measurement from rig floor, mbrf): 4686.0
Distance between rig floor and sea level (m): 10.9
Water depth (drill pipe measurement from sea level, m): 4675.1

	Start		End		Depth (mbsf)			Time on hole		
Operation	Date (2001)	Time (local)	Date (2001)	Time (local)	Top	Bottom	Drilled (mbsf)	Hours	Days	Comments
196-808H:										
Install reentry cone and 20-in casing	18 May	1937	20 May	1910	0	126.7	126.7	47.5	1.98	Mud motor failed; pulled out of hole; hole abandoned
					Totals for Hole 808H:		126.7	47.5	1.98	
196-808I:										
Install reentry cone and 20-in casing	20 May	1910	22 May	1130	0	160.1	160.1	40.3	1.68	20-in casing shoe at 156.6 mbsf
LWD	22 May	1130	27 May	1710	160.1	1057.6	897.4	125.7	5.24	Unable to penetrate past 1057.6 mbsf
Open 9⅞-in LWD hole to 17½ in for ACORK	14 Jun	0130	18 Jun	1555	160.1	975.3	815.2	110.4	4.60	
Assemble and drill in ACORK	18 Jun	1555	28 Jun	1945	—	—	—	243.8	10.16	964-m-long ACORK could only be drilled in to 927 mbsf; time on hole includes 17-hr DP transit back to site
					Totals for Hole 808I:		1872.7	520.2	21.68	
					Totals for Site 808:		1999.4	567.7	23.66	
					Totals for Leg 196:		3541.9	1152.9	48.05	

Notes: LWD = logging while drilling, ACORK = Advanced CORK. DP = dynamic positioning. — = not applicable.

Table T2. Mean values and standard deviations of log properties for each log unit, Hole 808I.

Log unit/subunit	Gamma ray (API)		Resistivity (Ωm)		Density (g/cm³)		Photoelectric effect (b/e⁻)		Neutron porosity (pu)		Differential caliper (in)	
	Mean	SD	Mean	SD	Mean	SD	Mean	SD	Mean	SD	Mean	SD
1	46.5	11.7	0.84	0.14	1.68	0.22	2.93	0.31	0.61	0.08	0.85	0.40
2a	61.5	4.4	0.81	0.09	1.88	0.09	3.01	0.17	0.56	0.04	1.03	0.20
2b	57.6	14.6	0.91	0.12	1.87	0.25	3.00	0.28	0.55	0.06	1.00	0.53
2c	62.1	4.1	0.63	0.05	1.84	0.07	2.98	0.15	0.56	0.04	1.22	0.16
3	68.6	6.5	0.67	0.11	1.98	0.10	3.15	0.16	0.52	0.04	0.85	0.29
4a	71.8	5.6	0.62	0.09	2.03	0.13	3.20	0.17	0.52	0.04	0.69	0.29
4b	76.5	6.4	0.65	0.08	2.17	0.08	3.17	0.15	0.48	0.04	0.49	0.15
4c	76.8	4.2	0.58	0.04	1.82	0.16	3.15	0.24	0.53	0.08	0.96	0.36

Note: SD = standard deviation.

Table T3. Important components and their depths in the Advanced CORK (ACORK) deployed in Hole 808I.

Component	Depth (mbsf)	Notes
Top of ACORK	Initially –42, now 0	Top of ACORK fell over onto seafloor. Casing and umbilical appear to be intact and instruments are accessible by ROV or manned submersible.
ACORK head	Initially –37, now 0	
Packer (center)	60	
Screen (center)	371	⅛-in pressure monitoring line
Screen (center)	533	¼-in pressure monitoring line
Screen (center)	787	¼-in pressure monitoring line
Screen (center)	833	¼-in pressure monitoring line
Screen (center)	879	¼-in pressure monitoring line
Packer (center)	912	
Screen (center)	922	¼-in pressure monitoring line
Casing shoe	927	
17½-in rat hole	972	Filled in?

Note: ROV = remotely operated vehicle.